UNIVERSITY OF ROCHESTER
LABORATORY FOR LASER ENERGETICS

Volume 171
April–June 2022
DOE/NA/3856-1752

LLE Review

Quarterly Report

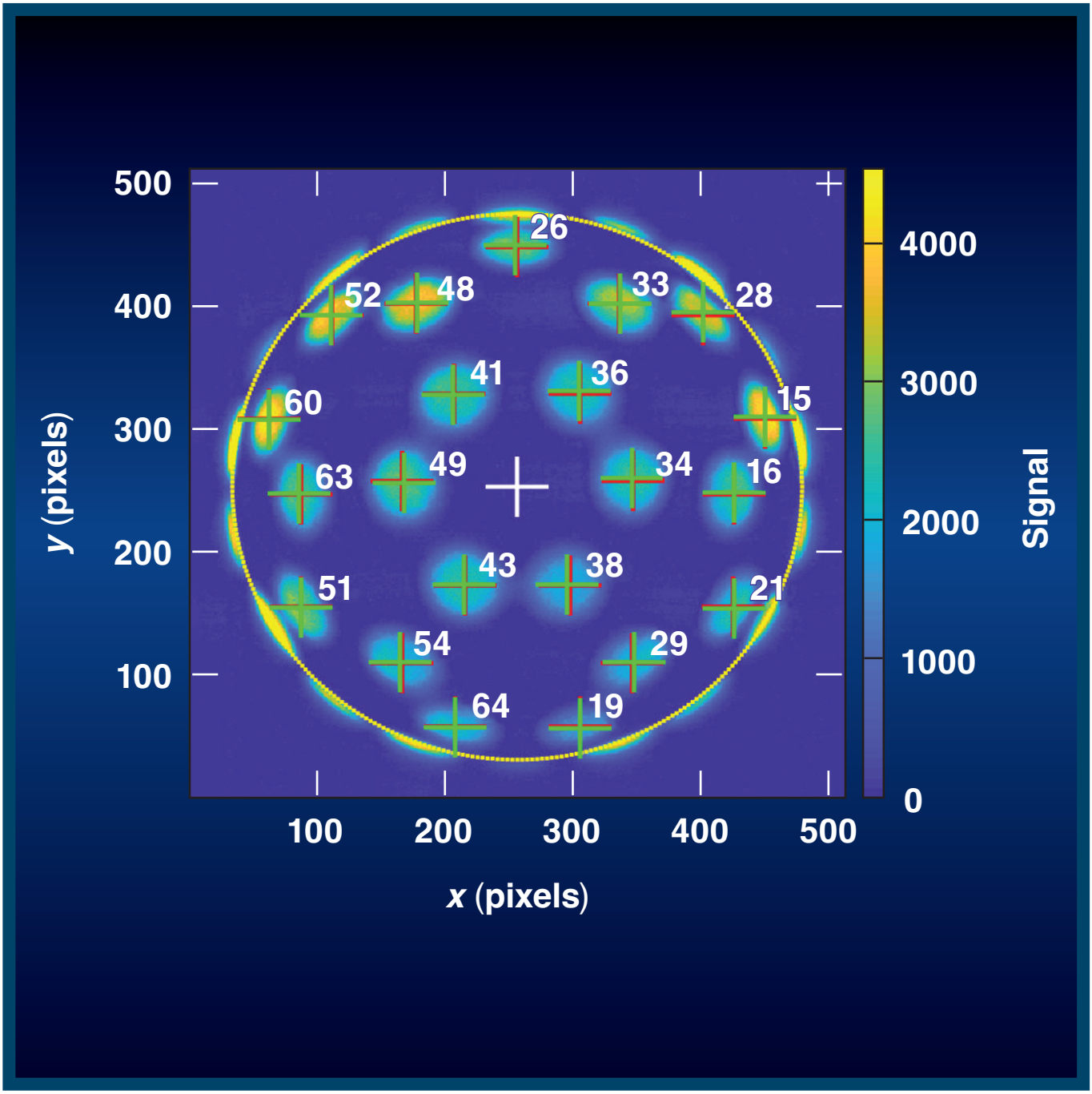

About the Cover:

The cover picture shows an x-ray image recorded on a charge-injection–device electronic sensor by one of the ten x-ray pinhole cameras located in TIM-5 in during a pointing shot. Beam-pointing accuracy is verified on the OMEGA Laser System by irradiating a 4-mm-diam Au-coated spherical target with ~23 kJ of laser energy. The large target diameter is used to separate the individual ~850-μm-diam laser spots that are typically overlapped on the ~1-mm-diam implosion targets. The spatial intensity distribution of the individual laser beams is carefully shaped and smoothed using distributed phase plates (DPP's), polarization wedges, and smoothing by spectral dispersion. A well-defined edge of the target can also be observed from the shadow of the beams behind the horizon of the sphere (yellow circle), which can be used to evaluate the location of the center of the sphere (white cross). The position of up to 21 beams can be evaluated from this image (red crosses) and compared to the desired locations (green crosses).

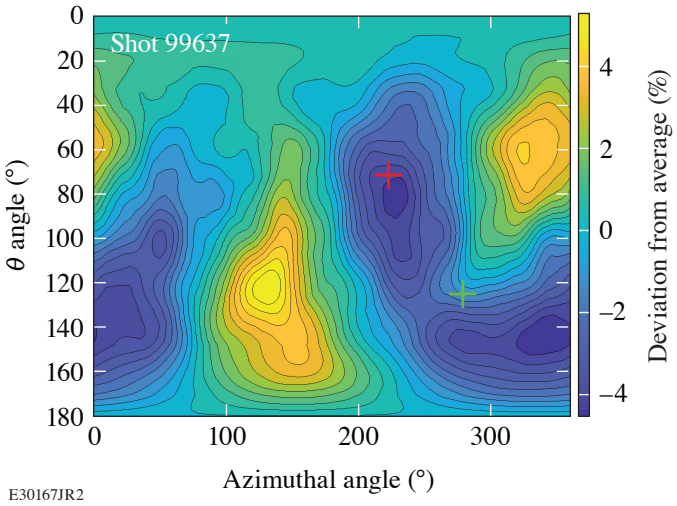

E30167JR2

To assess the impact of the pointing errors on the illumination uniformity, the on-target intensity distribution is calculated by overlapping all 60 beams onto a sphere of the typical diameter of an implosion target of ~870 μm. The pointing of the beams is set according to the evaluation of the data from the pointing shots. Identical beam profiles are assumed for all 60 beams, with a super-Gaussian intensity profile as set by the DPP. The resulting intensity map is shown in the figure on the right. Additionally, a modal decomposition into ℓ modes is performed, with the inferred direction of the $\ell = 1$ mode (red cross) and $\ell = 2$ mode (green cross) indicated in the above image.

The work described in this volume includes current research at the Laboratory for Laser Energetics, which is supported by New York State Energy Research and Development Authority, the University of Rochester, the U.S. Department of Energy Office of Inertial Confinement Fusion under Cooperative Agreement No. DE-NA0003856, and other agencies.

Printed in the United States of America
Available from
National Technical Information Services
U.S. Department of Commerce
5285 Port Royal Road
Springfield, VA 22161
www.ntis.gov

For questions or comments, contact Milton J. Shoup III, Editor, Laboratory for Laser Energetics, 250 East River Road, Rochester, NY 14623-1299, (585) 275-9636.

www.lle.rochester.edu

UNIVERSITY OF ROCHESTER
LABORATORY FOR LASER ENERGETICS

Volume 171
April–June 2022
DOE/NA/3856-1752

LLE Review

Quarterly Report

Contents

In Brief

This volume of LLE Review 171 covers the period from April–June 2022. Articles appearing in this volume are the principal summarized results for long-form research articles. Readers seeking a more-detailed account of research activities are invited to seek out the primary materials appearing in print, detailed in the publications and presentations section at the end of this volume.

Highlights of research presented in this volume include:

- C. Stoeckl *et al.* present beam-pointing verification using x-ray pinhole cameras on the 60-beam OMEGA Laser (p. 1).
- C. J. Forrest *et al.* describe measurements of low-mode asymmetries in the areal density of laser-direct-drive DT cryogenic implosions on OMEGA using neutron spectroscopy (p. 3).
- F. García-Rubio *et al.* discuss the theory of the magnetothermal instability in coronal plasma flows (p. 6).
- N. Acharya, H. Aluie, and J. K. Shang discuss a numerical investigation of a laser-driven shock interaction with a deformable particle (p. 9).
- S. X. Hu *et al.* describe probing extreme atomic physics at Gbar pressures (p. 11).
- H. Yin *et al.* report on the effective drift velocity from turbulent transport by vorticity (p. 13).
- L. Ceurvorst *et al.* report on the development of an x-ray radiography platform to study laser-direct-drive energy coupling at the National Ignition Facility (p. 15).
- D. H. Edgell *et al.* present on the use of a scattered-light uniformity imager for diagnosing laser-absorption asymmetries on OMEGA (p. 18).
- K. Churnetski *et al.* present three-dimensional hot-spot x-ray emission tomography results from cryogenic deuterium–tritium direct-drive implosions on OMEGA (p. 20).
- V. Yu. Glebov *et al.* demonstrate a new neutron time-of-flight detector for deuterium–deuterium yield and ion-temperature measurements on OMEGA (p. 24).
- H. G. Rinderknecht *et al.* report on a knock-on deuteron imager used for measurements of fuel and hot-spot asymmetry in direct-drive inertial confinement fusion implosions (p. 26).
- D. Weiner *et al.* discuss the design and implementation of a digital optical microscope for measuring submicron defects on cryogenic DT targets (p. 29).
- S. F. Nwabunwanne and W. R. Donaldson discuss the performance of a new class of tunable picosecond AlGaN UV photodiodes (p. 32).
- J. Katz *et al.* report on the measurement of laser absorption in underdense plasmas using near-field imaging of the incident and transmitted beams (p. 35).
- S. T. Ivancic *et al.* discuss the design of the high-yield time-gated x-ray hot-spot imager for OMEGA (p. 38).
- C. Dorrer *et al.* demonstrate high-resolution mapping of phase-matching conditions in second-order nonlinear crystals (p. 40).

- S. Bucht *et al.* report on achieving 100-GW idler pulses from an existing petawatt optical parametric chirped-pulse amplifier (p. 43).
- J. Zhang, W. R. Donaldson, and G. P. Agrawal discuss the impact of Raman scattering on the temporal reflection from a short soliton (p. 46).
- S. Zhang *et al.* report on a the first-principles equation of state of CHON resin for inertial confinement fusion applications (p. 49).
- B. J. Henderson *et al.* present measurements of the shocked-silica aerogel radiance transition (p. 52).
- R. M. N. Goshadze *et al.* present an analysis of shock-induced metallization of polystyrene along the principal Hugoniot investigated by advanced thermal density functionals (p. 54).
- J. A Frenje *et al.* report on the 13th Omega Laser Facility Users Group Workshop, held in person and virtually from 27–29 April 2022 (p. 57).
- J. Puth *et al.* summarize operations of the Omega Laser Facility during the third quarter of FY22 (p. 66).

Milton Shoup III
Editor

Beam-Pointing Verification Using X-Ray Pinhole Cameras on the 60-Beam OMEGA Laser

C. Stoeckl, D. Cao, L. Ceurvorst, A. Kalb, J. Kwiatkowski, A. Shvydky, and W. Theobald

Laboratory for Laser Energetics, University of Rochester

On the OMEGA Laser System, the beam-pointing accuracy is verified by irradiating a 4-mm-diam Au-coated spherical target with ~23 kJ of laser energy.[1] Up to ten x-ray pinhole cameras record the emission from all 60 beam spots [see Fig. 1(a)]. A new set of algorithms has been developed to improve the accuracy of the pointing evaluation. An updated edge-finding procedure allows one to infer the center of the sphere with subpixel accuracy. A new approach was introduced to back-propagate the pixel locations on the 2-D image to the 3-D surface of the sphere. A fast Fourier transform-based noise reduction method significantly improves the signal-to-noise ratio of the data. Based on the beam-pointing analysis, hard-sphere calculations of the laser-drive illumination uniformity on the target surface and the decomposition of the illumination distribution into lower order modes (1 to 10) are evaluated.

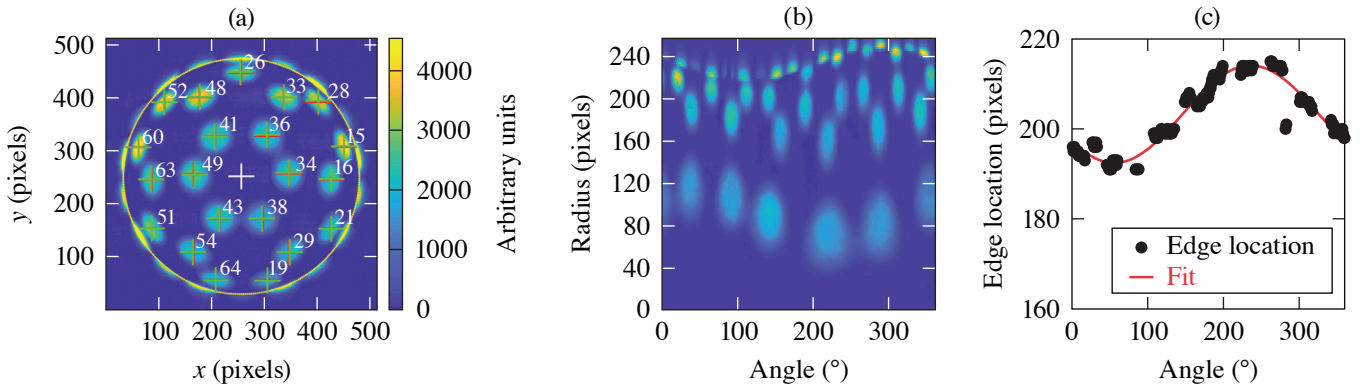

Figure 1
(a) X-ray image from one of the ten x-ray pinhole cameras acquired during a pointing shot. The position of up to 21 beams can be evaluated (red crosses) and compared to the desired locations (green crosses). The white cross shows the evaluated center of the sphere and the yellow circle is the outside radius. (b) Angular lineouts from a first guess of the center of the image of the sphere. (c) Evaluated location of the edge of the sphere compared to a cosine fit.

To infer the location of the center of the sphere, radial lineouts starting from a first estimate of the center (x_e, y_e) of the image are taken in 1° angular increments. Figure 1(b) shows a composite of these lineouts in the form of a 2-D image. The edge feature from the self-shadowing of the beams behind the horizon can be clearly seen at the top of the image. The location of the edge is determined as the position of the maximum of the gradient of each lineout and plotted in Fig. 2(c). Lines with low signal or high noise are discarded. A cosine function of the form $r = r_0 + a * \cos(t + b)$ is fitted to the data, with t as the angle, b as the phase offset, and a as the amplitude of the radial variation. From simple geometry, two offsets (dx, dy) can be computed that correct the estimated center to provide a better fit of the center $x_f = x_e + dx$; $y_f = y_e + dy$. Depending on the magnitude of the radial variation, this process can be repeated to get the best fit of the center.

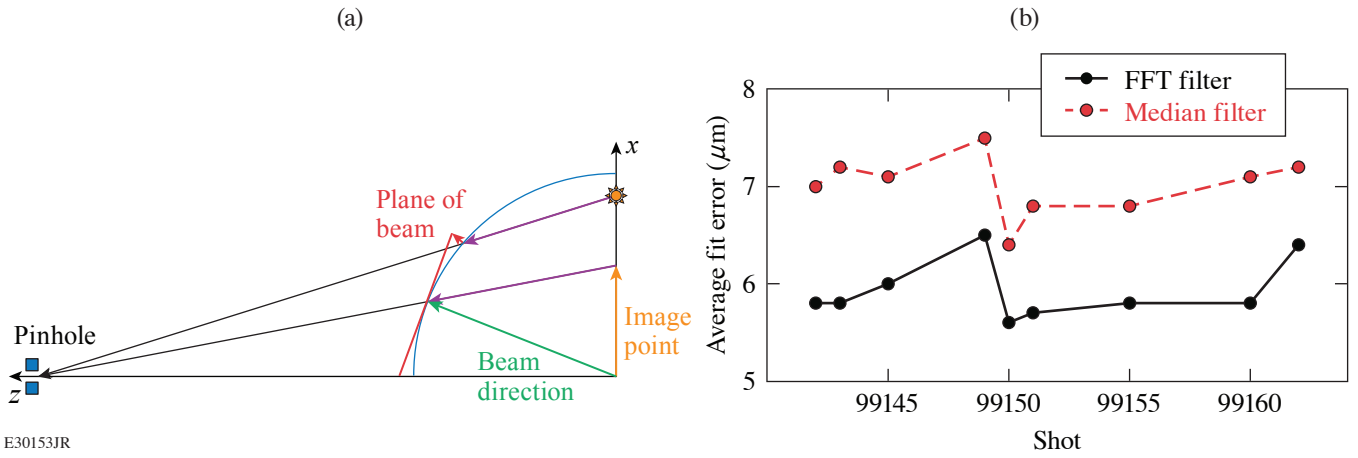

Figure 2
(a) Sketch of the geometry used to project the emission recorded from the individual beams into the planes perpendicular to the beam propagation direction. (b) Average pointing error evaluated from a median filtered image compared to a fast Fourier transform (FFT)-filtered image.

The x-ray pinhole camera image is a 2-D projection of the emission from a 3-D sphere. To infer the intensity distribution on the sphere, the image from the sensor is mapped to the object plane through the pinhole, and then each pixel location is projected onto the sphere [see purple arrow in Fig. 2(a)]. Since the intensity distribution of the laser focus is defined in a plane perpendicular to the laser propagation direction, the pixel locations on the sphere for a single beam are further projected onto the plane perpendicular to the laser direction tangent to the surface of the sphere [red arrow in Fig. 2(a)]. This procedure corrects all geometric effects of the imaging and compensates the ellipticity of the beams close to the edge of the image very well.

Simple median filters are typically used to clean up the raw charge-injection–device (CID) images under the assumption that the noise seen is purely statistical and uncorrelated. Upon more-detailed inspection of the images, it became obvious that there are medium- and large-scale correlations in the noise mostly caused by imperfections in the readout system. To clean up these correlated features a 2-D FFT is generated from the image and the regions in the FFT corresponding to high spatial frequencies or clearly identifiable background features are set to zero. A cleaned-up image is then reconstructed using the inverse FFT. The evaluation of the pointing with the FFT filtered images show a significant improvement in fit error [see Fig. 2(b)].

The limiting factors on the accuracy of the pointing evaluation, which are currently of the order of 5 μm, are most likely the quality of the pointing targets, noise (especially correlated features) in the CID readout, and imperfections in the intensity distribution of the laser beam focus. A more-uniform coating for of targets would reduce the artifacts in the image, like the “holes” [as seen in Fig. 1(a)], and lead to better fits. It is also likely that the FFT filter can be further improved by using an evolutionary algorithm or a machine learning approach.

This material is based upon work supported by the Department of Energy National Nuclear Security Administration under Award Number DE-NA0003856, the University of Rochester, and the New York State Energy Research and Development Authority.

1. R. A. Forties and F. J. Marshall, Rev. Sci. Instrum. **76**, 073505 (2005).

Measurements of Low-Mode Asymmetries in the Areal Density of Laser-Direct-Drive Deuterium–Tritium Cryogenic Implosions on OMEGA Using Neutron Spectroscopy

C. J. Forrest,[1] A. Crilly,[2] A. Schwemmlein,[1] M. Gatu Johnson,[3] O. M. Mannion,[4] B. Appelbe,[2] R. Betti,[1] V. Yu. Glebov,[1] V. Gopalaswamy,[1] J. P. Knauer,[1] Z. L. Mohamed,[1] P. B. Radha,[1] S. P. Regan,[1] C. Stoeckl,[1] and W. Theobald[1]

[1]Laboratory for Laser Energetics, University of Rochester
[2]Centre for Inertial Fusion Studies, the Blackett Laboratory, Imperial College London
[3]Plasma Science and Fusion Center, Massachusetts Institute of Technology
[4]Sandia National Laboratories

The OMEGA laser is used to study direct-drive inertial confinement fusion (ICF) by symmetrically irradiating a thin shell target with nominally identical laser beams. The shell is comprised of an outer plastic ablator (<10 μm) and a layer of cryogenic deuterium–tritium (DT) ice (~50 μm) encapsulating a vapor region DT gas. In these target designs, the incident laser ablates the thin shell, which then launches one or multiple shocks through the remaining converging shell and into the vapor region. The shock-transit stage of the implosion is followed by a deceleration phase, where the kinetic energy of the converging shell is converted to the internal energy of the hot spot. To achieve conditions relevant for ignition implosion designs, the hot-spot size must exceed the mean free path of the fusing ions and alpha particles in order to remain confined in the dense plasma. This requirement is essential to maximize the energy deposition of the alpha particle in the hot spot and surrounding dense fuel. Targets that are not compressed symmetrically will be unable to fully convert their shell kinetic energy to hot-spot thermal energy.

Areal density is one of the key parameters that determines the confinement time in ICF experiments, and low-mode asymmetries in the compressed fuel are detrimental to the implosion performance. The energy spectra from scattering of the primary DT neutrons off the compressed cold fuel assembly are used to investigate low-mode nonuniformities in direct-drive cryogenic DT implosions. For spherically symmetric implosions, the shape of the energy spectrum is primarily determined by the elastic and inelastic scattering cross sections for both neutron–deuterium (nD) and neutron–tritium (nT) kinematic interactions given by

$$\frac{\mathrm{d}N}{\mathrm{d}E} = Y_\mathrm{n}\left\{\left[\mathrm{DT} + \frac{1}{2}\frac{f_\mathrm{d}}{f_\mathrm{t}}\frac{\langle\sigma\nu_\mathrm{dd}\rangle}{\langle\sigma\nu_\mathrm{dt}\rangle}\mathrm{DD} + \frac{f_\mathrm{t}}{f_\mathrm{d}}\frac{\langle\sigma\nu_\mathrm{tt}\rangle}{\langle\sigma\nu_\mathrm{dt}\rangle}\mathrm{TT}\right]\right.$$
$$\left. + \rho L N_\mathrm{a}\left[\frac{\left(\mathrm{d}\sigma_\mathrm{nD}/\mathrm{d}E\right)f_\mathrm{d} + \left(\mathrm{d}\sigma_\mathrm{nT}/\mathrm{d}E\right)f_\mathrm{t}}{f_\mathrm{d}m_\mathrm{d} + f_\mathrm{t}m_\mathrm{t}} + \frac{\left(\mathrm{d}\sigma^\mathrm{d}_{\sigma_\mathrm{n2n}}/\mathrm{d}E\right)f_\mathrm{d}}{f_\mathrm{d}m_\mathrm{d} + f_\mathrm{t}m_\mathrm{t}} + \frac{\left(\mathrm{d}\sigma^\mathrm{t}_{\sigma_\mathrm{n2n}}/\mathrm{d}E\right)f_\mathrm{t}}{f_\mathrm{d}m_\mathrm{d} + f_\mathrm{t}m_\mathrm{t}}\right]\right\},$$

where Y_n is the primary DT yield, f_d and f_t are the fuel fraction of the fuel, and $\langle\sigma\nu\rangle$ is the reactivity rate with the associated fusing pair of ions. In the above expression DT, DD, and TT represent the shape of the primary neutron energy spectra for each reaction. The differential and double-differential cross-sections require a term to better describe this variation in the cold fuel, assuming a low-mode ($\ell = 1$) distribution as given by

$$\frac{\mathrm{d}\sigma}{\mathrm{d}E} = \int \left(\frac{\mathrm{d}\sigma}{\mathrm{d}\Omega}\right)\left(1 + \frac{\Delta\rho L}{\rho L} * \cos\theta\right)\mathrm{d}E,$$

$$\frac{\mathrm{d}\sigma_{\mathrm{n,2n}}}{\mathrm{d}E} = \int 2\pi\left(\frac{\mathrm{d}^2\sigma}{\mathrm{d}E\mathrm{d}\Omega}\right)\left(1 + \frac{\Delta\rho L}{\rho L} * \cos\theta\right)\mathrm{d}\cos\theta.$$

Experimental observations shown in Fig. 1 of the low-mode variations cold fuel assembly ($\rho L_0 + \rho L_1$) show good agreement with this recently developed model, indicating a departure from a spherical symmetry of the compressed DT fuel assembly.

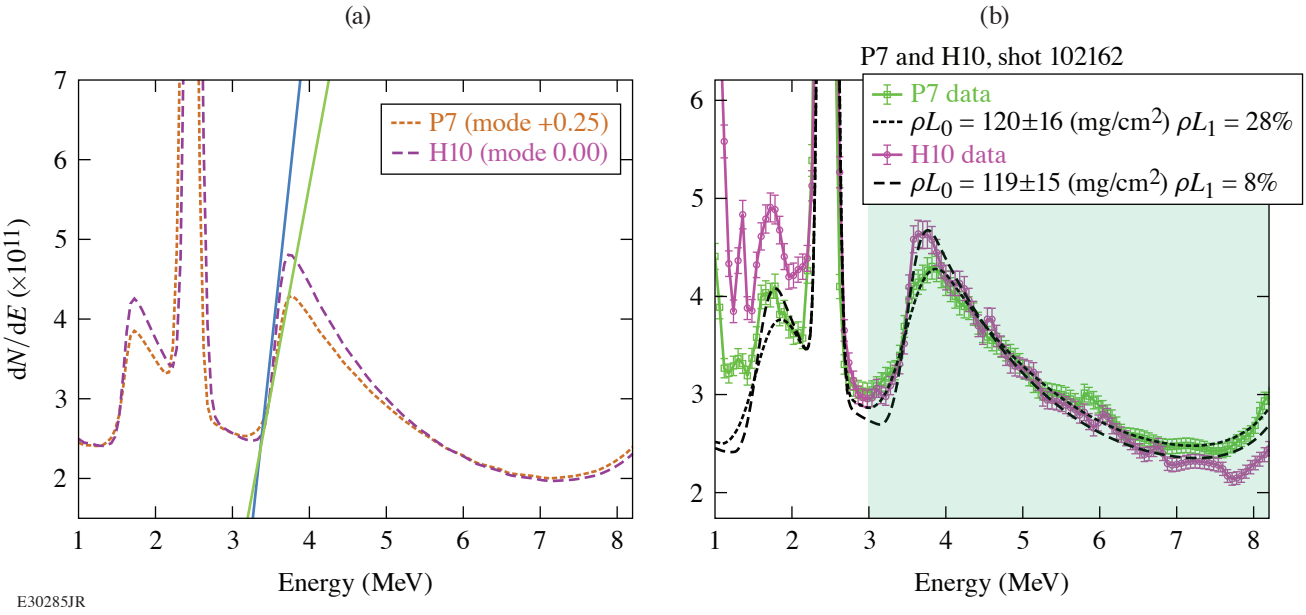

Figure 1
(a) An example of a cryogenic implosion with a significant mode 1 that shows qualitative agreement with the broadening of the kinematic edge due to the anisotropy of the cold fuel depending on the spectrometer's line of sight as predicted by the model. (b) A model illustrates the broadening of the kinematic edge due to the anisotropy of the cold fuel depending on the spectrometer's line of sight. Straight lines tangent to the nT edges are included to emphasize the difference in slopes. An example of a cryogenic implosion with a significant mode 1 shows qualitative agreement with the broadening of the kinematic edge due to the anisotropy of the cold fuel depending on the spectrometers line of sight as predicted by the model.

Another key signature in the presence of a low-mode variation is the broadening of the kinematic end point due to anisotropy of the dense fuel conditions has been observed. Recent theoretical[1] and experimental[2] studies have showed that the neutron-backscatter edge presents a novel measurement of the hydrodynamic conditions at stagnation. The spectral shape of the edge is determined by the velocity distribution of the scattering ions. When there is a large mode-1 variation in areal density, hydrodynamic models predict that the higher areal density side will decelerate slower than the lower areal density side.[3] The lower areal density side will therefore exhibit a larger variation in scattering ion velocities and consequently will produce a broader backscatter edge; the opposite is true for the higher areal density side.

More-recent hydrodynamics simulations of OMEGA implosions perturbed by a mode 1 were post-processed with a neutron transport code to obtain synthetic spectra on the P7 and H10 OMEGA lines of sight showing the anisotropic edge broadening. This anisotropy has been predicted in simulation to appear (Fig. 1) in the backscatter edge shape along different lines of sight. Measurements on the broadening of the kinematic edges show qualitative agreement with the anisotropy of the dense fuel conditions from separate lines of sight given by the model prediction. The anisotropy is also correlated with the observed mode-1

areal-density asymmetry. The P7 line of sight observes a positive mode-1 areal-density asymmetry and therefore backscatter occurs in a lower areal-density region for this line of sight.

This material is based upon work supported by the Department of Energy National Nuclear Security Administration under Award Number DE-NA0003856, the University of Rochester, and the New York State Energy Research and Development Authority.

1. A. J. Crilly *et al.*, Phys. Plasmas **27**, 012701 (2020).
2. O. M. Mannion *et al.*, Phys. Rev. E **105**, 055205 (2022).
3. B. K. Spears *et al.*, Phys. Plasmas **21**, 042702 (2014).

The Theory of Magnetothermal Instability in Coronal Plasma Flows

F. García-Rubio,[1,2] R. Betti,[1,2,3] J. Sanz,[4] and H. Aluie[1,2]

[1]Laboratory for Laser Energetics, University of Rochester
[2]Department of Mechanical Engineering, University of Rochester
[3]Department of Physics and Astronomy, University of Rochester
[4]Escuela Técnica Superior de Ingeniería Aeronáutica y del Espacio, Universidad Politécnica de Madrid, Spain

In this summary, the theory of the magnetothermal instability (MTI) is revisited through the lens of the stability of uniform systems, and its implication in the corona dynamics of direct-drive implosions is discussed. The underlying mechanism of this instability corresponds exclusively to the interplay between the Biermann battery generating magnetic (B) fields and the Righi–Leduc term bending the heat flux lines, as shown in Fig. 1. In its most simple configuration, a temperature perturbation δT results in B-field generation $\delta\vec{B}$ via the Biermann battery. This allows the Righi–Leduc heat flux, $\vec{q}_{\mathrm{RL}} \propto \left(T_0^4/n_0\right)\nabla T_0 \times \delta\vec{B}$, to pump heat into the hotter regions of the fluid, thereby driving the MTI by amplifying the δT perturbation.

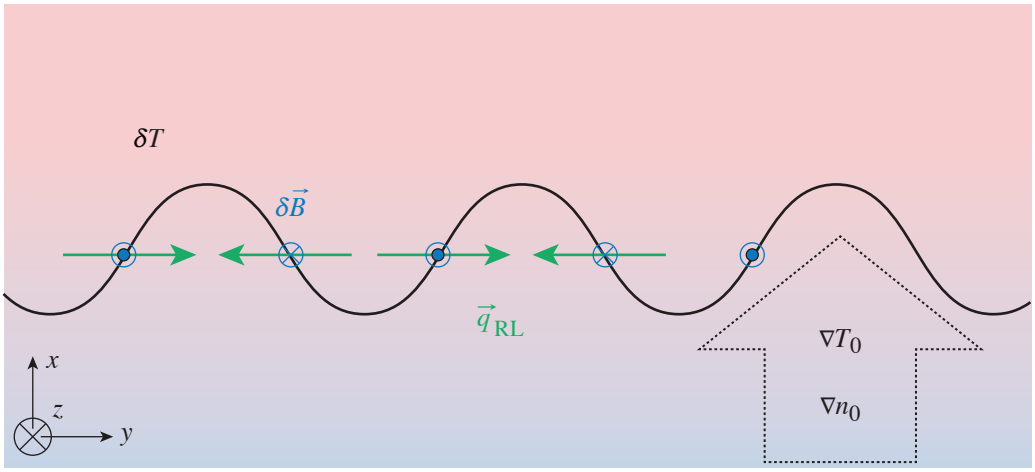

Figure 1
Schematic of the magnetothermal instability as first explained in Ref. 1. It relied on the background ∇T_0 and ∇n_0 being aligned.

The main novelty in the linear stability analysis performed in this summary corresponds to the distinction between the convective and the absolute nature of the perturbation growth. Previous analyses[1–3] identified the MTI as a convective instability and observed significant suppression of its growth rate caused by Nernst convection.[3] In the present linear analysis, we have applied the instability criteria derived by Briggs[4] to prove that, in the region where the Nernst and plasma blowoff velocities cancel, the MTI can be absolute and wave-packet perturbations grow *in situ*. The growth rate thereby derived becomes

$$\gamma \mathrm{MTI}_{\mathrm{ns}^{-1}} = 0.19 i\overline{\omega}_{M_2} \frac{10}{\log \Lambda} \frac{\gamma_0''}{\gamma_0 \delta_0 Z} \frac{T_{\mathrm{keV}}^{5/2}}{n_{10^{22}\mathrm{cm}^{-3}}} \left(\frac{\mathrm{d} \log T}{\mathrm{d}x_{100\,\mu\mathrm{m}}} \right)^2,$$

where γ_0'', γ_0, and δ_0 are coefficients that depend on the atomic number Z given in Braginskii,[5] and the dimensionless frequency $i\overline{\omega}_{M_2}$ depends on the isothermal Mach number (Ma) of the section in the corona in consideration and the pressure-to-temperature gradient ration (δ), Fig. 2.

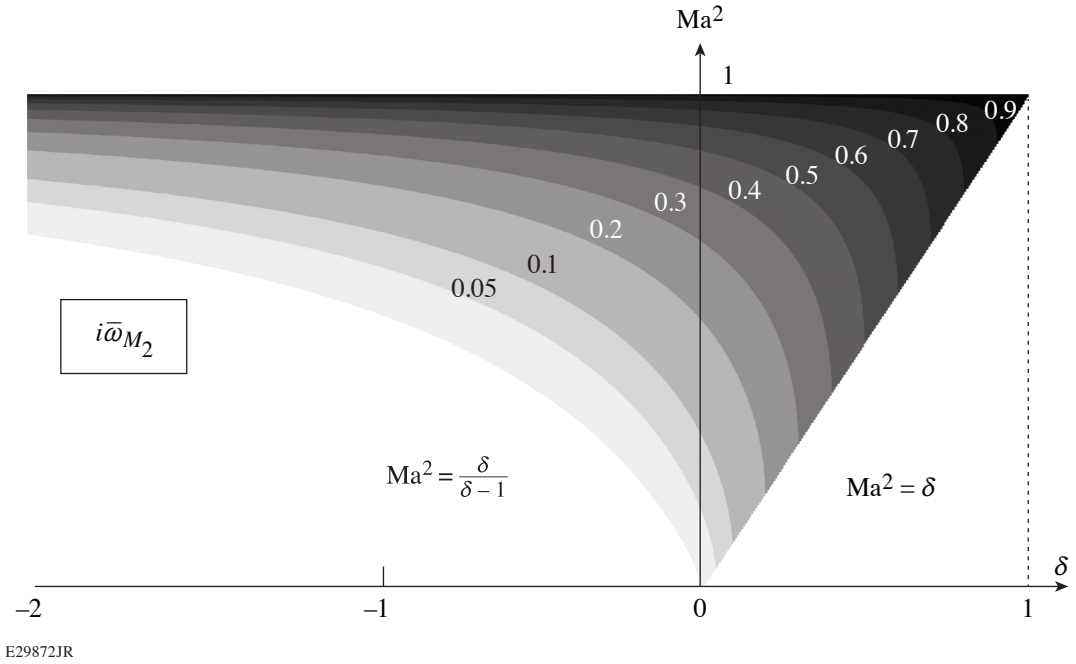

Figure 2
Isocontours of the temporal growth rate $i\overline{\omega}_{M_2}$ in the phase space isothermal Mach number Ma and pressure-to-temperature gradient ratio δ.

The analysis has been extended to derive the dispersion relation for short-wavelength perturbations developing in nonuniform profiles with application to coronal plasmas. It is found that the condition for MTI requires the net B-field convection velocity to be small at the isothermal sonic section, and the plasma conditions in this section govern the dynamics of the instability. This theory reveals a picture of the MTI where the conduction layer is the dynamically active region of the corona. Here is found the spatial resonance that causes perturbations to grow *in situ*, hence traveling with the imploding shell and potentially altering its dynamics. The structure of the unstable perturbations tends to elongate filaments in the azimuthal direction, in agreement with the observations made in Ref. 6. They can spread out to regions of outflowing convection velocity, being subsequently stretched radially and filling the outer corona. This picture is in qualitative agreement with the proton radiographs of imploding fast-ignition capsules performed by Rygg *et al.*,[7] who observed striated fields that originate close to the capsule surface, and conjectured that the vast spatial extent of these fields reflects an outward convection of filamentary structures originally produced inside the critical surface.

Applying this theory to direct-drive inertial confinement fusion implosions provides an MTI growth rate in the range of a fraction to few gigahertz (see Fig. 3), which is milder than the ones discussed by Manuel *et al.*[8] and Bissell *et al.*[9] (several to tens of gigahertz). This is mainly due to authors employing growth rate expressions derived from a convective instability analysis, which favors lower-density, higher-temperature regions (outer corona) as more-unstable regions. The outer corona indeed supports unstable waves, but we deem we must impose the requirement for absolute instability to account how the MTI affects the dynamics of the implosion. This holds the plasma state at the conduction layer responsible for the growth rate of the MTI. Finally, analysis of hydro-equivalent implosions suggests that unstable perturbations undergo more *e* foldings of growth in larger-size targets.

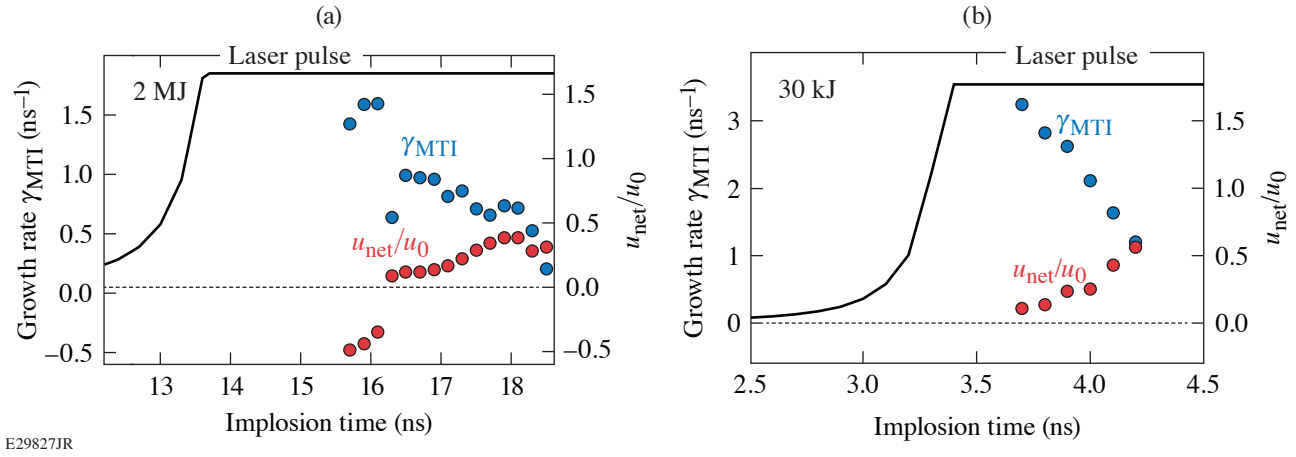

Figure 3
Maximum growth rate γ and velocity ratio u_{net}/u_0 at the isothermal sonic point for(a) 2-MJ and (b) 30-kJ direct-drive implosions. The laser power pulse shape is plotted for reference.

This work is supported by the Department of Energy Office of Science, Fusion Energy Sciences program grants DE-SC0016258, DE-SC0014318 and DE-SC0021072. F. García-Rubio was also supported by the Advanced Research Projects Agency-Energy (ARPA-E), U.S. Department of Energy, under Award No. DE-AR0001272. J. Sanz was also supported by the Spanish Ministerio de Economía y Competitividad, Project No. RTI2018-098801-B-I00. H. Aluie was also supported by U.S. DOE grants DE-SC0020229 and DE-SC0019329, U.S. NASA grant 80NSSC18K0772, U.S. NSF grants OCE-2123496 and PHY-2020249, and U.S. NNSA grants DE-NA0003856 and DE-NA0003914. This material is based upon work supported by the University of Rochester and the New York State Energy Research and Development Authority.

1. D. A. Tidman and R. A. Shanny, Phys. Fluids **17**, 1207 (1974).
2. J. J. Bissell, C. P. Ridgers, and R. J. Kingham, Phys. Rev. Lett. **105**, 175001 (2010).
3. M. Sherlock and J. J. Bissell, Phys. Rev. Lett. **124**, 055001 (2020).
4. R. J. Briggs, *Electron-Stream Interaction with Plasmas* (MIT Press, Cambridge, MA, 1964).
5. S. I. Braginskii, in *Reviews of Plasma Physics*, edited by M. A. Leontovich (Consultants Bureau, New York, 1965), Vol. 1, pp. 205–311.
6. I. V. Igumenshchev *et al.*, Phys. Plasmas **21**, 062707 (2014).
7. J. R. Rygg *et al.*, Science **319**, 1223 (2008).
8. M. J.-E. Manuel *et al.*, Phys. Plasmas **20**, 056301 (2013).
9. J. J. Bissell, R. J. Kingham, and C. P. Ridgers, Phys. Plasmas **19**, 052107 (2012).

Numerical Investigation of Laser-Driven Shock Interaction with a Deformable Particle

N. Acharya,[1,2] H. Aluie,[1,2] and J. K. Shang[1,2]

[1]Department of Mechanical Engineering, University of Rochester
[2]Laboratory for Laser Energetics, University of Rochester

To accurately simulate material behavior at relatively low temperatures, i.e., in the sub-eV range, we require models with strength properties in the solid/liquid regime. Such models are not often included in most radiation-hydrodynamics simulation codes including *FLASH*,[1] which are used as tools to design high-energy-density (HED) experiments. In addition, high-temperature equation-of-state (EOS) models used for simulations become less predictive of the thermodynamic material properties necessary for describing the hydrodynamic processes taking place at low temperatures. For instance, in *FLASH*, only thermal pressure contributes to the computation of the local sound speed. This entirely neglects the existence of nonthermal pressure, which is a property that determines the behavior of shock-compressed solids. Theoretically, this leads to higher material compressibility even at low shock pressures. Veification was carried out in 2-D *FLASH* simulations of an ~50-GPa ablation-driven shock propagating over an Al particle embedded in epoxy (CH) and observed ~3.5× compression and significant deformation of the particle in Fig. 1(a). The predicted evolution of the particle modeled with *IONMIX* EOS did not reproduce the experimental shock Hugoniot.[2] Hence, a technique was developed to implement a modified form of ideal gas EOS to model the materials (including Al, Ti, and W) and study the dynamics of the embedded particle. The simulated shock Hugoniots of multiple materials modeled using this technique compared well with experimental data. Examination of the flow field [see Fig. 1(b)] demonstrated that the unsteady drag coefficient for the particle featured a peak drag due to an unsteady interaction with the transmitted shock and a drag minimum due to shock focusing on the rear end of the particle. However, unlike previous studies performed without laser drives, the particle drag coefficient featured a second minimum due to rarefaction stretching associated with laser shutoff.

Numerous simulations were conducted that investigated the particle response for a range of particle densities, sizes, and acoustic impedances. These results revealed that lighter particles, such as Al, gained significant momentum up to 96% from the shocked CH compared to 29% in the case of heavier W. Finally, the effect of particle acoustic impedance on the bulk particle response was studied. Despite differences observed in the early stage of shock interaction, the acoustic impedance did not influence the peak particle velocity. This identified particle-to-host density ratio as a dominant factor in determining the inviscid terminal velocity of the particle. Time-scale analysis in previous works has pointed out that the shock–particle interaction time scale could be of the same order as the viscous time scale, particularly for condensed-matter systems.[3] Therefore, viscous effects coupled with rarefaction stretching effect could be important for particle drag calculation in the intermediate to later stages of shock interaction.

Finally, the simplified approach of modeling materials for hydrodynamic simulations presented in this work could be useful in studying propagation of shock waves through condensed media, in particular, dispersal of particles in multiphase explosives. The method could also be applied to understand the particle dynamics of tracers for their potential applications to x-ray particle image velocimetry in HED flows.

This work was performed under the auspices of the U.S. Department of Energy under Grant No. DE-SC0019329 within the joint HEDLP program and was supported by the Laboratory Basic Sciences program administered by UR/LLE for DOE/NNSA. H. Aluie was also supported by U.S. DOE Grant Nos. DE-SC0014318 and DE-SC0020229, NSF Grant Nos. PHY-2020249 and OCE-2123496, U.S. NASA Grant No. 80NSSC18K0772, and U.S. NNSA Grant Nos. DE-NA0003856 and DE-NA0003914. J. K.

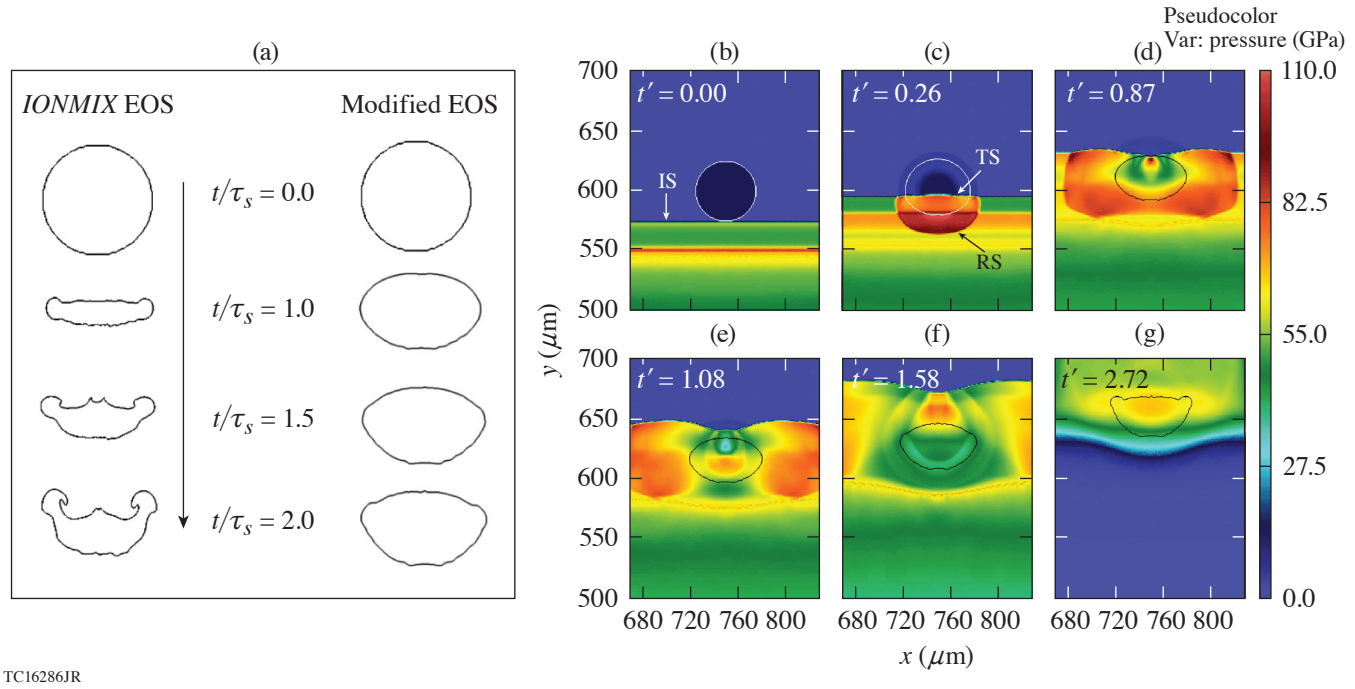

Figure 1
(a) Deformation of an Al particle in CH subjected to a 55-GPa shock with materials modeled using *IONMIX* EOS and a modified ideal gas EOS. τ_s is the shock–particle interaction time based on the particle diameter d_p and shock speed u_s. (b) Contour plots of pressure at increasing times for the post-shock pressure of 55 GPa in CH. Computational domain near the Al particle (modeled using modified EOS) is shown. The white curve [in (b) and (c)] or black curve [in (d)–(g)] is a particle interface constructed using cells around the particle with 25% mass-fraction cutoff. IS, TS, and RS denote incident, transmitted and reflected shock, respectively.

Shang was also supported by NSF Grant No. PHY2020249 and NNSA Grant No. DE-NA0003914. The software used in this work was developed in part by the DOE NNSA- and DOE Office of Science-supported Flash Center for Computational Science at the University of Chicago and the University of Rochester.

1. B. Fryxell *et al.*, Astrophys. J. Suppl. Ser. **131**, 273 (2000).
2. S. P. Marsh, ed. *LASL Shock Hugoniot Data*, Los Alamos Series on Dynamic Material Properties (University of California, Berkeley, CA, 1980).
3. F. Zhang, P. A. Thibault, and R. Link, Proc. Roy. Soc. A **459**, 705 (2003).

Understanding Extreme Atomic Physics at Gbar Pressure

S. X. Hu,[1,2] D. T. Bishel,[1,3] D. A. Chin,[1,3] P. M. Nilson,[1] V. V. Karasiev,[1] I. E. Golovkin,[4] M. Gu,[4] S. B. Hansen,[5] D. I. Mihaylov,[1] N. R. Shaffer,[1] S. Zhang,[1] and T. Walton[4]

[1]Laboratory for Laser Energetics, University of Rochester
[2]Department of Mechanical Engineering, University of Rochester
[3]Department of Physics and Astronomy, University of Rochester
[4]Prism Computational Sciences
[5]Sandia National Laboratories

Spectroscopic measurements of dense plasmas at billions of atmospheres (i.e., Gbar = billions of times the pressure at the Earth's surface) provide tests of the fundamental understanding of how matter behaves at extreme conditions, and by extension, the interpretation of dense astrophysical objects such as white dwarf stars. Developing reliable atomic physics models at these conditions, benchmarked by experimental data, is crucial to an improved understanding of radiation transport in both stars and inertial fusion targets. However, detailed spectroscopic measurements at these conditions are rare, and traditional collisional-radiative-equilibrium (CRE) models,[1] based on isolated-atom calculations and *ad hoc* continuum lowering models, have proved questionable at and beyond solid density, leaving open the possibility for more-accurate methods.

Reported here are x-ray spectroscopy measurements at gigabar pressures using laser-driven implosions. These measurements are used to test a density functional theory (DFT)-based multiband kinetic model (*VERITAS*), which was developed in this work. The *VERITAS* model uses DFT-derived band (atomic level) information to compute the radiative transition rates that can be coupled to the radiation transfer equation to describe the radiation generation and transport processes in a dense plasma. With Cu (as a witness element) doped inside a 30-μm-thick plastic shell implosion, time-integrated and time-resolved Cu K_α emission and 1s–2p absorption measurements during shell stagnation were performed. These observations are directly connected to the time-dependent atomic ionization balance in the assembled dense plasma. The system is further constrained by integrated measurements of the compressed areal density (ρR), neutron yield, bang time, and ion temperature, allowing the spectroscopic data to differentiate the DFT-based kinetic model from traditional treatments based on isolated-atom calculations and *ad hoc* continuum-lowering models.

DRACO-simulated dynamic plasma conditions was used to investigate x-ray generation and transport through the target using two CRE models (*ATBASE* and *FAC*) and the DFT-based kinetic code *VERITAS*. The predicted time-integrated spectra are compared with the experimental measurements in Fig. 1, in which the x-ray signal is plotted as a function of photon energy (all normalized to the continuum signal level at 7800 eV). The experimental spectra [Fig. 1(b); target is shown as inset in Fig. 1(b)] show both the pronounced K_α emission peaked at ~8042 eV and the 1s–2p absorption of Cu in the higher-photon energy range of 8100 to 8250 eV. Both the location and amplitude of the emission and absorption features are appropriately captured by *VERITAS* [Fig. 1(a)].

Figures 1(c) and 1(d) show the *Spect3D* simulation results in which either the atomic database (*ATBASE*) or the flexible atomic code (*FAC*) calculations are combined with the Ecker–Kroll and Stewart–Pyatt continuum-lowering models. When these CRE results are compared to experiments, they give a conflicting conclusion about the continuum-lowering model. Namely, the experimental emission and absorption features are qualitatively reproduced by the two CRE simulations of "*ATBASE* + Stewart–Pyatt" and "*FAC* + Ecker–Kroll" in Figs. 1(d) and 1(e) (although the emission peaks are too high), while the other two combinations

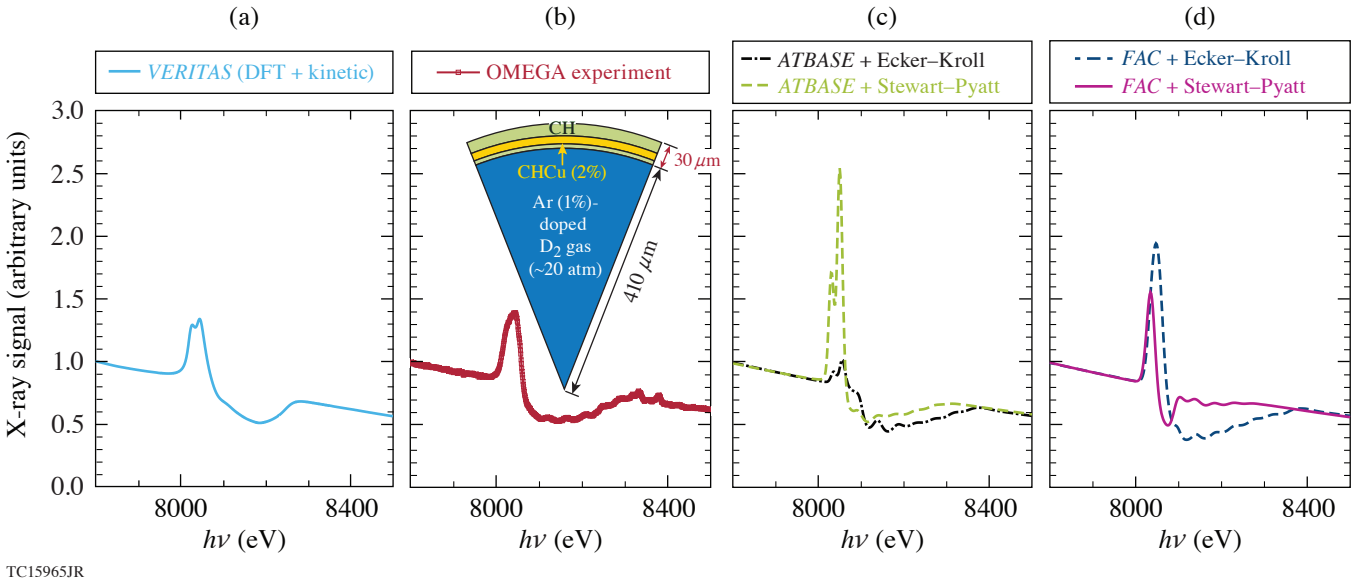

Figure 1
Comparisons of time-integrated x-ray spectra: (a) *VERITAS* DFT model prediction for the time-integrated K_α emission and 1*s*–2*p* absorption signals from a laser-driven implosion with a Cu-doped plastic layer. The model prediction is compared to (b) OMEGA experimental data, (c) CRE model predictions using the atomic database *ATBASE* in combination with Stewart–Pyatt and Ecker–Kroll continuum-lowering models, and (d) CRE model predictions using the *FAC* code with two different continuum-lowering models.

drastically disagree with experiments. This illustrates again the dilemma of the traditional spectroscopic treatment for warm dense plasmas: which *ad hoc* continuum-lowering model works better depends on the atomic physics model that is invoked. The resemblance between the *FAC* + Ecker–Kroll model [Fig. 1(d)] and experiments is likely coincidental since other recent measurements of ionization-potential depression have defied the Ecker–Kroll model. Overall, the DFT-based *VERITAS* model,[2] without invocation of an *ad hoc* continuum lowering model, better resembles the observed x-ray signal in the experiments. Nonetheless, one can see that the *VERITAS*-predicted continuum slope, the K_α-emission amplitude, and the 1*s*–2*p* absorption width are still slightly mismatched with respect to the experiment.

To summarize, a theoretical and experimental study of atomic physics in Cu-doped plastic at several billion atmospheres of pressure has been performed. Overall, a DFT-based approach reproduces many of the emission and absorption features that are observed in the experiment, while traditional plasma spectroscopy treatments show sensitivity to the combination of atomic physics and continuum-lowering models that are implemented. This sensitivity contributes to the present open questions on the validity of *ad hoc* continuum-lowering models. This work indicates the necessity for a self-consistent treatment of dense plasma effects on altering atomic energy levels/bands and their populations at ultrahigh pressures. The DFT-based *VERITAS* approach, with potential future benchmarks using other buried metal and metal-alloy layers, could provide a reliable way for simulating radiation generation and transport in dense plasmas encountered in stars and inertial fusion targets. The experimental scheme reported here, based on a laser-driven implosion, can be readily extended to a wide range of materials in single- and multishell geometries, opening the way for far-reaching investigations of extreme atomic physics and DFT models at tremendous pressures.

This material is based upon work supported by the Department of Energy National Nuclear Security Administration under Award Number DE-NA0003856, the University of Rochester, and the New York State Energy Research and Development Authority.

1. J. J. MacFarlane *et al.*, High Energy Density Phys. **3**, 181 (2007).
2. S. X. Hu *et al.*, Nat. Commun. **13**, 6780 (2022).

Effective Drift Velocity from Turbulent Transport by Vorticity

H. Yin,[1] H. Aluie,[1,2] S. Rai,[1] A. Lees,[1,2] D. Zhao,[1] S. M. Griffies,[3] A. Adcroft,[3] and J. K. Shang[1,2]

[1]Department of Mechanical Engineering, University of Rochester
[2]Laboratory for Laser Energetics, University of Rochester
[3]NOAA/Geophysical Fluid Dynamics Laboratory and Princeton University Program in Atmospheric and Oceanic Sciences

Highlighted here are the differing roles of vorticity and strain in the transport of coarse-grained scalars at length-scales larger than l by smaller-scale (subscale or subgrid or unresolved) turbulence. We use the first term in a multiscale gradient expansion due to Eyink,[1] which exhibits excellent correlation with the exact subscale physics when the partitioning length l is any scale smaller than that of the spectral peak. We show that unlike subscale strain, which acts as an anisotropic diffusion/anti-diffusion tensor, subscale vorticity's contribution is solely a conservative advection of coarse-grained quantities by an eddy-induced non-divergent velocity, $\mathbf{v}_*$, that is proportional to the curl of vorticity. Therefore, material (Lagrangian) advection of coarse-grained quantities is accomplished not by the coarse-grained flow velocity, $\bar{\mathbf{u}}_l$, but by the effective velocity, $\bar{\mathbf{u}}_l + \mathbf{v}_*$, the physics of which may improve hydrodynamic modeling.

Basic considerations from fluid dynamics indicate that the distance between particles in a laminar flow is determined by the strain.[2] Vorticity merely imparts a rotation on their separation vector $\mathbf{r}$ without affecting its magnitude. This behavior can be seen by considering the velocity, $\mathbf{u}$, difference between particles P and Q at positions $\mathbf{x}$ and $\mathbf{x} + \mathbf{r}$, respectively,

$$\mathbf{u}_Q - \mathbf{u}_P = \delta\mathbf{u} = \mathbf{u}(\mathbf{x}+\mathbf{r}) - \mathbf{u}(\mathbf{x}) = \mathbf{r}\cdot\nabla\mathbf{u}\,\big|_{\mathrm{x}} + ..., \tag{1}$$

where a Taylor-series expansion is justified for short distances $|\mathbf{r}|$ over which the flow is sufficiently smooth. In the Lagrangian frame of P at $\mathbf{x}$, the separation from Q evolves as

$$\frac{D\mathbf{r}}{Dt} = \delta\mathbf{u} = \mathbf{r}\cdot\mathbf{S} + \underbrace{\mathbf{r}\cdot\boldsymbol{\Omega}}_{\frac{1}{2}\boldsymbol{\omega}\times\mathbf{r}}, \tag{2}$$

where the velocity gradient tensor, $\nabla\mathbf{u} = \mathbf{S} + \boldsymbol{\Omega}$, has been decomposed into the symmetric strain rate tensor $\mathbf{S} = \left[\nabla\mathbf{u} - (\nabla\mathbf{u})^T\right]/2$ and the antisymmetric vorticity tensor $\boldsymbol{\Omega} = \left[\nabla\mathbf{u} - (\nabla\mathbf{u})^T\right]/2 = -1/2\epsilon_{ijk}\omega_k$. Here, $\boldsymbol{\omega} = \nabla \times \mathbf{u}$ is vorticity and ϵ_{ijk} is the Levi–Civita symbol. Taking an inner product of Eq. (2) with $\mathbf{r}$,

$$\frac{1}{2}\frac{D|\mathbf{r}|^2}{\mathrm{d}t} = \mathbf{r}\cdot\mathbf{S}\cdot\mathbf{r}, \tag{3}$$

shows that the distance is determined by the strain. Vorticity in Eq. (2) only acts to rotate $\mathbf{r}$ without changing its magnitude.

These considerations hinge on the critical assumption that the flow is sufficiently smooth over separation $\mathbf{r}$, which is patently invalid in a turbulent flow for $\mathbf{r}$ at inertial scales.[3] However, a version of this story survives due to the property of scale locality,[4] which justifies an expansion in scale. The main result of this research is Eq. (4),

$$\partial_t \overline{C}_l + \nabla \cdot \left[\left(\overline{\mathbf{u}}_l + \mathbf{v}_* \right) \overline{C}_l \right] = -\nabla \cdot \left[\mathbf{J}(C) \right], \tag{4a}$$

$$\mathbf{v}_* = \frac{1}{2} A l^2 \nabla \times \left(\nabla \times \overline{\mathbf{u}}_l \right), \tag{4b}$$

where Eq. (4a) shows us that coarse-grained simulations in general, including those from radiation-hydrodynamics inertial confinement fusion codes, may need to solve this equation to represent the unresolved (subgrid) vorticity physics self-consistently. Equation (4b) is an expression for the eddy-induced advection velocity $\mathbf{v}_*$ affecting length scales larger than l, which may be the grid cell size in a simulation. In Eq. (4a), $\mathbf{J}(C)$ can represent traditional subgrid models such as turbulent diffusion,[5] $\mathbf{J}(C) = -\alpha_{\text{turb}} \nabla \overline{C}_l$.

In summary, it is shown that unlike subscale strain, which acts as an anisotropic diffusion/anti-diffusion tensor, subscale vorticity's contribution at leading order is solely a conservative advection of coarse-grained scalars by an eddy-induced velocity $\mathbf{v}_*$ proportional to the curl of vorticity. Evidence of excellent agreement between the leading order terms and the exact ones from a 3-D compressible turbulence simulation are shown in Fig. 1. While the focus of this summary was on the transport of scalars, a similar analysis may also apply to the transport of momentum. Since the convergence of Eyink's expansion and, therefore, the dominance of the leading order term relies on ultraviolet scale locality,[4] these results and conclusions may not hold at length scales larger than those of the spectral peak. In other words, for coarse-grained simulations to use this modeling framework, they need to directly resolve the most energetic scales. Otherwise, some of the assumptions may not be valid. Note that the unresolved (subgrid) scales can still have the dominant vorticity contribution since energy and vorticity can occupy different scale ranges.

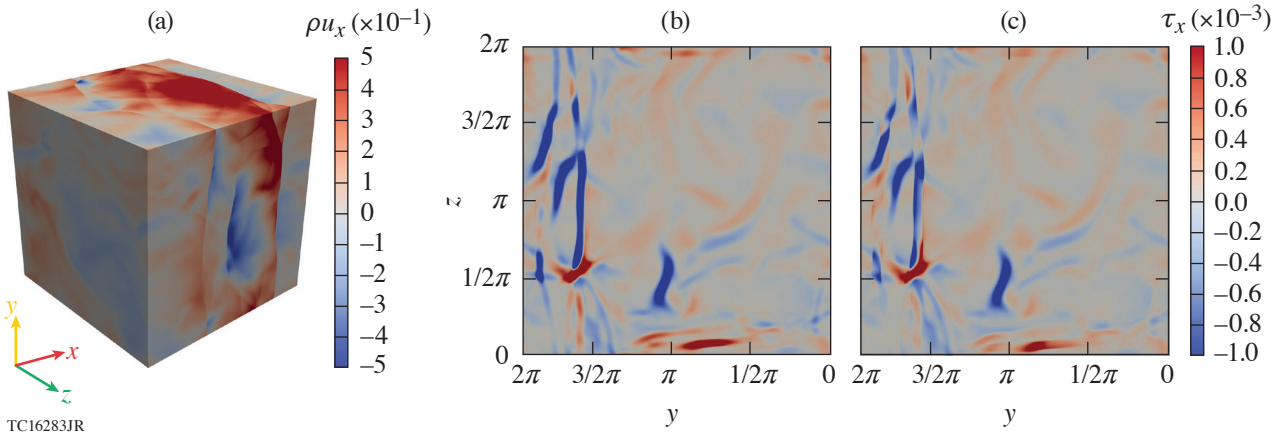

Figure 1
(a) Visualization of x component of momentum, ρu_x, in physical space from the 1024^3 compressible turbulence direct numerical simulation (DNS). The image is shown at an instant of time after the flow has reached steady state. Shocks can be seen as discontinuities. [(b),(c)] A 2-D slice at $x = 0$ from a snapshot of the 3-D compressible turbulence DNS, comparing the (b) exact $\overline{\tau}_l(u_x, \rho)$ at $l = 0.19635$ with (c) its approximation $\tau_m = 1/3 M_2 l^2 \partial_k \overline{\rho} \partial_k \overline{u}_x$.

This research was funded by U.S. DOE grant DE-SC0020229. Partial support from U.S. NSF grants PHY-2020249, OCE-2123496, U.S. NASA grant 80NSSC18K0772, and U.S. NNSA grant DE-NA0003856 is acknowledged.

1. G. L. Eyink, J. Fluid Mech. **549**, 159 (2006).
2. P. K. Kundu, I. M. Cohen, and D. R. Dowling, *Fluid Mechanics*, 6th ed. (Elsevier, 2016).
3. S. B. Pope, *Turbulent Flows* (Cambridge University Press, Cambridge, 2000).
4. H. Aluie, Phys. Rev. Lett. **106**, 174502 (2011).
5. J. Smagorinsky, Mon. Weather Rev. **91**, 99 (1963).

Development of an X-Ray Radiography Platform to Study Laser-Direct-Drive Energy Coupling at the National Ignition Facility

L. Ceurvorst,[1] W. Theobald,[1,2] M. J. Rosenberg,[1] P. B. Radha,[1] C. Stoeckl,[1] R. Betti,[1,2] K. S. Anderson,[1] J. A. Marozas,[1] V. N. Goncharov,[1,2] E. M. Campbell,[1] C. M. Shuldberg,[3] R. W. Luo,[3] W. Sweet,[3] L. Aghaian,[3] L. Carlson,[3] B. Bachmann,[4] T. Döppner,[4] M. Hohenberger,[4] K. Glize,[5] R. H. H. Scott,[5] A. Colaïtis,[6] and S. P. Regan[1,2]

[1]Laboratory for Laser Energetics, University of Rochester
[2]Department of Mechanical Engineering, University of Rochester
[3]General Atomics
[4]Lawrence Livermore National Laboratory
[5]Central Laser Facility, STFC Rutherford Appleton Laboratory
[6]Centre Lasers Intenses et Applications, Université de Bordeaux-CNRS-CEA

The coupling of laser energy to an imploding target in direct-drive inertial confinement fusion (ICF) is a key parameter that determines the ablation pressure and the implosion velocity of the shell. According to current models, cross-beam energy transfer (CBET) is a major factor that limits the ablation pressure on National Ignition Facility (NIF)-scale targets, reducing implosion velocity and shell kinetic energy. Hence, accurate measurements of the laser coupling efficiency for NIF-scale implosions are an important aspect of direct-drive ICF research. To obtain these measurements, a platform was developed on the NIF using x-ray radiography and self-emission imaging to diagnose the evolution of a directly driven solid spherical target. This plastic (CH) sphere was driven by 184 NIF beams in polar direct drive at three different intensities using a 7-ns ramp pulse. The remaining eight NIF beams were focused onto a copper backlighting foil to generate x rays that probed the target before being collected by a pinhole array coupled to a gated x-ray detector. This summary details the analysis technique used to reconstruct the target's density profile from these radiographs.

In the paraxial approximation, where the x rays are roughly parallel to the optical axis, the transmission T of x rays passing through a plasma is given by:

$$T(x,y) = e^{-\tau(x,y)}$$
$$\tau(x,y) = \int \mu(x,y,z)\rho(x,y,z)\mathrm{d}z, \tag{1}$$

where τ is the optical depth, μ is the opacity, and ρ is the density. The implosions performed in these experiments are expected to remain roughly spherically symmetric, meaning that both the opacity and density should primarily be radial functions. In this limit, Eq. (1) shows that the optical depth is simply the Abel transformation of the attenuation, equal to the opacity times the density. Therefore, the radiographs can be converted to optical depth images, azimuthally averaged, and Abel inverted to yield the attenuation profiles.

To convert radiographs to optical depth images, the transmission of the target must first be inferred by dividing the raw signal by a fitted backlighter profile. Typically, this is done by fitting the unobstructed portions of the backlighter emission with an appropriate function, in this case, the superposition of two super-Gaussians. As can be seen in Fig. 1(a), however, the backlighter was largely eclipsed by the target itself, leaving little unobstructed data with which to perform the fit. Instead, the entire image was used in the calculations by multiplying the backlighter emission profile by a simplified transmission function, resulting in fits such as the one shown in Fig. 1(b). The transmission images were then obtained by dividing the raw image by the fitted backlighter emission as displayed in Fig. 1(d).

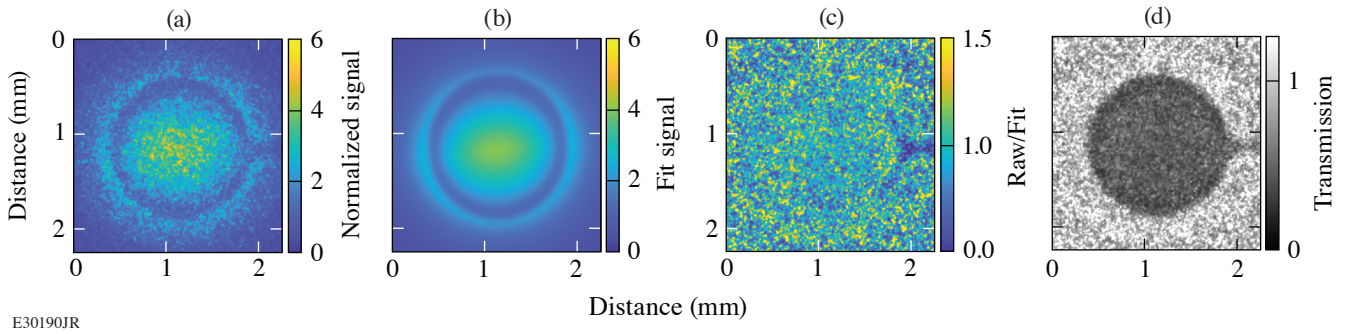

Figure 1
Converting radiographs into transmission images. (a) A single radiographic sub-image is taken from shot N210519-001 7.1 ns after the start of the drive. (b) This image is then fit with a simplified backlighter and transmission profile. (c) Dividing the raw radiograph by its fitted profile produces a flat image composed primarily of noise, confirming the quality of the fit. Note the stalk is not included in the fit and thus appears on the right side of this image. (d) The raw image is divided by the fitted backlighter profile to produce the final transmission image.

The resulting transmission was then converted to optical depth using Eq. (1), and the azimuthally averaged optical depth profiles were Abel inverted to obtain the system's radial attenuation. The final step of analysis was to separate the density and opacity profiles. Ahead of the shock, the target should not be significantly heated, maintaining its cold opacity value. After the shock, however, the material can be heated and ionized enough to reduce its overall opacity. A crude approximation was made that the opacity should be roughly constant in this shocked region, and its value was determined by matching the calculated target mass in the experiment to the accompanying *DRACO*[1] simulations. This yielded a hot opacity of 2.5±0.2 cm^2/g, similar to the 2.7 cm^2/g calculated by post-processing the simulations with *Spect3D*.[2]

Using this step function for the opacity, the final density profiles were inferred and compared to the simulations as shown in Fig. 2. The shock trajectories were in rough agreement, indicated by the rise in density. However, the subsequent fall in density corresponding to the ablation front occurred at a larger radius in the experiment compared to the simulations. This is similar to the trends seen previously with thin-shell targets.[3] At the time, the thicker observed shocked region was suspected to be caused by hydrodynamic instabilities. However, the ablation front is not accelerating here, largely eliminating this possibility.

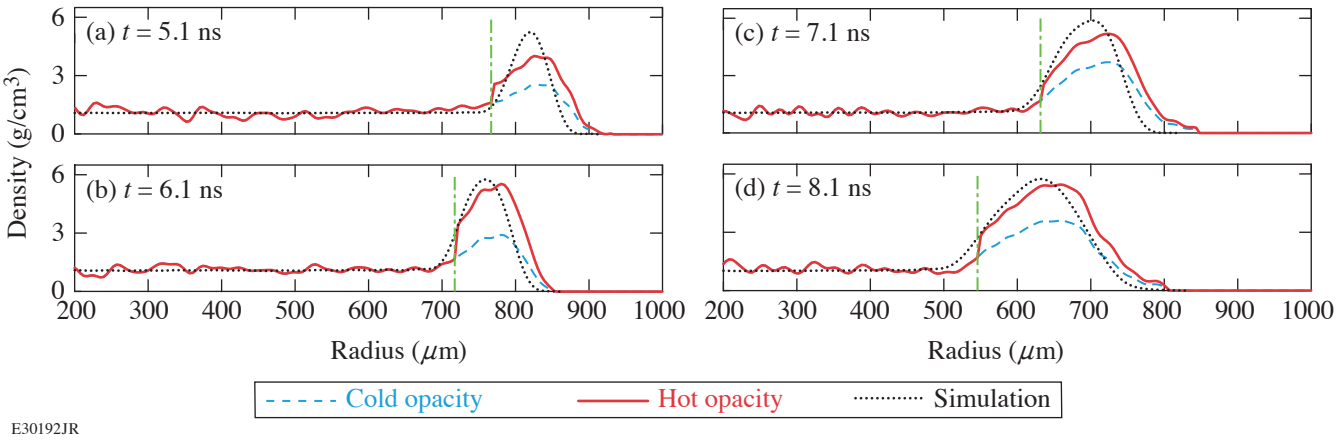

Figure 2
Inferred azimuthally averaged density profiles. The initial density calculation using only cold opacity (dashed blue curve) and mass conserving calculation using a stepped opacity profile (solid red curve) are compared to the simulated density profile convolved with the instrument response function of the system (dotted black curve) (a) 5.1 ns, (b) 6.1 ns, (c) 7.1 ns, and (d) 8.1 ns after the start of the drive. Vertical (dashed–dotted green) lines indicate the shock position beyond which the calculated hot opacity was applied.

To confirm that this discrepancy was not caused by the analysis technique, the same algorithm was applied to artificial radiographs calculated using *Spect3D*. The results of this analysis showed a 0.06 g/cm^3 rms error caused largely by the Abel inversion algorithm. As shown in Fig. 3, no shift to the reconstructed shock and ablation fronts was detected. The analysis also investigated the role of noise, which showed no systematic shift to these trajectories. The discrepancy in ablation front trajectory, therefore, appears to be physical. A comparison to simulations at all explored intensities and pulse shapes is now underway to distinguish between various effects such as preheat, CBET, and nonlocal heat-transport models. The results of this ongoing investigation will be published in a future manuscript.

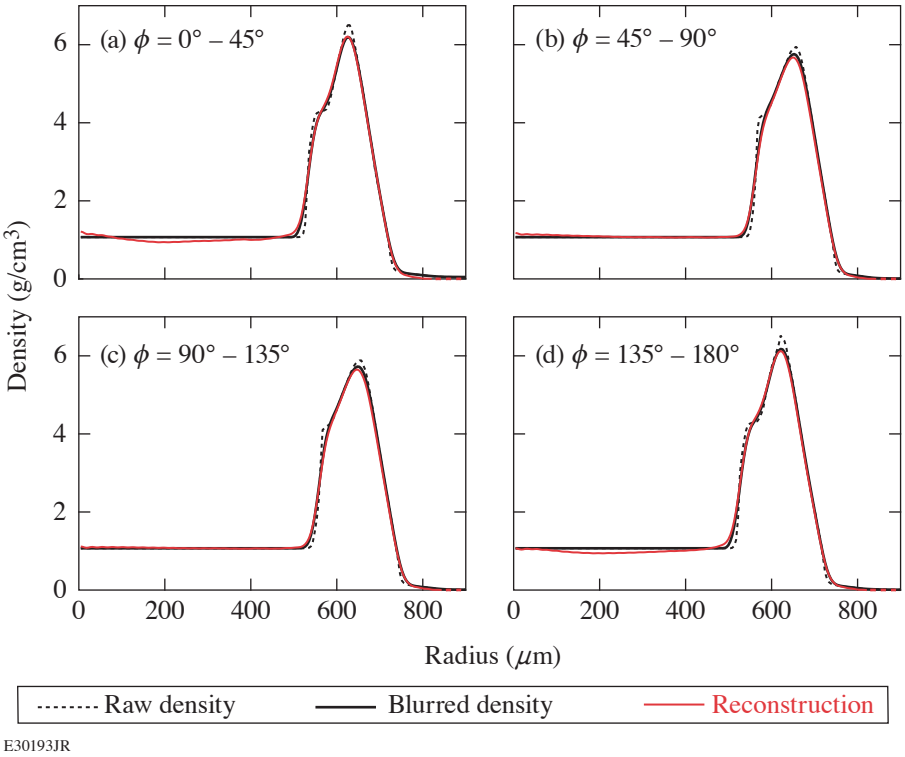

Figure 3
Validation of technique. Transmission images are calculated using *Spect3D*, and azimuthally dependent density profiles are reconstructed using this analysis technique. The data were calculated using azimuthal bins of (a) 0° to 45°, (b) 45° to 90°, (c) 90° to 135°, and (d) 135° to 180°. The reconstructed profiles (solid red curves) closely align with the original density profiles after accounting for the instrument response (solid black curves). The rms error between these two curves is 0.06 g/cm^3. Compared to the original density profile (dashed black curve), more features are lost because of imaging resolution than because of the reconstruction technique.

This material is based upon work supported by the Department of Energy National Nuclear Security Administration under Award Number DE-NA0003856, the University of Rochester, and the New York State Energy Research and Development Authority.

1. P. B. Radha *et al.*, Phys. Plasmas **23**, 056305 (2016).
2. J. MacFarlane *et al.*, High Energy Density Phys. **3**, 181 (2007).
3. M. Hohenberger *et al.*, Phys. Plasmas **22**, 056308 (2015).

A Scattered-Light Uniformity Imager for Diagnosing Laser-Absorption Asymmetries on OMEGA

D. H. Edgell, J. Katz, R. Raimondi, D. Turnbull, and D. H. Froula

Laboratory for Laser Energetics, University of Rochester

Successful implosions require efficient and highly uniform deposition of laser energy. Simulations suggest that the nonuniformity must be below the 1% rms level to achieve ignition.[1] Accurate measurement of the laser absorption is essential to evaluate implosion performance, including various schemes to mitigate laser–plasma instability losses. Laser light scattered from a target is the most direct measurement for diagnosing laser absorption in a direct-drive implosion. Observations from OMEGA implosions have shown much larger scattered-light asymmetries than standard predictions.[2,3] To address the insufficiencies of the existing scattered-light instruments, a new diagnostic, the scattered-light uniformity imager (SLUI), has been designed and deployed on OMEGA to absolutely measure the scattered-light intensity and nonuniformity for the purpose of diagnosing the asymmetry and determining its effect on laser drive uniformity. SLUI's collect a much larger portion of the scattered light around the target than other diagnostics.

SLUI measures the angularly discriminated scattered-light intensity distribution over a collection cone area by imaging a translucent transmission diffuser plate using a charge-coupled–device (CCD)/lens assembly There are two major assemblies in each SLUI: the diffuser plate front-end ten-inch manipulator (TIM)-based payload and a rear-end imaging assembly [Fig. 1(a)]. The main component of the front end is the 0.5-mm-thick translucent white spectralon diffuser plate. A stray light baffle, debris shield, and antireflection absorbing filter are also incorporated into the diagnostic payload inserted into the target chamber. The imaging part of the diagnostic (light baffle, vacuum window, filters, lens, and CCD camera) is located outside the target chamber. A sample diffuser image is shown in Fig. 1(b). Fine-scale structures, such as highlighted by the inset, are believed to be caused by structure in the diffuser plate. Some large-scale variances over the image may also be caused by the diffuser plate nonuniformity. The fine- and large-scale diffuser effects will be clarified by upcoming flat-fielding measurements. Each SLUI instrument sensitivity is absolutely calibrated offline using a National Institute of Standards and Technology traceable photodiode.

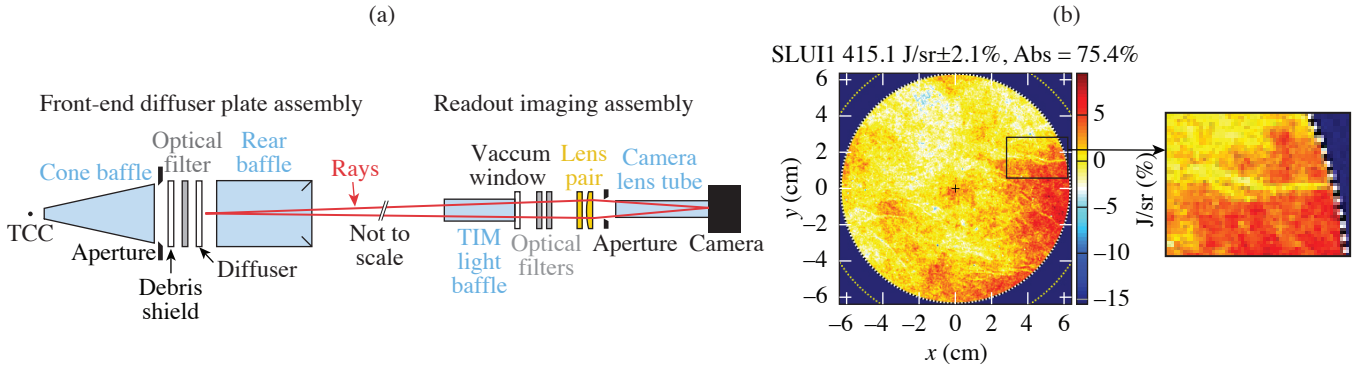

Figure 1
(a) The SLUI diagnostic. (b) Sample SLUI image of the diffuser plate for an OMEGA implosion. The inset highlights one of the small-scale features that are caused by the interior structure of the diffuser plate. TCC: target chamber center.

The standard operating position of the SLUI's places the diffuser plate standoff distance (SOD) at 31.5 cm from target chamber center (TCC) to avoid any chance of beam interference and helps reduce sputtering of baffle material on high-power shots. At this SOD, a SLUI has an effective *f* number of 2.5 and records the scattered light over a cone angle of 11.3° or ~0.97% of the total 4π emission area. Based on the measured point spread function, this effective area provides over 20K independent intensity measurements, enabling the study of the intensity and distribution of the scattered light over this area. Five SLUI's have been built and deployed in OMEGA's TIM diagnostic ports, covering almost 5% of the emission surface, enabling an absolute scattered-light measurement that according to modeling should be within a few percent of the global average. Five SLUI positions allowed resolution of the lowest modes (ℓ = 1,2) in the distribution. The large solid-angle image from each SLUI records the large local slopes in the distribution due to higher modes. Work is underway using these measured variations to evaluate the accuracy of the predicted scattered-light distributions and identify whether additional physics or other considerations need to be included.

The accuracy of the SLUI's measurements are sufficient to distinguish the effects of a 12-μm offset in target position. The green squares in Fig. 2 show the laser absorption inferred from each SLUI for an implosion that was centered at TCC within a couple of microns. The variation between the SLUI's is indicative of the scattered-light variation over the target chamber. The mean absorption for this shot is shown by the dotted black line. The blue diamonds are the laser absorptions inferred from SLUI from a similar implosion except that the target was intentionally offset 12 μm toward one of the SLUI's. The difference between the two implosions is illustrated by the red line. A consistent trend is found with a delta of about 5% absorption difference between the SLUI toward the offset and the SLUI away from the offset.

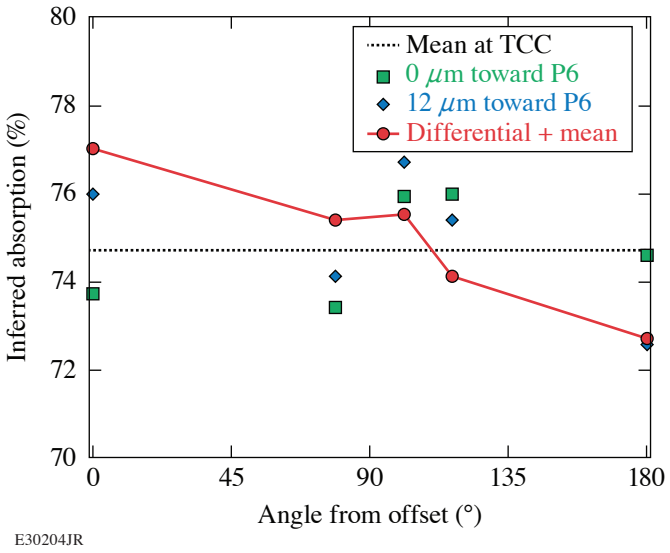

Figure 2
SLUI experimental measurements show the effect of a target offset. Shown is the laser absorption inferred for individual SLUI's for two similar implosions, one well centered at TCC (green squares) and the other intentionally offset ~12 μm toward one of the SLUI's (blue diamonds). The red line shows the difference between the two measurements centered on the mean overall absorption for the case at TCC (dotted black line).

The SLUI diagnostic is now available for deployment on OMEGA implosions, providing an absolutely calibrated platform to study the global laser absorption and sources of scattered-light and absorption asymmetries such as beam pointing, target offset, power balance, and polarization effects on cross-beam energy transfer.

This material is based upon work supported by the Department of Energy National Nuclear Security Administration under Award Number DE-NA0003856, the University of Rochester, and the New York State Energy Research and Development Authority.

1. V. N. Goncharov *et al.*, Plasma Phys. Control. Fusion **59**, 014008 (2017).
2. D. H. Edgell *et al.*, Phys. Rev. Lett. **127**, 075001 (2021).
3. O. M. Mannion *et al.*, Phys. Plasmas **28**, 042701 (2021).

Three-Dimensional Hot-Spot X-Ray Emission Tomography from Cryogenic Deuterium–Tritium Direct-Drive Implosions on OMEGA

K. Churnetski,[1,2] K. M. Woo,[1] W. Theobald,[1,2] P. B. Radha,[1] R. Betti,[1,2,3] V. Gopalaswamy,[1] I. V. Igumenshchev,[1] S. T. Ivancic,[1] M. Michalko,[1] R. C. Shah,[1] C. Stoeckl,[1] C. A. Thomas,[1] and S. P. Regan[1,2]

[1]Laboratory for Laser Energetics, University of Rochester
[2]Department of Mechanical Engineering, University of Rochester
[3]Department of Physics and Astronomy, University of Rochester

In direct-drive inertial confinement fusion (ICF),[1] laser beams are focused onto a spherical target to implode a thin shell composed of an outer ablation layer (typically plastic) and an inner layer of solid cryogenic deuterium–tritium (DT) fuel. The laser-direct-drive ICF concept is studied on the 60-beam, 30-kJ, 351-nm OMEGA laser,[2] which has produced high-performing implosions with hot-spot pressures exceeding 50 Gbar, described in Ref. 3. The recent application of statistical modeling significantly improved the implosion performance and the neutron yield.[4] Low-mode drive variations in the driver illumination and from target perturbations can significantly impact implosions.[5–7] The goal over the next several years is to further optimize OMEGA implosions and to demonstrate ignition-relevant implosions that when scaled to 2 MJ of laser energy, would enter the burning-plasma regime.[8,9] Three-dimensional hot-spot x-ray emission tomography is a powerful tool to diagnose low-mode asymmetries, which will help to mitigate low-mode perturbations and improve implosion performance. This work is embedded in a long-term project that aims to understand the physics and multidimensional effects that currently limit the hot-spot pressure in ICF implosions on OMEGA and to help to develop strategies to increase the hot-spot pressure.

OMEGA currently has a combination of time-gated and time-integrated x-ray diagnostics for hot-spot imaging along four lines of sight (LOS), which enable a 3-D interpretation of the hot-spot shape. These diagnostics include KBframed,[10] the single line-of-sight, time-resolved x-ray imager (SLOS-TRXI),[11] KB (formerly GMXI),[12] and a spatially resolved electron temperature diagnostic (SR-TE).[13] The diagnostics have different spatial and temporal resolutions, as well as slightly different spectral sensitivities. These four diagnostics are quasi-orthogonal from each other, allowing for a 3-D view of the imploding ICF core. Figure 1 shows the locations of the detectors on the OMEGA target chamber and example data from each detector.

A 3-D hot-spot emission model was developed to reconstruct the hot-spot emission profile of direct-drive implosions on OMEGA by combining the measured x-ray emission data from multiple LOS.[14] The radiation transfer equation along a single LOS is considered for a steady-state plasma in which the temperature and density distributions and the radiation field are independent of time.[15] The hot-spot plasma of cryogenic DT target implosions on OMEGA is optically thin for photon energies >2.5 keV. All of the x-ray imagers considered here satisfy this condition and absorption can be neglected.[13] Neither the absolute signal nor the temporal evolution of the hot-spot emission are taken into account in this simplified model. The spectral response is assumed to be the same for all the x-ray imagers. Using those simplifications and dropping the frequency dependence on the plasma emissivity ε, the projected x-ray image $I_{\hat{s}}$ along an observation direction $\hat{s}$ over a path length s is given by $I_{\hat{s}} \sim \int_{\hat{s}} \varepsilon \mathrm{d}s$.

A method described in Woo *et al.*[14] has been developed to reconstruct ε through a complete expansion set using both non-orthogonal polynomial and orthogonal polynomial expansions. The complex shape of the hot-spot emission can be described in terms of a model of generalized spherical-harmonic Gaussian functions,

$$\ln \varepsilon(r,\theta,\varphi) = \sum_{n=0}^{\infty} \sigma_n R^n \left[1 + \sum_{\ell=1}^{\infty} \sum_{m=-\ell}^{\ell} \sum_{k=0}^{\infty} A_{\ell m k} R^k Y_{\ell m}(\theta,\varphi)\right]^n. \quad (1)$$

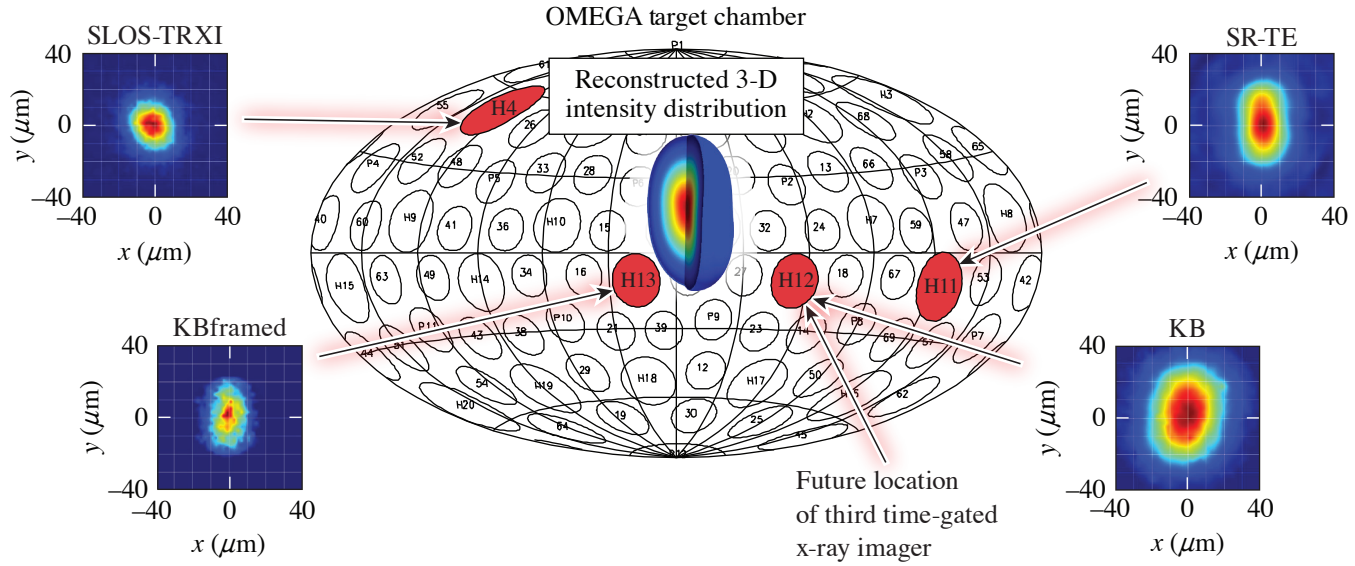

Figure 1
The locations of the existing four hot-spot x-ray imaging detectors on the OMEGA target chamber are indicated by the red circles. SLOS-TRXI is located in port H4 (45°, 234°), KBframed in port H13 (105°, 342°), KB in port H12 (96°, 54°), and SR-TE in port H11 (101°, 134°). The future third time-gated x-ray imager will also be located in port H12 (96°, 54°). Example data are shown for each diagnostic and the reconstructed 3-D hot-spot emission is displayed in the target chamber center. The polar and azimuthal angles for each detector are denoted in parenthesis.

The emissivity is described in spherical coordinates (r, θ, φ), where the origin of the coordinate system coincides with the peak of ε. In Eq. (1), R is the radius and $Y_{\ell,m}$ are the real spherical harmonic functions. The expansion coefficients, φ_n and $A_{\ell,m}$, are determined by a gradient-descent, machine-learning algorithm that minimizes a loss function, which is the fit error between the model and the normalized measured x-ray images.

To reconstruct the emission profile, an initial estimate is made for the solution of of ε, which is a 1-D Gaussian profile. This model is projected into the LOS of the x-ray detectors using a ray-tracing routine and the projections are compared with the experimental x-ray images from each diagnostic. The error between the model and the experimental images is calculated as the sum of the root-mean-square (rms) difference over the multiple lines of sight. The coefficients of the model are slightly perturbed, and this process is repeated for several iterations until the rms error is minimized.

Proof-of-principle simulations with the hydrodynamic code *DEC3D*[16] assuming a mode-2 perturbation were used to validate the 3-D reconstruction procedure. The result of the simulation was post-processed with the detector resolutions and spectral sensitivities using *Spect3D*[17] to create simulated x-ray images along the four lines of sight. Normally distributed random noise was added to the simulated x-ray images, and the hot-spot emission was reconstructed multiple times in a Monte Carlo simulation by varying the noise. The resulting 3-D reconstructions were projected along the detector lines of sight and the major and minor radii were calculated at the 1/e contour level for the reconstruction projections and simulated x-ray images. The radii agreed within the error bars, which gives confidence in the viability of this technique.

A direct-drive ICF campaign on OMEGA was conducted with deliberate laser-drive asymmetries to study the effect of hot-spot shape asymmetries on implosion performance. The polar-direct drive (PDD)[18] beam illumination geometry was applied by using 40 of the 60 OMEGA beams, switching off 20 beams around the equator. The 40 beams are grouped in three beam rings in the upper and lower hemisphere according to their polar angles.[18] The partition of beam energies in rings 1 and 3 was varied while keeping the total laser energy constant. The magnitude of the laser-drive asymmetry was varied to produce hot spots that

ranged from oblate to prolate in shape. Figure 2 shows data from three shots at stagnation from KBframed, which has an equatorial view of the capsule. Reconstructions were done for each shot during this campaign and compared to the experimental inputs.

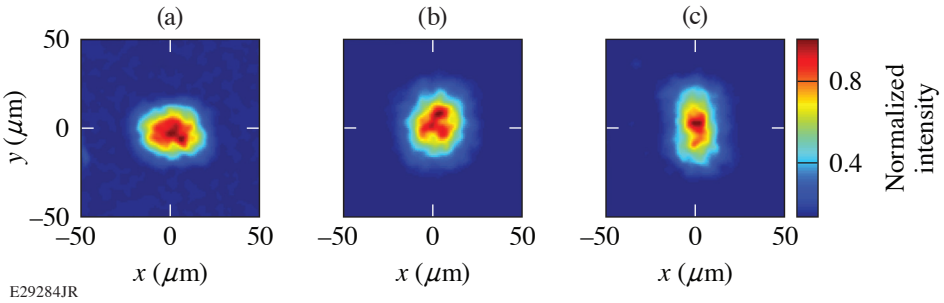

Figure 2
Experimental x-ray images from the KBframed diagnostic at stagnation of cryogenic DT target implosions performed with the PDD illumination geometry. The beam-energy balance was varied from a stronger drive on (a) the poles (shot 96578), to (b) a balanced drive (shot 96575), to (c) a stronger drive on the equator (shot 96581), while keeping the total laser energy conserved.

The reconstruction of shot 96581 is shown in Fig. 1. Data from SLOS-TRXI and KBframed are chosen to be from the time of peak emission, and data from KB channel 3 and SRTE channel 1 are used due to the similar energy ranges to those of SLOS-TRXI and KBframed. The differences in hot-spot size between the different diagnostics can be attributed to differences in time resolution. With a higher intensity of laser energy incident at the equator of the capsule, a prolate shape is expected in the hot-spot emission with the major axis aligned with the z axis of the target chamber. Spherical harmonic modes up to $\ell = 3$ were used in the reconstruction. The large $A_{2,0} = -0.47 \pm 0.03$ expansion coefficient indicates a strong mode $\ell = 2$ in the reconstruction, which can be seen in the experimental x-ray images. The $A_{2,0}$ coefficient is negative, which indicates a prolate shape and is consistent with what we expect from the laser-drive asymmetry. Reconstructions of other shots from this campaign also show the expected overall shape and orientation of the hot spot based on the laser-drive asymmetry and will be further discussed in a future publication.

This material is based upon work supported by the Department of Energy National Nuclear Security Administration under Award Number DE-NA0003856, the University of Rochester, and the New York State Energy Research and Development Authority.

1. R. S. Craxton *et al.*, Phys. Plasmas **22**, 110501 (2015).
2. T. R. Boehly *et al.*, Opt. Commun. **133**, 495 (1997).
3. S. P. Regan *et al.*, Phys. Rev. Lett. **117**, 025001 (2016); 059903(E) (2016).
4. V. Gopalaswamy *et al.*, Nature **565**, 581 (2019).
5. B. K. Spears *et al.*, Phys. Plasmas **21**, 042702 (2014).
6. O. M. Mannion *et al.*, Phys. Plasmas **28**, 042701 (2021).
7. H. G. Rinderknecht *et al.*, Phys. Rev. Lett. **124**, 145002 (2020).
8. O. A. Hurricane *et al.*, Phys. Plasmas **26**, 052704 (2019).
9. A. B. Zylstra *et al.*, Nature **601**, 542 (2022).
10. F. J. Marshall *et al.*, Rev. Sci. Instrum. **88**, 093702 (2017).)
11. W. Theobald *et al.*, Rev. Sci. Instrum. **89**, 10G117 (2018).
12. F. J. Marshall and J. A. Oertel, Rev. Sci. Instrum. **68**, 735 (1997).
13. D. Cao *et al.*, Phys. Plasmas **26**, 082709 (2019).
14. K. M. Woo *et al.*, Phys. Plasmas **29**, 082705 (2022).
15. Ya. B. Zel'dovich and Yu. P. Raizer, *Physics of Shock Waves and High-Temperature Hydrodynamic Phenomena*, edited by W. D. Hayes and R. F. Probstein (Dover, Mineola, NY, 2002).

16. K. M. Woo *et al.*, Phys. Plasmas **25**, 102710 (2018).
17. J. J. MacFarlane *et al.*, High Energy Density Phys. **3**, 181 (2007).
18. P. B. Radha *et al.*, Phys. Plasmas **19**, 082704 (2012).

A New Neutron Time-of-Flight Detector for Yield and Ion-Temperature Measurements at the Omega Laser Facility

V. Yu. Glebov,[1] C. J. Forrest,[1] J. Kendrick,[1] J. P. Knauer,[1] O. M. Mannion,[2] H. McClow,[1] S. P. Regan,[1] C. Stoeckl,[1] B. Stanley,[1] and W. Theobald[1]

[1]Laboratory for Laser Energetics, University of Rochester
[2]Sandia National Laboratories

A new neutron time-of-flight (nTOF) detector for deuterium–deuterium (D–D) fusion yield and ion-temperature measurements was designed, installed, and calibrated for the OMEGA Laser System. This detector provides an additional line of sight for D–D neutron yield and ion-temperature measurements for yields exceeding 1×10^{10} with higher precision than existing detectors. The nTOF detector consists of a 90-mm-diam, 20-mm-thick BC-422 scintillator and a gated Photek[1] photomultiplier tube (PMT240). This PMT has a 40-mm-diam photocathode, two microchannel plates, and provides a gain of up to 1×10^6. For DD measurements the PMT240 is operated at a bias voltage of –4.4 kV, corresponding to a PMT gain of 2×10^5. The PMT collects scintillating light through the 20-mm side of the scintillator without the use of a light guide. There is no lead shielding from hard x rays in order to allow the x-ray instrument response function of the detector to be easily measured. Instead, hard x-ray signals generated in implosion experiments are gated out by the PMT. The design provides a place for glass neutral-density (ND) filters between the scintillator and the PMT to avoid PMT saturation at high yields. The nTOF detector is installed in the OMEGA Target Bay along the P8A sub-port line of sight (LOS) with $\theta = 109.57°$ and $\phi = 90.00°$ (where θ and ϕ are the polar and azimuthal angles of the port in the target chamber coordinate system) at a distance of 5.3 m from the target chamber center. This detector is named P8A 5.3-m nTOF.

Until recently only two nTOF detectors on OMEGA [5.4-m nTOF (Ref. 2) located at 5.4 m from target chamber center (TCC) in sub-port H10G LOS with $\theta = 84.98°$ and $\phi = 311.76°$ and 12-m nTOFL (Ref. 3) located at 12.4 m from TCC in sub-port H8A LOS with $\theta = 87.86°$ and $\phi = 161.24°$] measured the D–D yield and ion temperature above the 2×10^{10} yield. The P8A 5.3-m nTOF detector provided an additional line of sight and increased the yield range of DD measurements on OMEGA. The P8A nTOF has a larger scintillator volume and records more neutron interactions than the other two detectors. The DD yield calibration of the P8A nTOF against the 12-m nTOFL detector is shown in Fig. 1. Only shots with yields exceeding 1×10^{10} were selected for the calibration. Figure 1(a) shows the charge of the neutron signal from P8A nTOF plotted versus the DD yield from the 12-m nTOF. The line in Fig. 1(a) is the linear fit of the data that is forced to go through the point (0,0). Figure 1(a) demonstrates a good linearity of the P8A nTOF detector signal for D–D yields up to 4×10^{11}. The data in Fig. 1 were recorded without an ND filter. When an ND filter is used there is practically no upper limit in D–D yield measurement for the P8A nTOF detector. Figure 1(b) shows the ratio of the yields from the two detectors as a function of the shot number.

Most of the LLE implosion campaigns are designed for DT yields in the range from 1×10^{13} to 1×10^{14} and recently for yields above 3×10^{14}. Therefore, the DT nTOF detectors on OMEGA were designed for such high yields. External OMEGA users, however, sometimes require DT yield measurements from 5×10^{10} to 1×10^{12}. The PMT high-voltage setting of P8A nTOF is adjusted from –4.4 kV for DD operation to –3.6 kV, corresponding to a PMT gain of 6×10^3 for the DT operation. The P8A nTOF was calibrated in DT yield against Cu activation. Figure 2(a) shows the charge of the neutron signal from P8A nTOF plotted versus the DT yield from Cu activation. The straight line in Fig. 2(a) is the linear fit of the data that is forced to go through the point (0,0). Figure 2(a) demonstrated that P8A nTOF is linear in desired DT yield range from 5×10^{10} to 1×10^{12}. Figure 2(b) shows the ratio of the yields from the two detectors as a function of shot number.

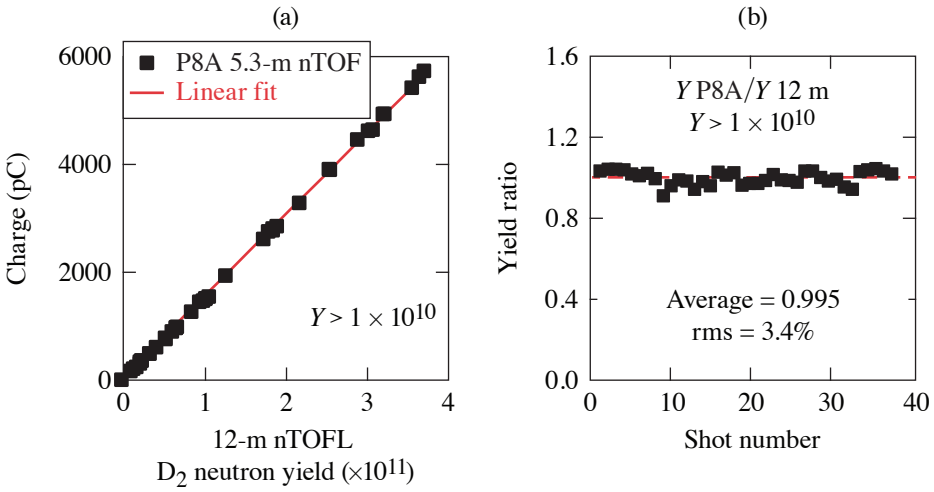

TC16083JR

Figure 1
(a) DD neutron calibration of P8A 5.3-m nTOF against 12-m nTOFL detector and (b) the ratio of DD yield measured by P8A 5.3-m nTOF and 12-m nTOFL detectors.

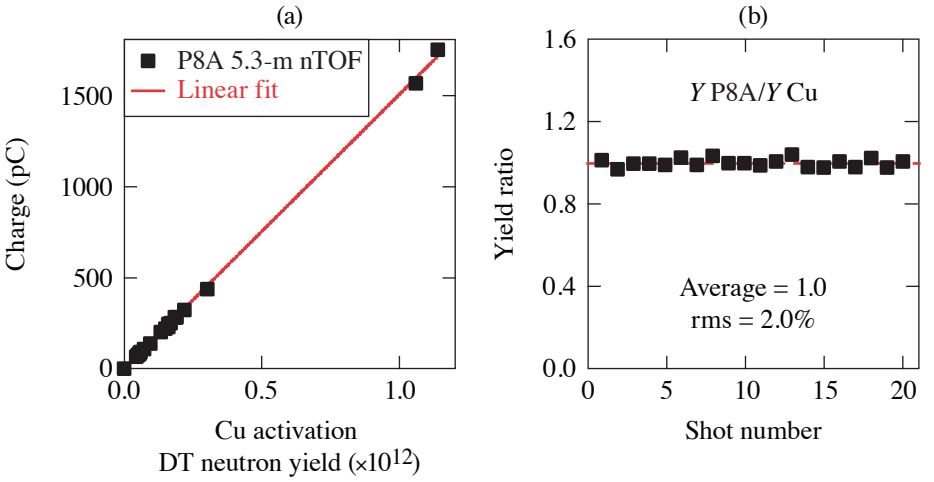

TC16085JR

Figure 2
(a) DT neutron calibration of P8A 5.3-m nTOF against copper activation and (b) the ratio of DT yield measured by P8A 5.3-m nTOF and copper activation.

A new nTOF detector was installed and calibrated on the OMEGA Laser System. This detector is now a standard OMEGA diagnostic for D–D yields above 1×10^{10} and DT yields from 5×10^{10} to 2×10^{12}.

This material is based upon work supported by the Department of Energy National Nuclear Security Administration under Award Number DE-NA0003856, the University of Rochester, and the New York State Energy Research and Development Authority. Sandia National Laboratories is a multimission laboratory managed and operated by National Technology & Engineering Solutions of Sandia, LLC, a wholly owned subsidiary of Honeywell International Inc., for the U.S. Department of Energy's National Nuclear Security Administration under contract DE-NA0003525. This paper describes objective technical results and analysis.

1. Photek Ltd., St. Leonards on Sea, East Sussex, TN38 9NS, United Kingdom, Accessed 9 September 2020, http://www.photek.com/.
2. M. A. Russotto and R. L. Kremens, Rev. Sci. Instrum. **61**, 3125 (1990).
3. V. Yu. Glebov *et al.*, Rev. Sci. Instrum. **75**, 3559 (2004).

A Knock-On Deuteron Imager for Measurements of Fuel and Hot-Spot Asymmetry in Direct-Drive Inertial Confinement Fusion Implosions

H. G. Rinderknecht,[1] P. V. Heuer,[1] J. Kunimune,[2] P. J. Adrian,[2] J. P. Knauer,[1] W. Theobald,[1] R. Fairbanks,[1] B. Brannon,[1] L. Ceurvorst,[1] V. Gopalaswamy,[1] C. A. Williams,[1] P. B. Radha,[1] S. P. Regan,[1] M. Gatu Johnson,[2] F. H. Séguin,[2] and J. A. Frenje[2]

[1]Laboratory for Laser Energetics, University of Rochester
[2]Plasma Science and Fusion Center, Massachusetts Institute of Technology

A knock-on deuteron imager (KoDI) has been implemented to measure the hot spot and fuel asymmetry of cryogenic inertial confinement fusion implosions on OMEGA. Energetic neutrons produced by D–T fusion elastically scatter ("knock-on") deuterons from the fuel layer with a probability that depends on ρR. Deuterons above 10 MeV are produced by near-forward scattering, and imaging them is equivalent to time-integrated neutron imaging of the hot spot. Deuterons below 6 MeV are produced by a combination of sidescattering and ranging in the fuel, and encode information about the spatial distribution of the dense fuel.

The KoDI instrument consists of a multi-penumbral aperture positioned 10 to 20 cm from the implosion using a ten-inch manipulator (TIM) and a detector pack at 350 cm from the implosion to record penumbral images with magnification of up to 35×. Range filters and the intrinsic properties of CR-39 (Ref. 1) are used to distinguish different charged-particle images by energy along the same line of sight. Image plates fielded behind the CR-39 record a 10-keV x-ray image using the same aperture.

Differential filtering is used to distinguish between high- and low-energy deuteron populations. The left half of the CR-39 is filtered by 135 μm tantalum, transmitting only deuterons initially above 10 MeV. The right half is filtered by 10 μm tantalum, transmitting deuterons initially above 2 MeV. The diameter of tracks is used to further discriminate the data into rough energy bins to interpret the images. While the exact diameter–energy relationship varies from sample to sample, the energy order and approximate energy range can be inferred. The analysis of the x-ray data is described in Ref. 2.

Penumbral imaging maximizes the statistics of the recorded signal. Each penumbral aperture is made by laser drilling a 200-μm-thick tantalum or 175-μm-thick tungsten substrate, producing a conical hole with an opening angle of 10°. Two effects cause the point-spread function (PSF) of the penumbral apertures to differ from the ideal knife edge: charged-particle scattering in the substrate and electrical charging of the array. Because of the high magnification of the camera, even a small amount of straggle is sufficient to produce a uniform background and the effect of scattering on the PSF blur is negligible. Electrical charging of the aperture array is more significant. A semi-analytic form of the charged-aperture PSF was derived using a numerically integrated electric field inside the array, $E(r)$:

$$\mathrm{PSF} = \left[\frac{\mathrm{d}r_\mathrm{i}'}{\mathrm{d}r_\mathrm{a}'}\right]^{-1}, r_\mathrm{i}' = r_\mathrm{a}' + \frac{e\Delta z}{4\pi\varepsilon_0}\left[\frac{Q}{K}\frac{D}{R_\mathrm{a}}\frac{M-1}{M^2}\right]E'\left(r_\mathrm{a}'\right), \tag{1}$$

where r_a and r_i are radial position in the aperture and image plane, R_a is the aperture radius, D the detector distance to target chamber center (TCC), Δz is the aperture thickness, M is the camera magnification, Q is the aperture charge density, K is the deuteron kinetic energy, and primes indicate normalized quantities $\left\{r_\mathrm{a}' = r_\mathrm{a}/R_\mathrm{a},\ r_\mathrm{i}' = r_\mathrm{i}/R_\mathrm{a}M,\ E' = E'/\left[Q/2\pi\varepsilon_0\right]\right\}$. The charged-aperture PSF is a family of curves that depends only on the value of the coefficient in square brackets, which we call V. [We select

$\Delta z = 200\ \mu$m and V has units of (coulomb/cm^2)/MeV.] Charging effects are negligible for values $V \lesssim 10^{-7}$, but become dominant for $V \gtrsim 3 \times 10^{-5}$. For accurate reconstructions using a charged aperture, the amount of charging must be known and the blurring caused by charging effects must not dominate the structure caused by the object. The PSF radius at 50% of maximum increases monotonically with the charging coefficient. The amount of charging from the data is inferred by comparing the projected radius of the deuteron aperture images with x-ray measurements of the camera magnification. Since V depends on particle energy, low-energy deuterons are more susceptible to the effects of charging than high-energy deuterons.

The images of the source are encoded in the recorded penumbral images and are recovered using the iterative reconstruction algorithm described by Gelfgat *et al.* in the limit of Poisson statistics.[3] We include a uniform background and begin with a uniform prior. Numerical testing shows that for N total tracks, the required number of iterations to converge grows as roughly $N^{0.33}$ for a fixed image size. The asymptotic reconstructions are overfit, concentrating numerical noise into high variations between neighboring pixels. To avoid overfitting, a condition for when to terminate the reconstruction is desirable and is under investigation.

The KoDI system was fielded on a series of direct-drive cryogenic implosions on OMEGA during 2021 and 2022. In the majority of the experiments, the diagnostic was fielded in TIM-1 with a magnification of 25 or 35. In one shot series (102560–102571), multiple KoDI instruments were fielded at different magnifications on each shot. Figure 1 shows the (a) deuteron and (b) x-ray data recorded on shot 102568. Analysis of the raw x-ray data indicated a magnification of 35.70±0.10. The deuteron data were analyzed to infer a charge-induced magnification increase of 5.4±0.3%. These values were used to calculate the point-spread function for reconstructing the data. A reconstruction of a high-energy deuteron image is shown in Fig. 1(c), and the corresponding reconstructed x-ray image in Fig. 1(d). The inferred shape and size of the hot spot is comparable between the x rays and deuterons. The 50% radius (P0) of the deuteron image was fit as 30 μm, with a significant mode-2 (P_2/P_0) of 30%. The axis of the mode-2 matches that seen in the reconstructed x-ray image. The camera was fielded in TIM-5, observing the implosion nearly perpendicularly to the stalk axis, and the observed mode-2 is elongated in the stalk direction.

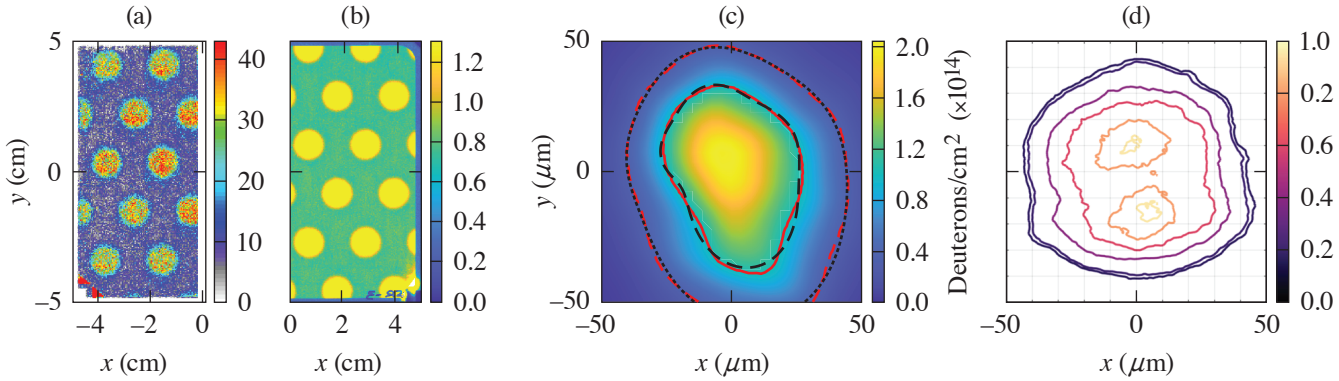

Figure 1
KoDI data recorded on OMEGA cryogenic implosion 102568. (a) High-energy deuteron image (>10 MeV, tracks per 400-μm square pixel); (b) 10-keV x-ray image (PSL per 100-μm square pixel); (c) reconstructed deuteron source with 50% and 17% intensity contours (red curves) and Legendre polynomial fits to $n = 4$ (black curves); and (d) reconstructed x-ray source.

Aperture charging was observed on the majority of the experiments and appears to show increased charging with aperture distance from TCC. The observed trend is not consistent with a prompt charging source that originates at TCC, which should fall off as R^2. The data are roughly consistent with a model in which the electromagnetic pulse (EMP) radiation produced by the laser–target interaction drives currents in the TIM body, for which farther distance from TCC allows a greater amount of time for the aperture to charge before being sampled by the deuterons.

While the charged-aperture PSF is, in principle, sufficient to interpret the diagnostic data, in practice, the reduction or elimination of aperture charging will significantly benefit the experiments by reducing analysis error and maximizing camera resolution,

and is necessary for low-energy deuteron images that are more severely distorted. Several approaches to controlling the aperture charging are being investigated, including replacing the front 30 cm of the diagnostic with a nonconductive material; fabricating the aperture from a nonconductive material such as silicon dioxide; and reducing the EMP source by changing the target mounting stalk.[4] These solutions will be tested in upcoming campaigns to assess their effects on the recorded data.

The data recorded by the KoDI diagnostic will enable detailed studies of the hot spot and assembled cold fuel on OMEGA. Comparisons of the high-energy deuteron and x-ray images will be used to infer the profiles of temperature and density to localize mix in the hot spot. Up to six lines of sight will be used to reconstruct the 3-D profiles of neutron emission and cold dense fuel. These data will provide unprecedented constraints on fuel assembly in direct-drive implosions, which will assist in the goals of reaching improved symmetry and hydro-equivalent ignition conditions on OMEGA.

This material is based upon work supported by the Department of Energy National Nuclear Security Administration under Award Number DE-NA0003856, the University of Rochester, and the New York State Energy Research and Development Authority.

1. N. Sinenian *et al.*, Rev. Sci. Instrum. **82**, 103303 (2011); **85**, 119901(E) (2014).
2. P. J. Adrian *et al.*, Rev. Sci. Instrum. **94**, 043548 (2021).
3. V. I. Gelfgat, E. L. Kosarev, and E. R. Podolyak, Comp. Phys. Commun. **74**, 335 (1993).
4. P. Bradford *et al.*, High Power Laser Sci. Eng. **6**, e21 (2018).

Design and Implementation of a Digital Optical Microscope for Measurement of Submicron Defects on Cryogenic DT Targets

D. Weiner, D. Bredesen, J. Bender, D. H. Edgell, C. Fella, V. N. Goncharov, D. W. Jacobs-Perkins, R. T. Janezic, M. W. Koch, S. F. B. Morse, S. P. Regan, S. Scarantino, M. J. Shoup III, M. D. Wittman, and J. Zou

Laboratory for Laser Energetics, University of Rochester

Submicron particles on the exterior surface of cryogenic deuterium–tritium (DT) target shells may contribute to hydrodynamic instability during target implosions that reduce predicted performance. Particles that originate from pre-existing shell defects or foreign material present within the target Fill/Transfer Station and are observed to exist on the surface after filling with a DT gas. Currently available imaging tools are limited to resolution of the order of 3 μm (Ref. 1). A digital optical microscope system has been developed that provides *in-situ* capability to image 0.5- to 1.0-μm features that are within a critical size range identified by physics considerations. The system design is described and initial results are presented.[2] Initial results indicate that the fill cycle process results in a statistically minor increase in defect count (+10%) and affected area (+4%), and that the pre-to-post fill particle distribution is unchanged.

The Fill/Transfer Station (FTS) is an existing system that houses a target during its fill cycle. Current target evaluation is done at a separate characterization station that is incompatible with cryogenic temperatures. Close examination of a target requires removal of the thermal shroud, which requires that the imaging system exist in a cryogenic environment. The target is held at a temperature of 40 to 50 K during observation.

A commercially available 40×, 0.60 N.A. long-working-distance microscope objective meets the 0.5-μm resolution goal. The projected 20-μm feature size implies that a camera sensor with pixel size less than 10 μm is required to avoid aliasing. A room-temperature test bed was designed and built to verify proof-of-concept using identical optics and illumination to enable comparison of pre- and post-fill images. A quasi-collimated illuminator was designed to reduce the formation hot spots in the target region that originate from LED source points and provide uniform irradiance in the target plane.

The prototype system is shown in Fig. 1. The mechanical design is comprised of three sections: an illuminator, the microscope holder and motion stage, and the charge-coupled–device camera. The microscope and illuminator assemblies are compatible with cryogenic temperatures while the camera is housed within a vacuum bubble to provide isolation from the cold environment. Heat sinks were included to provide for dissipation of thermal sources (LED and camera power supply). With the microscope located outside of the thermal shroud, the microscope translation stage is motorized with a range sufficient to move the objective to the target. Limit switches connected to the controls interface prevent inadvertent collisions between components. A prototype system was installed on the FTS.

The control system provides the ability to remotely power and adjust the LED illumination level, regulate the camera vacuum bubble temperature, and deliver motion control to the microscope and camera stages. To reduce the impact of target vibration and thermal load, the illumination is pulsed and synchronized with the camera's electronic shutter setting. The acquisition pulse width is adjusted to provide optimal integration time on the sensor. Interlocks prevent interference between the microscope, the FTS shroud puller, and the moving cryostat. A software interface is included for image acquisition, display, analysis, and storage. All major component controls are deliverable over an Ethernet connection.

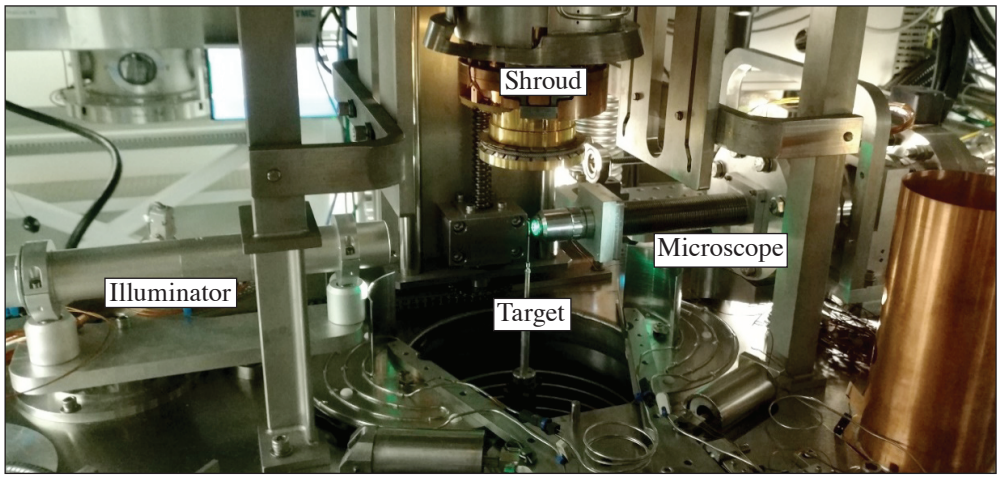

G13604JR

Figure 1
Installed FTS system showing key components.

A set of 12, 178 × 210-μm locations using pre-existing fiducial markers were established about the equator of the target shell, each of which was characterized under pre- and post-fill conditions. The warm temperature pre-fill and cryogenic post-fill optical systems used the same design with similar performance but separate systems. Each area was analyzed using all-in-focus (AIF)[3,4] and maximally stable extremal region (MSER)[5] image-processing techniques to detect and characterize micron-scale shell features. Images were pre-processed to normalize the bright-field background and optimize contrast. The AIF images were generated from a stack of eight to ten through-focus positions, which were then subject to an MSER algorithm for defect detection and statistical computation. A single target was used with a shell made from a glow-discharge polymer (GDP) process. Approximately 1% of the total shell area was analyzed and the results extrapolated. Figure 2 shows a side-by-side image comparison of one location for pre- and post-fill conditions.

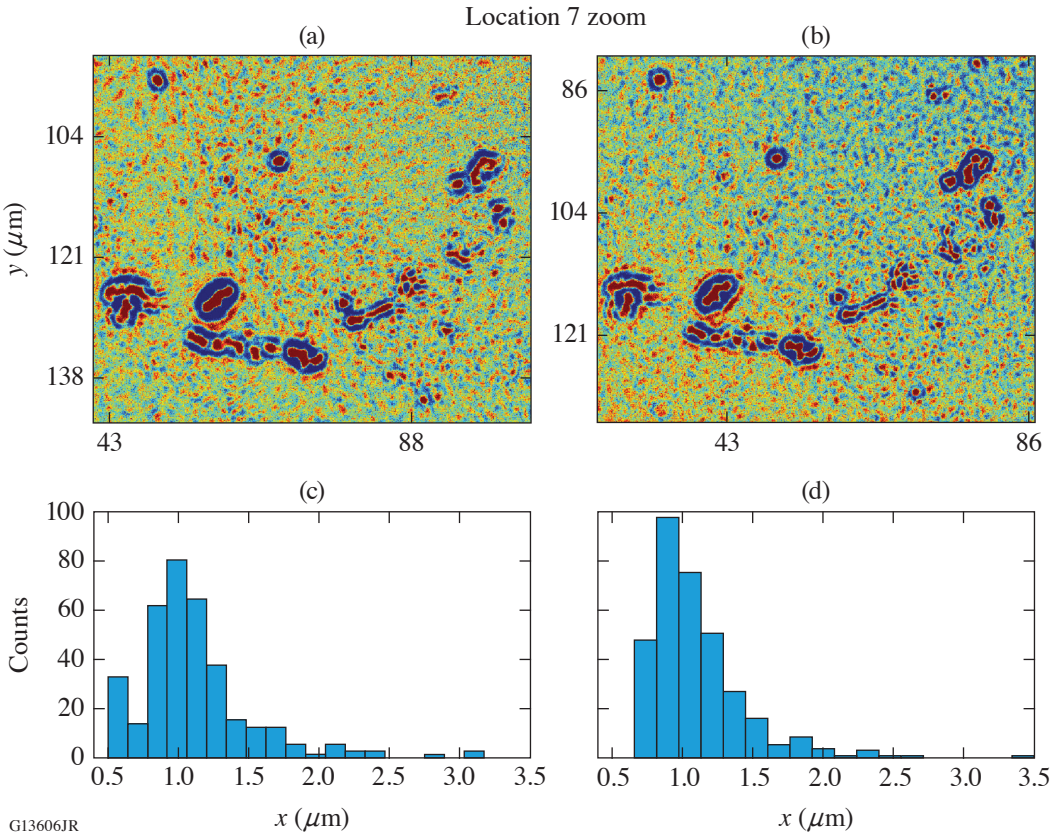

G13606JR

Figure 2
Image comparison for one of the 12 analyzed target areas.

The AIF/MSER techniques used found a 10% increase in feature counts and a 4% increase in feature area upon completion of the fill process (Fig. 3). While the plots suggest good agreement between the pre-fill and post-fill analysis, at present there is no assignment of error or degree of confidence assigned to the measurements.

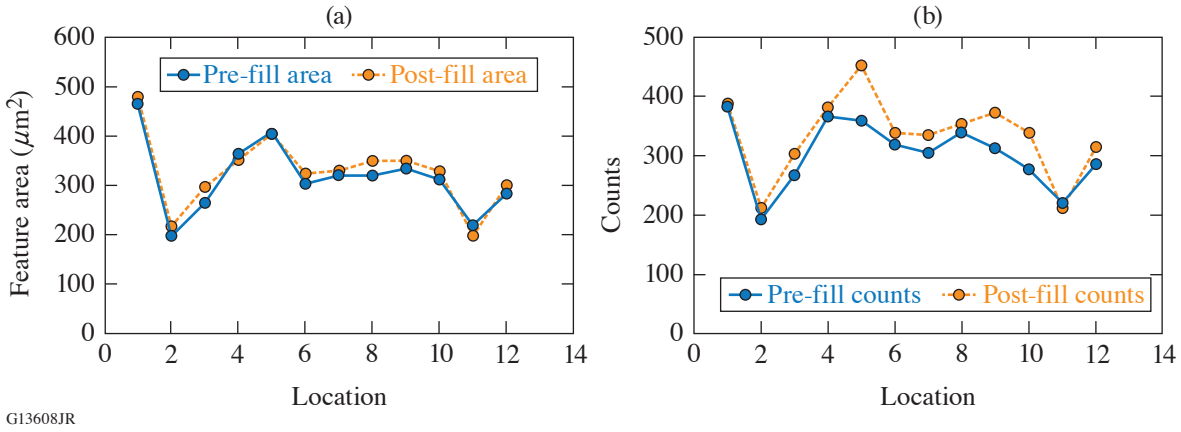

Figure 3
AIF/MSER analysis summary.

No new defects were identified between pre- and post-fill observations with the prototype system. Equivalent diameter size distribution for observed particles was between 0.5 to 2 μm (identified most significant for seeding hydrodynamic instabilities). Initial results indicate that the fill process does not significantly add to defect contribution, and that pre- and post-observation defect distributions are unchanged.

Future work is anticipated to include the testing of target shells made from materials other than GDP (e.g., polystyrene) containing fewer pre-existing defects and the collection of larger data sets to strengthen the statistical significance of results that are obtained. Periodic recharacterization of the platform using a surrogate target is also planned to monitor possible long time-scale system drift.

This material is based upon work supported by the Department of Energy National Nuclear Security Administration under Award Number DE-NA0003856, the University of Rochester, and the New York State Energy Research and Development Authority.

1. *LLE Review Quarterly Report* **104**, 169, Laboratory for Laser Energetics, University of Rochester, Rochester, NY, NTIS Order No. PB2006-108481 (2005).
2. D. R. Harding *et al.*, Matter Radiat. Extremes **3**, 312 (2018).
3. S. Pertuz *et al.*, IEEE Trans. Image Process. **22**, 1242 (2013).
4. F. Pérez Nava and J. P. Luke, in *2009 3DTV Conference: The True Vision - Capture, Transmission and Display of 3D Video* (IEEE, New York, 2009), pp. 1–4.
5. P. P. Ramya and J. Ajay, in *2019 1st International Conference on Innovations in Information and Communication Technology (ICIICT)* (IEEE, Chennai, India, 2019), pp. 1–4.

Tunable Picosecond AlGaN UV Photodiodes

S. F. Nwabunwanne and W. R. Donaldson

Laboratory for Laser Energetics and Department of Electrical and Computer Engineering, University of Rochester

Efficient and ultrafast UV photodetection is needed when characterizing high-temperature plasmas and ultrashort UV laser pulses. Semiconductor-based photodetectors (PD's) have not been widely used for these applications because of their reduced absorption depths in the UV spectrum, making streak cameras the dominant choice in the industry. A new category of photosensors built on $Al_xGa_{(1-x)}N$ (where x varies from 0 to 1) alloy provide tunable band gaps in the entire UV spectrum. Changing x varies from 0 to 1 and adjusts the band gap from 361 nm to 200 nm. Consequently, one can select the spectral window of interest for photosensing.

Laterally oriented AlGaN thin films were used to fabricate photodetectors with interdigitated electrodes.[1] These detectors recorded <30-ps response times, making them suitable for diagnosing ultrafast UV laser pulses and laser–plasma interactions.

This summary reports the outcomes of the spectral studies of detectors fabricated on different $Al_xGa_{(1-x)}N$ thin films where x is 0 to 0.3 (Ref. 1). Measured spectral responsivities are in the range of 0.43 A/W, which is comparable to other semiconductor-based detectors in the visible and infrared regions like silicon and InGaAs. High-quality semiconductors are critical for achieving these results, hence material characterization with x-ray diffraction is recommended prior to fabrication. The University of Rochester is in collaboration with Sydor Technologies to make these detectors available to the public. Some of the AlGaN PD's reported in Refs. 1 and 2, as well as newly fabricated GaN ($x = 0$) PD's with the same design parameters given in Ref. 1, were investigated for a comparison of their spectral selectivity profiles. The objective of this investigation was to determine the spectral responsivity and the ultrafast characteristics of our $Al_xGa_{(1-x)}N$ detectors with x ranging from 0 to 0.3

Figure 1 portrays the temporal response of a Au intrinsic $Al_{0.1}Ga_{0.9}N$ circular asymmetric (CA) device under study and a silicon reference PD at 260 nm under 20-V bias voltage. The voltage response of the AlGaN detector was 1.4 V with a 33-ps rise time

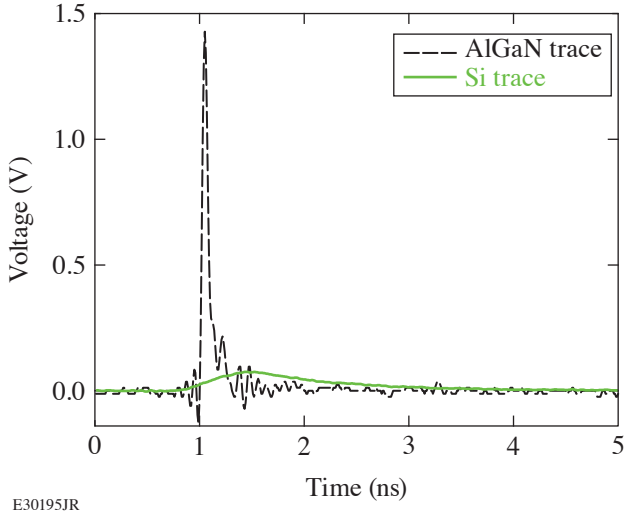

Figure 1
Au intrinsic $Al_{0.1}Ga_{0.9}N$ CA device response (black curve) under 20-V bias and Si reference detector (green curve) at 260 nm with rise times of 33 ps and 430 ps, and FWHM of 60 ps and 1.2 ns for AlGaN and Si PD's, respectively.

and a 60-ps full width half maximum. The pulse width of the device's temporal response increased from 26 ps (the resolution of the 12.5-GHz Tektronix oscilloscope) to 60 ps because of the delays introduced by the measurement system.[3]

The spectral responsivity of another AlGaN device that had 10% Al and rectangular asymmetric (RA) Pt (Ref. 1) metal contacts is depicted in Fig. 2. This detector's responsivity peaked at 315 nm with 0.43 A/W and a rapid cut off at 360 nm. The high responsivity supports the recorded external quantum efficiency of these photodiodes reported in Ref. 1. The responsivity dropped at shorter wavelengths because the absorption depth of photons within the AlGaN thin film reduced from 77 nm at 280 nm to 48 nm at 240 nm.

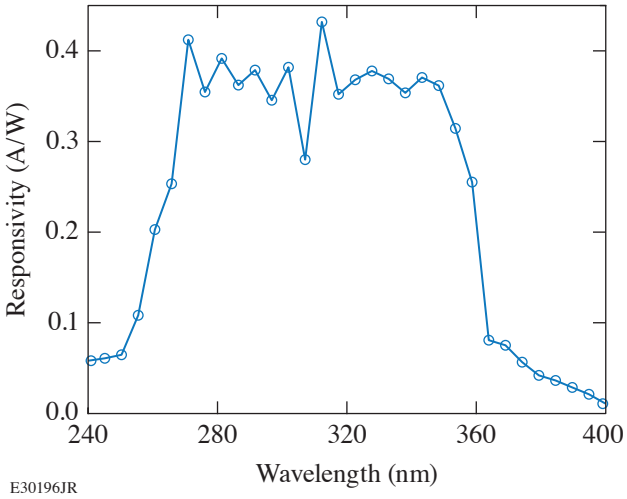

Figure 2
Pt intrinsic $Al_{0.1}Ga_{0.9}N$ RA device with spectral responsivity at 10-V bias voltage with peak responsivity of 0.43 A/W at 315 nm.

The spectral responsivity properties of another AlGaN UV PD that has 20% Al with CA Au metal is presented in Fig. 3. The data were measured under a 10-V bias voltage. This detector exhibited a maximum spectral responsivity of 0.033 A/W at 280 nm and a rapid cut off at 300 nm. The rising Al content implies that this diode will sense only deep UV wavelengths but a factor of 10 decrease in responsivity is recorded at 280 nm.

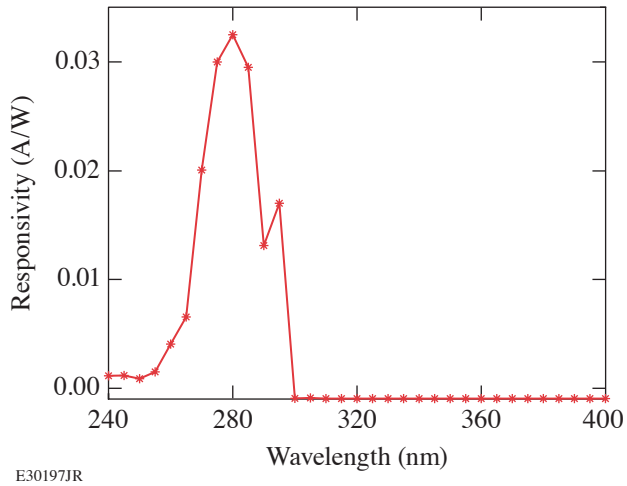

Figure 3
Au intrinsic $Al_{0.2}Ga_{0.8}N$ CA device with spectral responsivity at 10-V bias voltage with maximum responsivity of 0.033 A/W at 280 nm.

Summing up, the spectral responsivity of our AlGaN UV detectors in a metal–semiconductor–metal configuration was discussed. The results demonstrated that the applicability of AlGaN-based UV detectors in high-energy investigations of laser–plasma interactions, which have multiple sources of light in close proximity, require ultrafast and efficient UV photodetection. Finally,

it is necessary to carefully select the Al composition that meets the spectral window that needs to be sensed as this determines if the realized PD will meet the application requirements.

This material is based upon work supported by the Department of Energy National Nuclear Security Administration under Award Number DE-NA0003856, the University of Rochester, and the New York State Energy Research and Development Authority.

1. S. F. Nwabunwanne and W. R. Donaldson, IEEE J. Quantum Electron. **57**, 4000608 (2021).
2. S. Nwabunwanne and W. Donaldson, Proc. SPIE **12001**, 120010F (2022).
3. Y. Zhao and W. R. Donaldson, J. Mater. Res. **33**, 2627 (2018).

Measurement of Laser Absorption in Underdense Plasmas Using Near-Field Imaging of the Incident and Transmitted Beams

J. Katz,[1] D. Turnbull,[1] S. T. Ivancic,[1] A. L. Milder,[1] and D. H. Froula[1,2]

[1]Laboratory for Laser Energetics, University of Rochester
[2]Department of Physics and Astronomy, University of Rochester

Measurements of laser absorption in high-temperature, underdense plasmas produced at the Omega Laser Facility are made using two near-field imaging detectors that diagnose the spatial profile and energy of the port P9 beam before and after it transmits through the plasma. By comparing the signal ratios of these detectors for shots with and without plasma, absorption is measured without the need for absolute energy calibration of either detector. Complementary diagnostics monitor laser backscatter and spatially resolve key plasma parameters,[1] including ion and electron temperature and electron density, along the beam propagation length. Simultaneous measurements of the plasma conditions and total beam absorption provide means to experimentally validate physics models used to predict absorption in plasmas relevant to inertial confinement fusion.

The experimental platform, shown in Fig. 1, utilizes a set of 351-nm heater beams to ionize a 2-mm-diam, cylindrical column of neutral gas that is injected into target chamber center (TCC) using a gas-jet delivery system. The 527-nm P9 probe beam is then fired into the plasma. Experimental conditions can be varied by adjusting the 351-nm heater-beam energies and timings or by changing the gas type and initial neutral gas density. Total absorption in these high-temperature (>100-eV), millimeter-scale-length plasmas are often a few percent or less. As such, high-precision measurements of the input and transmitted beam energies are required. It is also important to confirm that any potential energy loss to the transmitted beam from mechanisms other than absorption remain energetically insignificant.

The input beam is sampled using a partial reflection from a full-aperture, 30-cm-diam uncoated-wedge pickoff located before the target chamber vacuum window and final-focus lens assembly. An uncoated, concave mirror focuses the reflected beam at *f*/10, allowing it to be recorded directly with a 13 × 13-mm sensor. The P9 transmitted-beam diagnostic (P9TBD)[2] characterizes the transmitted light by terminating the expanded beam on a semi-transparent diffuser and imaging the illuminated surface using a lens and charge-coupled–device (CCD) camera. The near-field image measures both the transmitted beam energy and the degree of any potential beam filamentation or whole beam refraction. The nominal diameter of the expanded beam at the diffuser plane is 28 cm. The 45-cm (*f*/4) acceptance aperture of the P9TBD allows energy of the beam to be measured even in the presence of moderate levels of beam refraction or filamentation.[3]

For an ideal detector, the total signal recorded on the CCD images is proportional to the amount of energy present at TCC. The proportionality constant, K, given in analog-to-digital units (ADU) per joule of photon energy, is influenced by a number of factors including the optical throughput between the sample point and TCC, the sensor quantum efficiency, the camera digitizer gain, and the throughput of any optical filtration used to adjust signal levels. It is difficult to accurately quantify all of these components individually. If the energy loss in the transmitted beam is limited to absorption alone, however, knowledge of the individual instrument sensitivities is not required to determine absorption since the measurement depends only on the ratio of the instrument sensitives K and the total signals.

$$\mathrm{ABS} = 1 - \frac{c_{\mathrm{Trans}}}{\underbrace{c_0}_{K}} \frac{\sum \mathrm{CCD}e^{-}_{\mathrm{Trans}}}{\sum \mathrm{CCD}e^{-}_{0}},$$

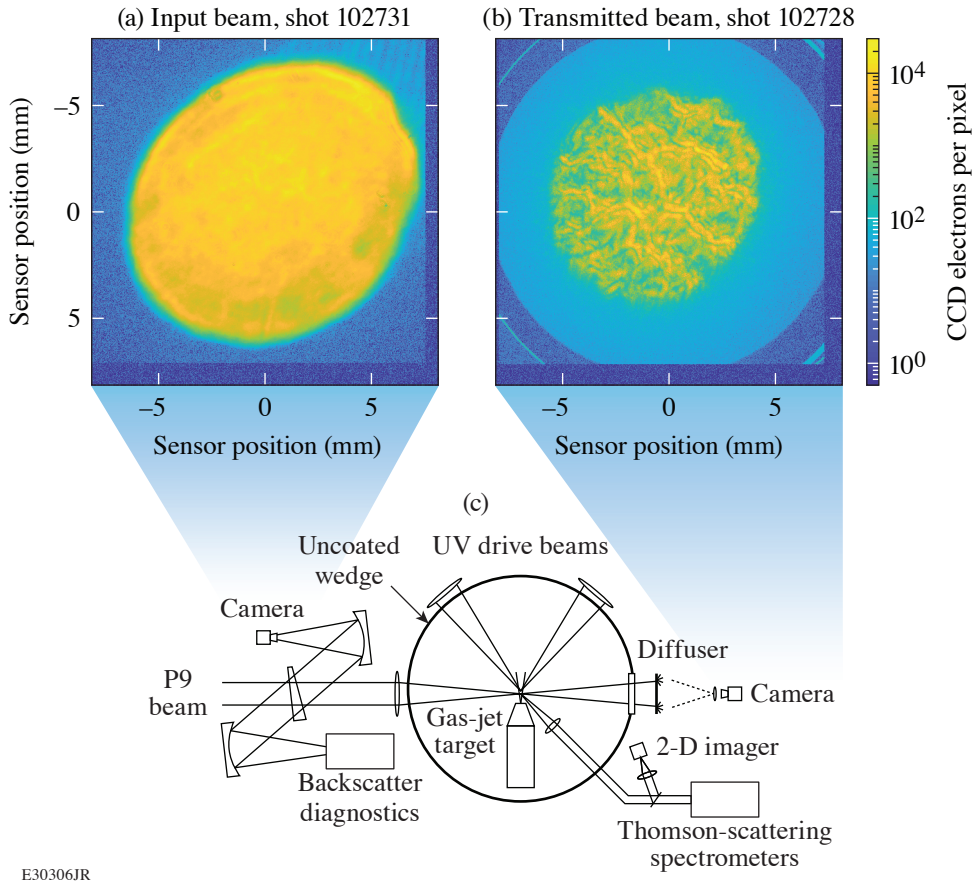

Figure 1
The amount of laser energy deposited in the plasma from a single beam is inferred by comparing input and output energies. Two CCD cameras measure the incident and transmitted beam spatial profiles and energies with high precision. Back and sidescatter diagnostics are used to verify that energy losses from laser–plasma instabilities are energetically insignificant.

where K is measured experimentally by taking a calibration shot with no plasma present. In this case, there is no absorption, $E_0 = E_{\text{Trans}}$, and K is given by the ratio of the input to transmitted signals. To the extent that c_0 and c_{Trans} remain stable over time, the accuracy of the absorption measurement is driven by the measurement precision of the two detectors. Two calibration shots are normally taken during a shot day to confirm the measurement stability and typically agree to within ±0.01%. Additionally, the measurement stability and precision of the two detectors was benchmarked using a full-aperture, Q-switched laser propagated along the P9 beamline through TCC. Synchronized images were recorded at 5-min intervals over a period of 8 h and the ratio of the detector sensitivities was measured. The measurement variation followed a normal distribution with a standard deviation of ±0.014% and showed no noticeable drifts as a function of time.

The amount of stray 2ω light from the other OMEGA drive beams that scatters into the P9 energy detectors is also measured. For these calibration shots, the plasma is heated by the drive beams but the P9 probe beam is turned off and the background level is measured directly. If a variety of beam energies are fielded during the shot day, the magnitude of the background subtraction is scaled by the total 2ω light present in the experiment, as measured by the harmonic energy diagnostic.[4] Baffling and optical filtration help limit the background signal levels to less than 0.05% of the primary signal.

Propagating the expected errors present in the calibrations and the statistical noise in the signal summations, the overall uncertainty of a typical absorption measurement is estimated to be ±0.07%. With these capabilities, the mechanics of inverse bremsstrahlung heating can be explored experimentally with exceptional quantitative detail.

This material is based upon work supported by the Department of Energy National Nuclear Security Administration under Award Number DE-NA0003856, the University of Rochester, and the New York State Energy Research and Development Authority.

1. J. Katz *et al.*, J. Instrum. **8**, C12009 (2013).
2. J. Katz *et al.*, Rev. Sci. Instrum. **92**, 033526 (2021).
3. D. Turnbull *et al.*, Phys. Rev. Lett. **129**, 025001 (2022).
4. *LLE Review Quarterly Report* **63**, 110, Laboratory for Laser Energetics, Rochester, NY, NTIS Order No. DE96000767 (1995).

Design of the High-Yield, Time-Gated X-Ray Hot-Spot Imager for OMEGA

S. T. Ivancic,[1] W. Theobald,[1] K. Churnetski,[1] M. Michalko,[1] D. Willistein,[1] W. A. Bittle,[1] S. P. Regan,[1] A. Carpenter,[2] C. Trosseille,[2] J. D. Kilkenny,[3] A. Raymond,[3] J. D. Hares,[4] A. K. L. Dymoke Bradshaw,[4] G. Rochau,[5] and D. Garand[6]

[1]Laboratory for Laser Energetics, University of Rochester
[2]Lawrence Livermore National Laboratory
[3]General Atomics
[4]Kentech Instruments Ltd., UK
[5]Sandia National Laboratories
[6]Sydor Technologies

Low-mode 3-D nonuniformities of the compressed core in inertial confinement fusion (ICF) implosions are important to diagnose because they represent inefficiency in the conversion of kinetic to internal energy of the core.[1] X-ray projection to infer 3-D shape is incisive for understanding drive nonuniformities and their potential mitigations.[2] Demonstration of using time-integrated x-ray imaging has been developed,[3,4] which is transferrable to time-resolved analysis with a suite of time-synchronized detectors with sufficient signal. Drift-tube imagers[5,6] coupled to high-speed hybrid complementary metal-oxide semiconductor (hCMOS) detectors[7] have a number of advantages over framing cameras[8] especially for being fieldable in a harsh neutron environment such as those found near the target chamber during high-yield implosions. Radiation-hardened electronic readout is essential to provide real-time data. A third, time-gated x-ray line of sight is proposed for OMEGA to provide an additional view to allow for time-resolved 3-D tomographic reconstruction of the hot-spot shape. The simultaneous operation of this new imager with the existing time-gated x-ray imaging lines of sight on OMEGA[9,10] will enable a time-resolved reconstruction of the low-mode shape of the ICF hot spot.

The x-ray hot-spot imager consists of three distinct subassemblies illustrated schematically in Fig. 1: A 22.5× magnification pinhole-array imager provides a multitude of images at an intermediate plane located outside of the OMEGA tank wall on a large-format photocathode. The x rays are converted to photoelectrons, which are imaged by a demagnifying, dilation drift tube that reduces the photoelectron image by 2× on a detector plane while providing temporal magnification of 100 to 350×. The demagnification serves two purposes, first it allows the imager to operate at a larger magnification that serves to lower the current at the photocathode. Demagnification is required in order to form the image to a suitable size to be detected by available solid-state detectors. In this case the photoelectron images are recorded by two side-by-side hCMOS[10] sensors, which are capable of recording eight sequential frames with an adjustable integration time in the range of 1 to 10 ns. The temporal magnification maps eight 20-ps sequential frames onto the hCMOS with a varying duration from 2 to 7 ns. This magnification allows the entire x-ray emission history of the hot spot to be captured.

The photoelectrons are constrained by a homogeneous axial magnetic field to move helical orbits along the axis of the drift tube, providing an upright photoelectron image onto the hCMOS detector. The design of the tube is segmented with the magnetic-field strength increasing in the latter two segments to provide the 2:1 demagnification of the drifting photoelectron signal as it traverses the tube. Simulations using magnetostatic modeling using the field solver *COMSOL* have been performed to measure the effect of segmentation of the solenoidal field into four separate tube parts working together. The overall effect is negligible relative to the sizes of the imager point-spread function and blurring caused by the drift tube.

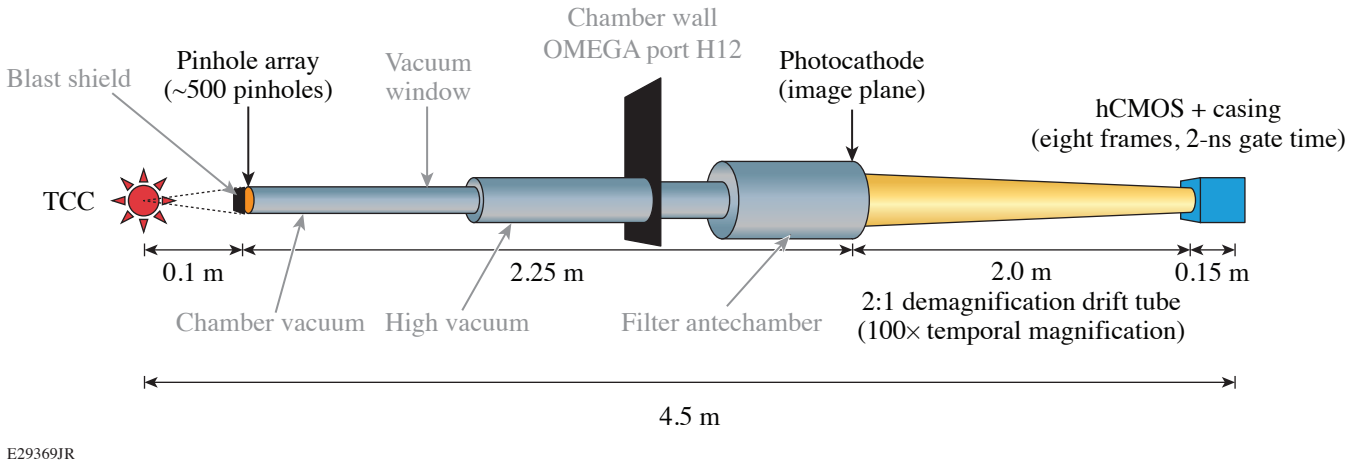

Figure 1
Schematic of the overall x-ray imaging system. A pinhole array is situated 100 mm from the target chamber center (TCC). The x-ray images pass through a beryllium vacuum window located in a re-entrant tube inside the tank that separates the tritium-contaminated tank vacuum from a separate clean vacuum volume that includes the instrument inclusive of the drift tube. The x-ray image emerges from the target chamber out of OMEGA port H12 to an intermediate image plane located 2.25 m from the pinhole array. An access hatch forward of the image plane allows for x-ray filters to be introduced over some or all of the x-ray images. The x-ray imager casts >500 images onto a 50-mm × 50-mm intermediate image plane.

This material is based upon work supported by the Department of Energy National Nuclear Security Administration under Award Number DE-NA0003856, the University of Rochester, and the New York State Energy Research and Development Authority.

1. K. M. Woo *et al.*, Phys. Plasmas **25**, 102710 (2018).
2. O. M. Mannion *et al.*, Phys. Plasmas **28**, 042701 (2021).
3. K. Churnetski *et al.*, Rev. Sci. Instrum. **93**, 093530 (2022).
4. S. M. Glenn *et al.*,, Rev. Sci. Instrum. **83**, 10E519 (2012).
5. T. J. Hilsabeck *et al.*, Rev. Sci. Instrum. **81**, 10E317 (2010).
6. K. Engelhorn *et al.*, Rev. Sci. Instrum. **89**, 10G123 (2018).
7. L. Claus *et al.*, Proc. SPIE **10390**, 103900A (2017).
8. D. K. Bradley *et al.*, Rev. Sci. Instrum. **66**, 716 (1995).
9. W. Theobald *et al.*, Rev. Sci. Instrum. **89**, 10G117 (2018).
10. F. J. Marshall *et al.*, Rev. Sci. Instrum. **88**, 093702 (2017).

High-Resolution Mapping of Phase-Matching Conditions in Second-Order Nonlinear Crystals

C. Dorrer, I. A. Begishev, S.-W. Bahk, and J. Bromage

Laboratory for Laser Energetics, University of Rochester

Nonlinear crystals are widely used for frequency conversion of lasers and optical parametric amplification. Phase matching between the interacting waves is required for efficient operation.[1] This can generally be achieved by temperature or angle tuning, which both allow precise control the optical index. Such global tuning is sufficient when the interacting beams and the crystal have spatially uniform properties. This is a reasonable assumption for relatively small nonlinear crystals. However, the local crystals properties are impacted by environmental stability during growth, stress within the boule, and impurities in the growth solution. These issues are particularly important for the large-aperture ($\sim 40 \times 40$-cm^2) KDP and partially deuterated KDP (DKDP) that are required to support doubling and tripling of inertial confinement fusion laser systems.[2,3] Variations in axis angle θ and deuteration level X can decrease the frequency-conversion efficiency and uniformity. Large-aperture deuterated KDP crystals will be required for optical parametric chirped-pulse–amplification systems delivering ultrashort optical pulses with peak power well beyond 1 PW (Ref. 4).

While x-ray techniques, optical interferometry, and spectroscopy can be used to spatially resolve the physical characteristics of nonlinear crystals, mapping the local phase-matching conditions is a more-direct approach to performance quantification for an actual laser system. This work demonstrates the high-resolution characterization of local phase-matching conditions for second-harmonic generation of a beam at 1053 nm in several laser crystals, including partially deuterated KDP crystals used for broadband optical parametric amplification of pulses at 920 nm by a pump pulse at 526.5 nm (Ref. 5).

A test bed capable of characterizing crystals over apertures as large as 50×50 mm^2 has been developed [Fig. 1(a)]. A Nd:YLF regenerative amplifier seeded by a fiber front end delivers 1053-nm (λ_1) 350-ps pulses collimated to an ~1-mm diameter. The crystal under test (length L) is mounted on two translation stages that provide transverse scanning in front of the static laser beam. The phase-mismatch $\Delta k_{SHG}L$ for second-harmonic generation (SHG) is proportional to the normalized energy variation $S(x,y) = [\eta(x,y)/(1/2)]-1$, where η is measured at 526.5 nm (λ_2) for the crystal angularly detuned from ideal phase matching [(θ_+) and (θ_-) in Fig. 1(b)]. The nonideal translation stages induce small position-dependent angular rotations of the crystal that can impact phase matching. To alleviate this, the 1053-nm beam is stabilized by a piezo-actuated mirror using the feedback signal from a four-quadrant photodetector on which the beam reflected by the crystal's input face is incident.

As an example of application, the normalized energy variation S is shown in Fig. 2 for a crystal with a deuteration level equal to 98%. For the first two measurements, the input face is the same [labeled as (A) on the figure], whereas the input face is the opposite face for the third measurement [labeled as (B) on the figure]. This crystal has variations in normalized energy up to 25%. Anticorrelated variations of S are obtained when operating at θ_- and θ_+ [Figs. 2(a) and 2(b)]. The high-frequency variations, e.g., in the upper-right corner on Fig. 2(a), are not measurement artifacts. They consistently correspond to a sign change between Figs. 2(a) and 2(b), indicating that they are caused by a local change in phase matching instead of another effect such as low local transmission. This is confirmed by the measured energy variations after a 180° rotation along the vertical axis [Fig. 2(c)]. The low-frequency variations in S are symmetric along the x axis for the two crystal orientations differing by the 180° crystal rotation [Figs. 2(a) and 2(c)]. This indicates that they are caused by bulk variations and do not depend on the propagation direction within the crystal. The observed 25% variations in S are consistent with 20-μrad angular variations and 0.025% deuteration variations.

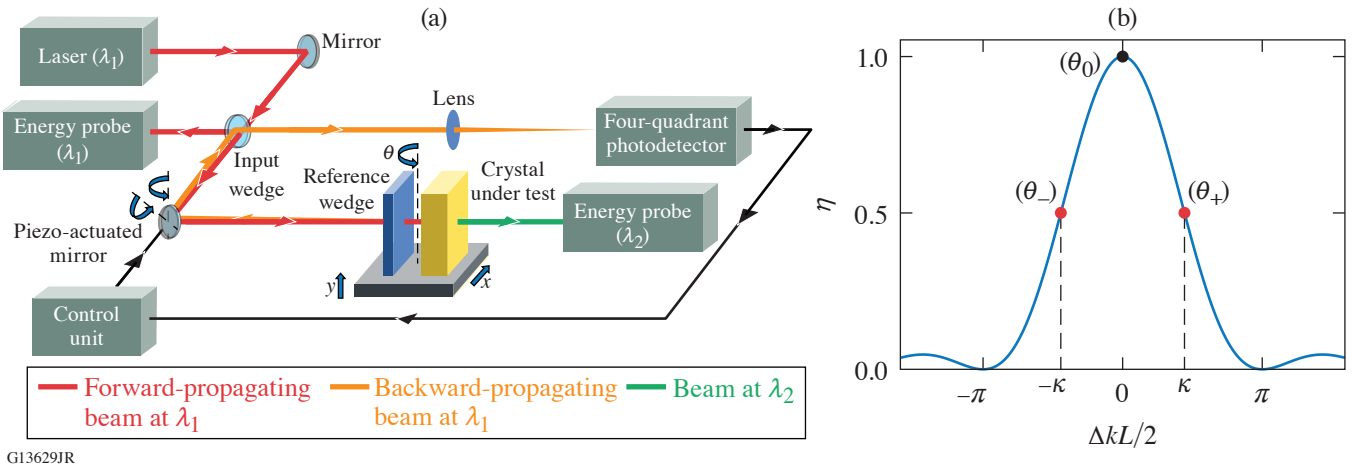

Figure 1
(a) Setup for spatially resolved measurement of the SHG energy, indicating the forward-propagating beam at λ_1 (red line), the backward-propagating beam at λ_1 (orange line), and the beam at λ_2 (green line). (b) Relative SHG efficiency η as a function of the phase mismatch ΔkL.

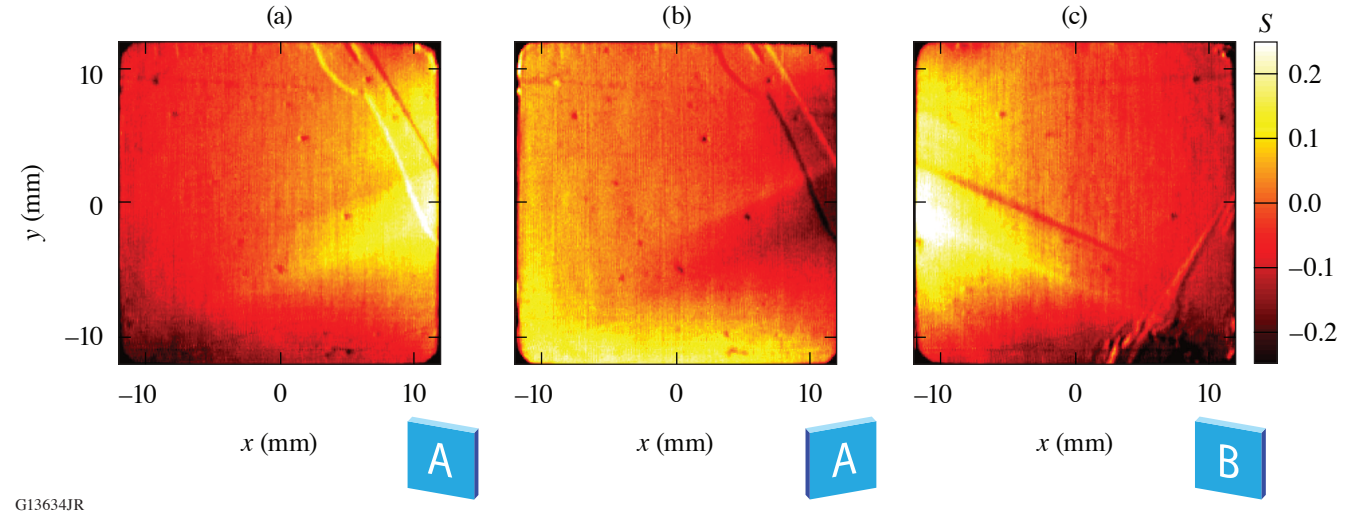

Figure 2
Normalized energy variation S for a crystal with a deuteration level equal to 98%. (a) and (b) correspond to characterization with the same face (A) at the input, and different phase-matching angles θ_- and θ_+, respectively. (c) corresponds to a 180° rotation of the crystal, i.e., characterization with the other face (B) at the input, and phase matching angle θ_-.

The high-frequency variations in S observed in the upper right corner of Fig. 2(a) are, however, not observed in the upper left corner of Fig. 2(c), indicating that these variations are caused by disruptions in phase matching occurring at or close to the input surface. Analytical derivations and experimental results obtained on other crystals confirm that surface variations, such as those introduced by irregularities in sol-gel antireflection coatings, can impact the phase-matching conditions.

A novel approach to the characterization of transverse variations in phase-matching conditions in nonlinear crystals has been demonstrated. SHG in the detuned crystal under test unambiguously converts the local phase mismatch onto energy at the upconverted frequency. Transverse scanning of the crystal combined with beam stabilization maps out phase-matching variations over an aperture only limited by the scanning range of the translation stages. The characterization of partially deuterated

KDP crystals with submillimeter resolution over a 50×50-mm^2 aperture has revealed the impact of spatially nonuniform crystal properties and high-frequency surface variations due to coating imperfections.

The authors thank A. Bolognesi, M. Barczys, T. McKean, and M. Spilatro for experimental assistance with the 1053-nm source. This material is based upon work supported by the Department of Energy National Nuclear Security Administration under Award Number DE-NA0003856, the University of Rochester, and the New York State Energy Research and Development Authority.

1. R. Boyd, *Nonlinear Optics*, 3rd ed. (Academic Press, Amsterdam, 2008), pp. 217–221.
2. J. J. De Yoreo, A. K. Burnham, and P. K. Whitman, Int. Mater. Rev. **47**, 113 (2002).
3. J. M. Auerbach *et al.*, Appl. Opt. **40**, 1404 (2001).
4. C. N. Danson *et al.*, High Power Laser Sci. Eng. **7**, e54 (2019).
5. C. Dorrer *et al.*, Opt. Mater. Express **12**, 3679 (2022).

Utilizing the MTW-OPAL Idler to Seed a Raman Plasma Amplifier

S. Bucht, R. G. Roides, B. Webb, D. Haberberger, C. Feng, D. H. Froula, and J. Bromage

Laboratory for Laser Energetics, University of Rochester

A Raman plasma amplifier (RPA) promises to overcome the damage limitations of chirped-pulse–amplification (CPA)[1] compression gratings by using a "damage-free" plasma to transfer energy from a multipicosecond high-energy pulse to a longer-wavelength femtosecond seed pulse.[2] This technology promises to achieve focused intensities exceeding 10^{23} W/cm^2 if pumped with the output of an Nd:glass-based CPA system laser[3] but requires a 1100- to 1250-nm seed pulse. Simulations show that to achieve an efficient amplifier, a high-intensity (10^{15} W/cm^2), sub-200-fs duration seed pulse is required.[4,5]

One technique for creating such a laser is by using the idler of an optical parametric chirped-pulse–amplification (OPCPA) system.[6] OPCPA systems produce two broadband pulses: a signal, which is seeded, and an idler, which has a wavelength that is red shifted. The Multi-Terawatt optical parametric amplifier line (MTW-OPAL) Laser System,[7,8] which produces 7-J, 20-fs pulses at 910 nm, consists of an ultrabroadband front end (UFE), a cylindrical Offner stretcher (COS), a power amplifier (N4), and a final DKDP amplifier (N5) as shown in Fig. 1(b). The idler that exits the N4 power amplifier has a bandwidth that ranges from 1100 to 1500 nm and 70 mJ of energy; if compressed and focused it would provide an ideal laser to seed an efficient RPA.

Using this idler requires overcoming two disadvantages that are a result of phase matching and energy conservation. First, phase matching in N4 produces an idler that is angularly dispersed, which hampers pulse focusing and compression.[9] Second, energy conservation inverts the spectral phase of the idler relative to the signal,[10] significantly changing the typical stretch–amplify–compress process of CPA.[1] Here we address both the phase reversal and angular dispersion of the MTW-OPAL idler with the addition of several optical subsystems to achieve 100-GW pulses at 1170 nm with 120-fs durations.

For ease of switching between the conventional MTW-OPAL configuration [Fig. 1(b)] and an idler OPAL configuration [Fig. 1(a)], many of the subsystems were left unchanged between the two modes of operation. No changes were made to the UFE or the N4 pump laser. The differences include switching from the COS to an alternate grism stretcher (GrS), operating at a reduced bandwidth, and bypassing the final amplifier (N5). This GrS accounts for the inversion of the idler spectral phase and allows for a standard grating compressor to be used to compress the idler (IGC). Angular dispersion was compensated with an angular dispersion compensator (ADC) prior to compression.

The design of the GrS is the result of compromise between a full compression of the pulse and optic manufacturing limitations.[11] Each grism is made from a 45°, N-SF57 prism mounted 1 mm away from a 1480-lp/mm gold grating. This design fully compensates for the two lowest orders of spectral phase (group-delay dispersion and third-order dispersion) but has some residual fourth-order dispersion. The stretcher also reduces bandwidth of OPAL to wavelengths that correspond those of interest for an RPA and a roof mirror double passes the pulse to a duration of 1 ns.

The idler exiting N4 is imaged with a 3× achromatic image relay onto two custom prisms to reduce angular dispersion from 123 μrad/nm to <0.5 μrad/nm. The idler is then compressed with a pair of parallel 1285-lp/mm gratings (PGL) and a roof mirror. Slant distance and input angle are selected to maximize peak power as measured with a custom IR-SPIDER (APE).[12] The compressed pulse was measured to have a full-width-half-maximum (FWHM) pulse duration of 120±10 fs (Fig. 2).

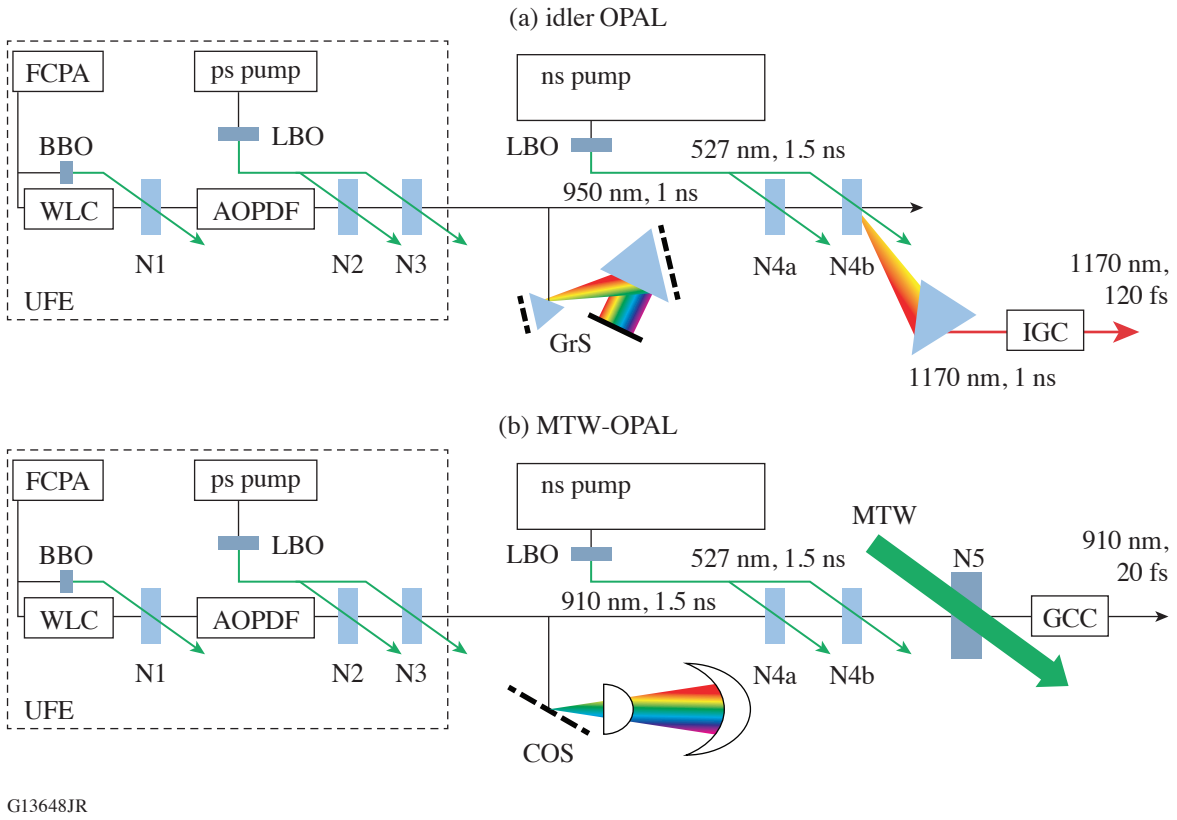

Figure 1

(a) A schematic of the idler OPAL and (b) standard MTW-OPAL configurations shows that they share many components including the UFE, the pre- and power amplifiers (N4a and N4b), and a nanosecond pump laser. (a) Systems added to operate the OPAL idler include an alternate grism stretcher (GrS), ADC, and an IGC. (b) The components of MTW-OPAL that are unused are the final amplifier, which is pumped by the MTW laser (N5), a COS, and grating compressor chamber (GCC). FCPA: fiber chirped pulse amplifier; WLC: white-light continuum; AOPDF: acoustic-optic-programable dispersive filter.

The focused and compressed idler had an average peak intensity of 5×10^{15} W/cm^2, which is about an order of magnitude lower than the transform-limited and diffraction-limited (TL-DL) intensity. The diffraction- and transform-limited intensity is based on the measured near-field beam profile and spectrum (row 1 in Table I). Reduction of this peak intensity is calculated from a subset of spatiotemporal effects: linear angular dispersion (AD), residual spectral phase, and monochromatic wavefront. Residual spectral phase was measured with the IR-SPIDER described above, while monochromatic wavefront was measured with a focal-spot diagnostic. This diagnostic was also used to measure residual angular dispersion by blocking all but two wavelengths in the GrS. How each of these spatiotemporal effects individually impact the achievable peak intensity is calculated in rows 2–4 in Table I. In the fifth row of Table I, all three spatiotemporal effects are applied.

Table I: Contributions to peak intensity.

	FWHM Pulse duration	Spot radii (μm)	AD$_x$,AD$_y$ (μrad/nm)	Intensity (W/cm^2)
TL-DL	50.2	19.6	0,0	56×10^{15}
Spectral phase	120	–		$14.1 \pm 0.8 \times 10^{15}$
Monochromatic wavefront	–	21.5 to 70		$18 \pm 3.7 \times 10^{15}$
Linear angular dispersion	–	–	<0.5, 0.5	35 to 56×10^{15}
Combined	120	21.5 to 70	<0.5, 0.5	$4.7 \pm 1 \times 10^{15}$

TL-DL: transform-limited; AD: angular dispersion

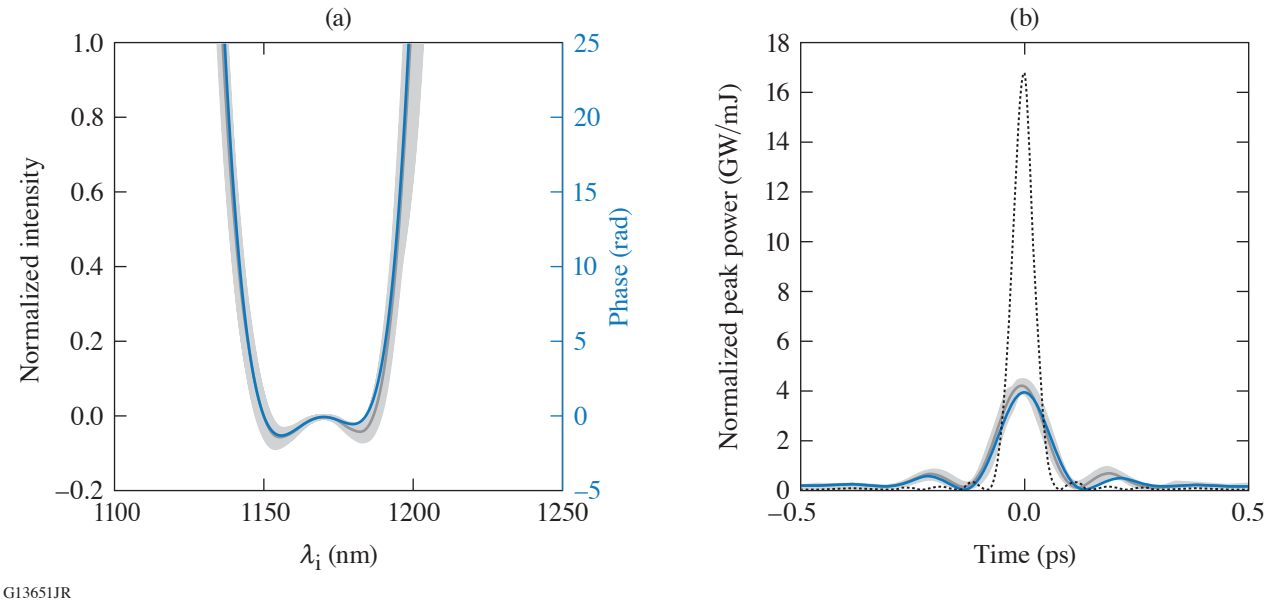

Figure 2
(a) The idler phase is measured over 100 shots by the IR-SPIDER and is denoted by the shaded area. The average phase and spectrum are shown by the solid gray and dotted curves, respectively, and closely matches the expected phase (blue curve). (b) The measured peak power is 4× lower than transform limited (black dotted curve), but matches the temporal pulse predicted by the design of the grism stretcher/grating compressor pair.

In conclusion, the compression of the idler to 100-GW peak powers from an existing OPCPA system has been demonstrated. While operating at a reduced peak intensity from the transform and diffraction limit, the idler from high-peak-power OPCPA systems achieves 100-GW pulses and provides a unique opportunity to further study the limits of laser technology.

This material is based upon the work supported by the Department of Energy Office of Science under Award No. DE-SC0016253, the Department of Energy National Nuclear Security Administration under Award No. DE-NA0003856, the University of Rochester, and the New York State Energy Research and Development Authority.

1. D. Strickland and G. Mourou, Opt. Commun. **56**, 219 (1985).
2. V. M. Malkin, G. Shvets, and N. J. Fisch, Phys. Rev. Lett. **82**, 4448 (1999).
3. J. H. Kelly *et al.*, J. Phys. IV France **133**, 75 (2006).
4. J. D. Sadler, "Optimisation and Applications of Raman Plasma Amplifiers," Ph.D. thesis, University of Oxford, 2017.
5. D. Haberberger *et al.*, Phys. Plasmas **28**, 062311 (2021).
6. A. Dubietis, G. Jonusauskas, and A. Piskarskas, Opt. Commun. **88**, 437 (1992).
7. J. Bromage *et al.*, High Power Laser Sci. Eng. **7**, e4 (2019).
8. J. Bromage *et al.*, High Power Laser Sci. Eng. **9**, e63 (2021).
9. T. Wilhelm, J. Piel, and E. Riedle, Opt. Lett. **22**, 1494 (1997).
10. I. N. Ross *et al.*, J. Opt. Soc. Am. B **19**, 2945 (2002).
11. S. Bucht *et al.*, J. Opt. Soc. Am. B **36**, 2325 (2019).
12. "APE Angewandte Physik & Elektronik GmbH," Ultrafast Laser Diagnostics & Tuneable Laser Solutions, Berlin, Germany.

Impact of Raman Scattering on Temporal Reflection from a Short Soliton

J. Zhang,[1] W. R. Donaldson,[2] and G. P. Agrawal[1]

[1]The Institute of Optics, University of Rochester
[2]Laborotary for Laser Energetics, University of Rochester

An optical pulse can be reflected at a temporal boundary across which the refractive index changes with time.[1] The reflected pulse is frequency shifted by an amount set by the law of momentum conservation. While a temporal boundary where the refractive index changes everywhere at the same time is hard to create in practice, reflection can also happen at a moving boundary. Such a boundary can be created through the optical Kerr effect by injecting an intense pump pulse into a dispersive nonlinear medium. This configuration has been studied in optical fibers when a weak pulse collides with an optical soliton.[2–4]

When a femtosecond soliton is formed inside an optical fiber, intrapulse Raman scattering between its different spectral components leads to a continuous red shift that decelerates the soliton as it propagates. This work considers the situation where a weak pulse reflects from such a decelerating soliton. It is shown that the reflected pulse can be much shorter than the input pulse, involving a new type of temporal focusing. The effect is explained using space–time duality and derive an approximate transformation law for Gaussian-shape input pulses.

Using the generalized nonlinear Schrödinger equation, the temporal reflection of a probe pulse from a soliton (called the pump pulse) is numerically simulated. Results are shown in Fig. 1 for a realistic set of parameters for silica fibers. In the time domain,

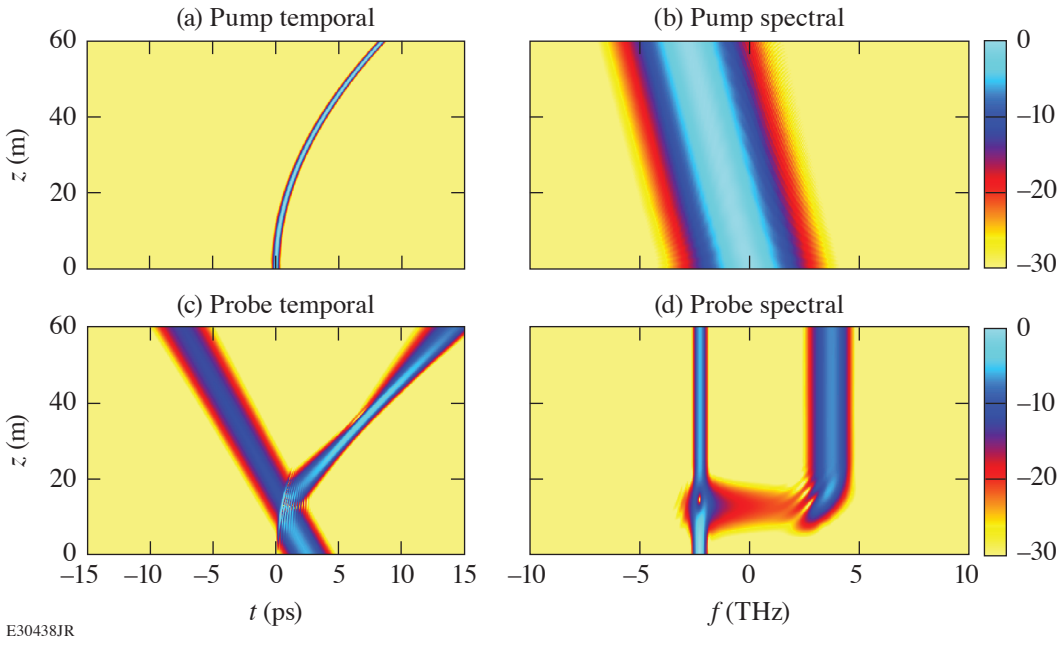

Figure 1
Simulation of temporal reflection of a probe pulse on a pump soliton. The pump soliton continuously red shifts because of Raman scattering.

the trajectory of the soliton has a parabolic shape because of its Raman-induced deceleration. When the probe pulse hits the pump pulse, it splits into a reflected pulse and a transmitted pulse.

The reflected pulse undergoes a frequency shift and its spectrum becomes broader than the incident spectrum. The reflected pulse also becomes narrower before it broadens again. This is an example of temporal focusing induced by the decelerating soliton. This effect can be explained using the concept of space–time duality.[5] The decelerating soliton forms a temporal boundary with a parabolic trajectory. A probe pulse reflected from this boundary is analogous to an optical beam being reflected by a parabolic-shaped mirror. It has been found that temporal focusing is more significant for longer incident pulses.

An approximate analytic theory has been developed that describes how the spectrum of an incident Gaussian pulse is modified when the pulse is reflected by a decelerating soliton. Figure 2 compares the analytical prediction with the numerical results. Both the reflected pulse spectrum and the rms pulse width of the reflected pulse agree well with the numerical simulations. The analytical approximation can be used to understand the temporal focusing effect.

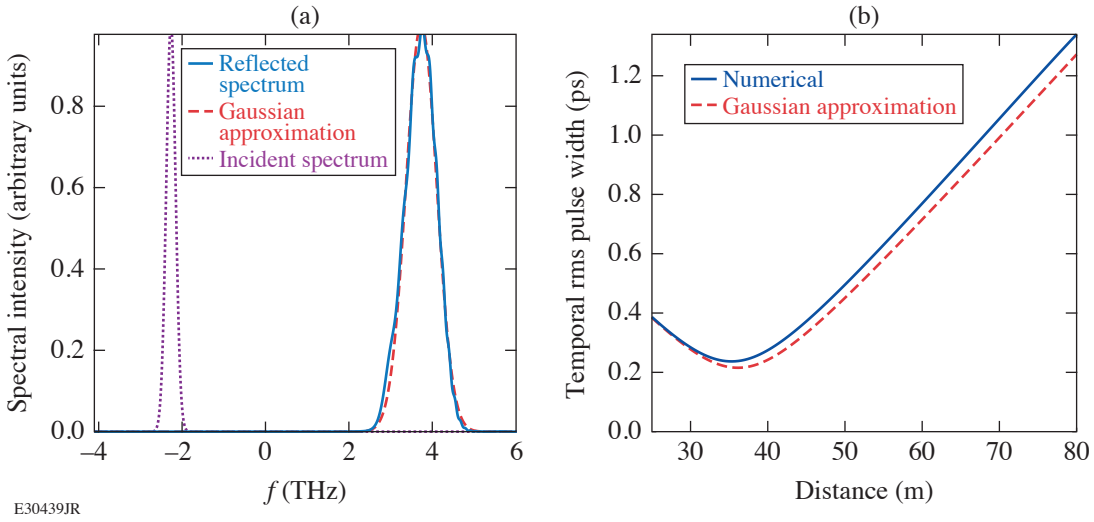

Figure 2
Comparison of analytical formula with numerical result. (a) Reflected pulse spectrum; (b) rms pulse width of a reflected pulse as it propagates.

This work is supported by National Science Foundation (ECCS-1933328). This material is based upon work supported by the Department of Energy National Nuclear Security Administration under Award Number DE-NA0003856, the University of Rochester, and the New York State Energy Research and Development Authority.

1. B. W. Plansinis, W. R. Donaldson, and G. P. Agrawal, Phys. Rev. Lett. **115**, 183901 (2015).
2. T. G. Philbin *et al.*, Science **319**, 1367 (2008).
3. K. E. Webb *et al.*, Nat. Commun. **5**, 4969 (2014).
4. L. Tartara, IEEE J. Quantum Electron. **48**, 1439 (2012).
5. B. H. Kolner, IEEE J. Quantum Electron. **30**, 1951 (1994).

A First-Principles Equation of State of CHON for Inertial Confinement Fusion Applications

S. Zhang,[1] V. V. Karasiev,[1] N. R Shaffer,[1] S. X. Hu,[1] D. Mihaylov,[1] K. Nichols,[1] R. Paul,[1] R. M. N. Goshadze,[1] M. Ghosh,[1] J. Hinz,[1] R. Epstein,[1] and S. Goedecker[2]

[1]Laboratory for Laser Energetics, University of Rochester
[2]Department of Physics, University of Basel, Switzerland

In laser-direct-drive (LDD) inertial confinement fusion (ICF) targets, a foam layer or ablator materials with radial density gradients can mitigate laser imprint and reduce hydrodynamic instabilities during ablation.[1,2] This can be realized by taking advantage of the two-photon polymerization (TPP) technique, which can precisely fabricate CHON polyacrylate resin into shell structures with superb lateral structure uniformity (to the level of 1 μm) (Ref. 3). To test the new ideas and optimize designs to improve target performance in relevant ICF and high-energy-density experiments, high-quality equations of state (EOS) of the target materials are required. In contrast to CH, however, which has been a widely used ablator material with relatively well understood EOS,[4–7] an EOS for CHON is still missing.

For this study, a wide-range (0 to 1044 g/cm^3 and 0 to 10^9 K) EOS table was constructed for a C-H-O-N quaternary compound ($C_{16}H_{27}O_6N_1$, stoichiometry that matches the resin material used in the laboratory for TPP printing) from first-principles simulations. The calculations combine two state-of-the-art approaches: Kohn–Sham density functional theory molecular dynamics (KS-DFT-MD) with an accurate meta-generalized gradient approximation (GGA)-level thermal exchange-correlation functional (T-SCAN-L) and orbital-free (OF) DFT-MD with lately developed Luo–Karasiev–Trickey γ Thomas–Fermi (LKTγTF) tunable noninteracting free-energy functionals. The thermal functional LKTγTF is constructed through a convex combination of LKT GGA[8] and Thomas–Fermi (TF)[9] functionals, where γ is determined for each density by matching the pressure from our OF-DFT-MD calculations at a high temperature (1 to 3×10^5 K) to the corresponding value from the KS-DFT-MD calculations; energies from OF-DFT-MD are uniformly shifted along each isochore to align with the KS-DFT-MD values at the matching temperature. This approach is similar but superior to previous EOS studies that stitch KS and OF but use TF functional in the OF calculations.[5,10,11] The first-principles EOS calculations are performed along 27 isochores (between 0.05 and 1044 g/cm^3) at 24 different temperatures (between 1000 and 10^9 K). The data have been extrapolated to lower densities and temperatures to produce a wide-range EOS table.

The EOS results show smooth bridging of KS and OF data at the matching condition. Figure 1 shows the EOS data approach the fully ionized ideal gas values in the limit of high temperatures (10^6 to 10^7 K, higher at higher densities). At lower temperatures, the energies and pressures for isochores of up to 4 to 7.5 g/cm^3 are below the ideal gas values because of the weaker ion and electron thermal contributions; for higher densities, the EOS increasingly exceeds the ideal gas values because of the increased degeneracy of electrons. The slope variations in the energy plots between different densities reflect changes in heat capacity; the differences between energy and pressure plots define the profile of the Grüneisen parameter. Both are caused by the joint effects of ion thermal vibration and electron thermal excitation.

Based on the calculated EOS, the predicted Hugoniot of CHON resin [Fig. 2(a)] shows a sharper profile and larger compression maximum by ~2% than that of pure CH polystyrene because of the coexistence of nitrogen and oxygen. Calculations of thermodynamic properties show overall consistency with that of CH along their respective Hugoniots [Figs. 2(b) and 2(c)]. Both exhibit a local minimum in heat capacity and maximum in the Grüneisen parameter at 2 to 3×10^4 K, which corresponds to

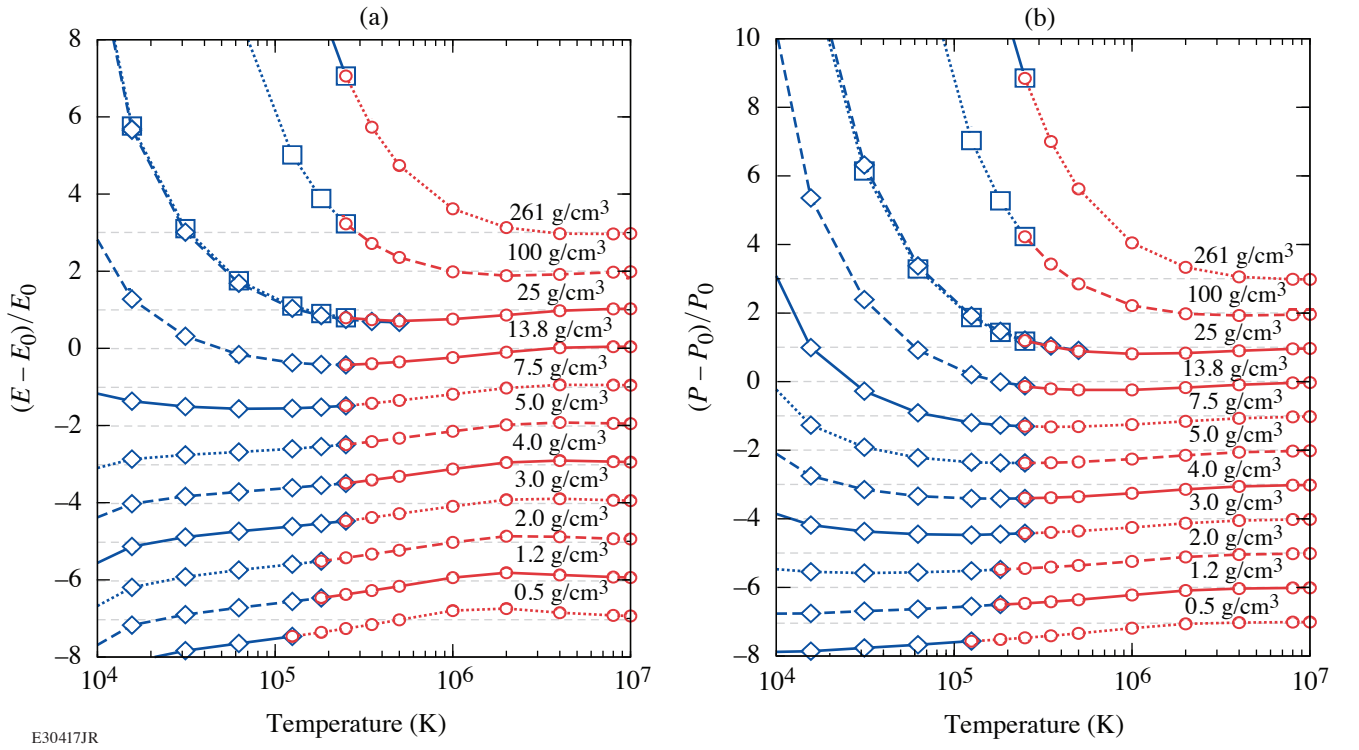

Figure 1
Matching KS (blue) and OF (red) (a) energies and (b) pressures along selected isochores. Data shown are relative to values of fully ionized ideal gas (denoted by E_0 and P_0 and shown with dashed gray horizontal lines). Blue diamonds and squares denote calculations using projector-augmented-wave and bare-coulomb potentials, respectively, which agree well with each other. Different isochores have been shifted apart for clarity.

bonded-to-atomic transition,[12] and a peak in heat capacity and a basin in the Grüneisen parameter at 10^6 K, corresponding to ionization of the K shell. The heat capacity and the Grüneisen parameters are found to reach the fully ionized ideal gas limit at 10^7 K. It is also found that the thermal expansion coefficient and the bulk sound velocity show independence of the isochore once the temperature exceeds 10^6 K.

To test the laser absorption and hydrodynamic efficiency of CHON resin as a potential ablator material for LDD targets, radiation-hydrodynamic simulations were performed of cryogenic DT implosion targets by using the 1-D radiation-hydrodynamics code *LILAC*.[13] The CHON results are compared with the conventional CH ablator. Results from the simulations show CHON outperforms CH as the ablator for LDD target designs (Fig. 3) due to a slight increase in the laser absorption fraction, which should further prompt the fabrication of the CHON shell with a foam layer for laser-imprint mitigation.

This material is based upon work supported by the Department of Energy National Nuclear Security Administration under Award Number DE-NA0003856, the University of Rochester, and the New York State Energy Research and Development Authority. V. V. Karasiev, D. I. Mihaylov, R. M. N. Goshadze, and S. X. Hu also acknowledge support by the U.S. NSF PHY Grant No. 1802964.

1. N. Metzler, A. L. Velikovich, and J. H. Gardner, Phys. Plasmas **6**, 3283 (1999).
2. S. X. Hu *et al.*, Phys. Plasmas **25**, 082710 (2018).
3. O. Stein *et al.*, Fusion Sci. Technol. **73**, 153 (2018)
4. M. A. Barrios *et al.*, Phys. Plasmas **17**, 056307 (2010).
5. S. X. Hu *et al.*, Phys. Rev. E **92**, 043104 (2015).
6. S. Zhang *et al.*, Phys. Rev. E **96**, 013204 (2017); S. Zhang *et al.*, J. Chem. Phys. **148**, 102318 (2018).

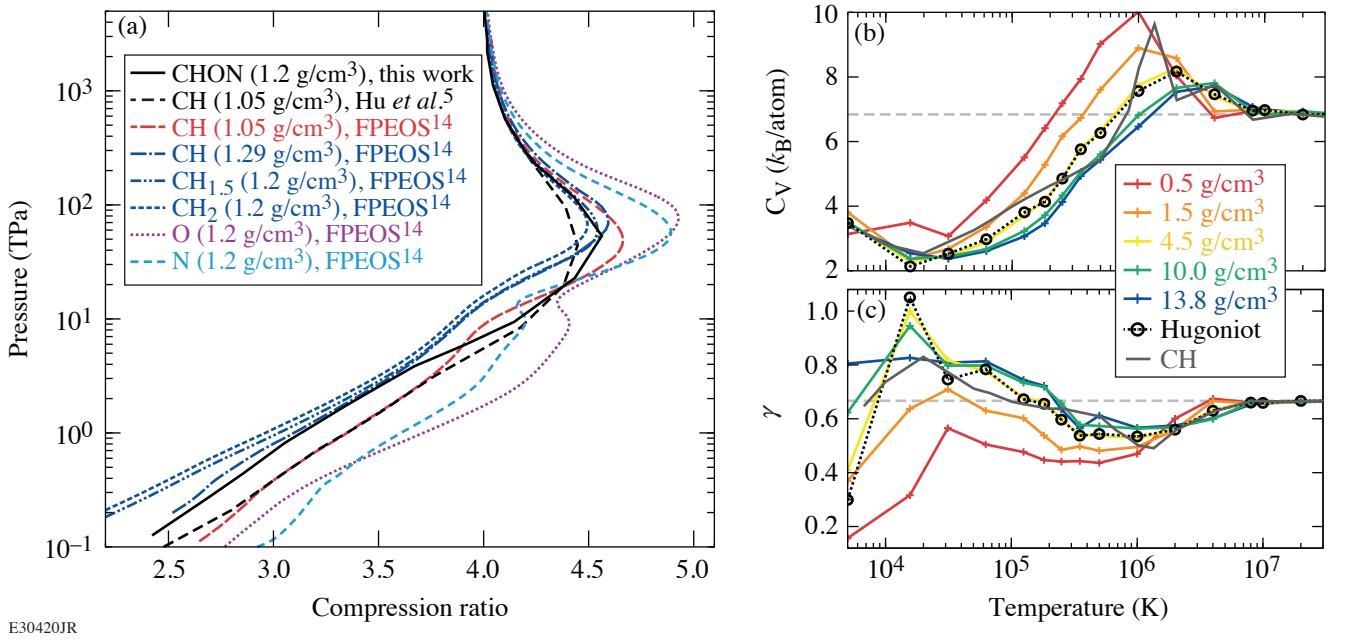

Figure 2
(a) Pressure-compression ratio Hugoniot, (b) heat capacity, and (c) Grüneisen parameter of CHON compared with that of CH. In (a), results of C–H compounds[5,6] and of O and N from first-principles EOS[14] are shown for comparison. In (b) and (c), the horizontal gray dashed lines denote the corresponding values of a fully ionized ideal gas.

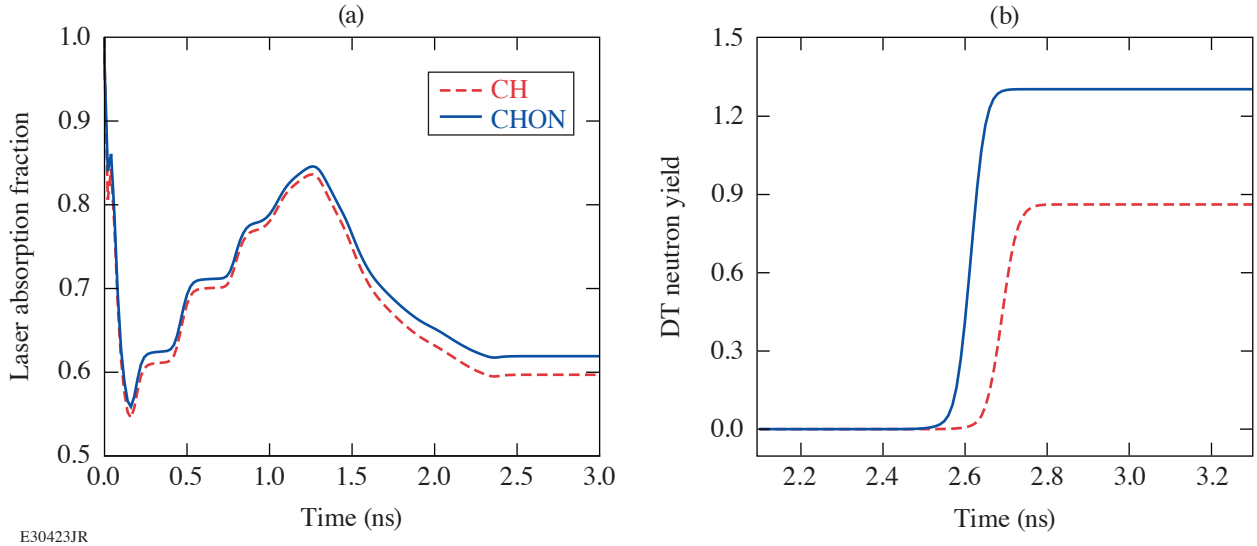

Figure 3
Comparison in (a) the time evolution of laser absorption fraction and (b) neutron yield at later time of the implosion when using targets with CH or CHON ablators. The simulations are based on a typical OMEGA-scale cryo-DT target with a 50-μm-thick DT-ice layer covered by 8-μm-thick CH ablator (ρ_0 = 1.05 g/cm^3) or 7-μm-thick CHON ablator (ρ_0 = 1.2 g/cm^3) to have equivalent target mass. The simulations employ the same laser pulse (total UV laser energy of ~27 kJ, shape optimized for the CH target assembly on OMEGA).

7. A. L. Kritcher *et al.*, Nature **584**, 51 (2020).
8. K. Luo, V. V. Karasiev, and S. B. Trickey, Phys. Rev. B **101**, 075116 (2020).
9. R. P. Feynman, N. Metropolis, and E. Teller, Phys. Rev. **75**, 1561 (1949).
10. S. X. Hu *et al.*, Phys. Rev. B **94**, 094109 (2016); Phys. Rev. E **95**, 043210 (2017).
11. Y. H. Ding and S. X. Hu, Phys. Plasmas **24**, 062702 (2017).
12. S. Zhang *et al.*, J. Appl. Phys. **131**, 071101 (2022).
13. J. Delettrez *et al.*, Phys. Rev. A **36**, 3926 (1987).
14. B. Militzer *et al.*, Phys. Rev. E **103**, 013203 (2021).

Shocked-Silica Aerogel Radiance Transition

B. J. Henderson,[1,2] J. R. Rygg,[1,2,3] M. C. Marshall,[1] M. K. Ginnane,[1] L. E. Hansen,[4] E. Davies,[5] P. M. Celliers,[5] and G. W. Collins[1,2,3]

[1]Laboratory for Laser Energetics, University of Rochester
[2]Department of Physics and Astronomy, University of Rochester
[3]Department of Mechanical Engineering, University of Rochester
[4]Sandia National Laboratories
[5]Lawrence Livermore National Laboratory

The objective of this work was to measure the radiance of shock fronts in SiO_2 aerogel at various initial densities. The optical properties of shock-compressed fused silica, quartz,[1] and stishovite[2] have been characterized and used as standards for temperature and reflectance measurements.[3] This work measures the optical radiant behavior of shock-compressed SiO_2 aerogel, which is expected to be significantly hotter, and thus brighter, at comparable shock pressures, than shock-compressed SiO_2 starting at solid density.[4,5] These measurements can be used to constrain radiative-hydrodynamics in inertial confinement fusion simulations of implosions using aerogel liners and to generate an optimally bright broadband source for high-energy-density–physics experiments.

Experiments were performed on the OMEGA EP Laser System. Targets were irradiated by one to four laser beams (λ = 351 nm) on a polystyrene (CH) ablator, producing strong shock waves that compress the planar samples. These experiments used laser irradiance between 10 and 200 TW/cm^2 produced by 2-, 2.5-, and 4-ns temporally square and ramp-top laser pulses with spatially uniform spot diameters of approximately 1100 or 1800 μm through the use of distributed phase plates. The targets were composed of a 40-μm CH ablator (refractive index n = 1.59 at λ = 532 nm, ρ_0 = 1.05 g/cm^3), a 50-μm quartz pusher (n = 1.547, ρ_0 = 2.65 g/cm^3), and a 250-μm SiO_2 aerogel sample (n = 1.02 to 1.06, ρ_0 = 0.1 to 0.3 g/cm^3). Shock velocity, reflectivity, and radiance were measured using a velocity interferometer for any reflector (VISAR) and a streaked optical pyrometer (SOP).

Brightness temperature of the shocked aerogel was determined by measuring the radiance of the shock front using the SOP. The SOP collects time- and spatially resolved thermal emission from the shock front integrated over wavelengths between 590 and 850 nm, with a peak efficiency at 600 nm. The SOP signal is converted to brightness temperature using an absolute calibration of the OMEGA EP SOP, which follows the procedure described in Ref. 6.

SiO_2 aerogel exhibits behavior that is starkly different from its higher-density counterparts (Fig. 1). Specifically, the exponent of the power law fit a is ~2 with no observed slope change for fused silica, quartz, and stishovite. For SiO_2 aerogel, a is 2 below the change in slope and ~1 above the change in slope. Below the change in slope observed in aerogel, the six T_{bright}–P curves for SiO_2 form a set of parallel lines. Some possible causes for this behavior include: (a) radiative precursor ahead of the shock, (b) a conductive precursor, and (c) shock propagation in aerogel microstructure.

This material was based upon work supported by the Department of Energy National Nuclear Security Administration under Award No. DE-NA0003856, the University of Rochester, and the New York State Energy Re-search and Development Authority. A portion of this work was performed under the auspices of NSF Physics Frontier Center Award No. PHY-2020249, and under the auspices of the U.S. Department of Energy by Lawrence Livermore National Laboratory under Contract No. DE-AC52-07NA27344.

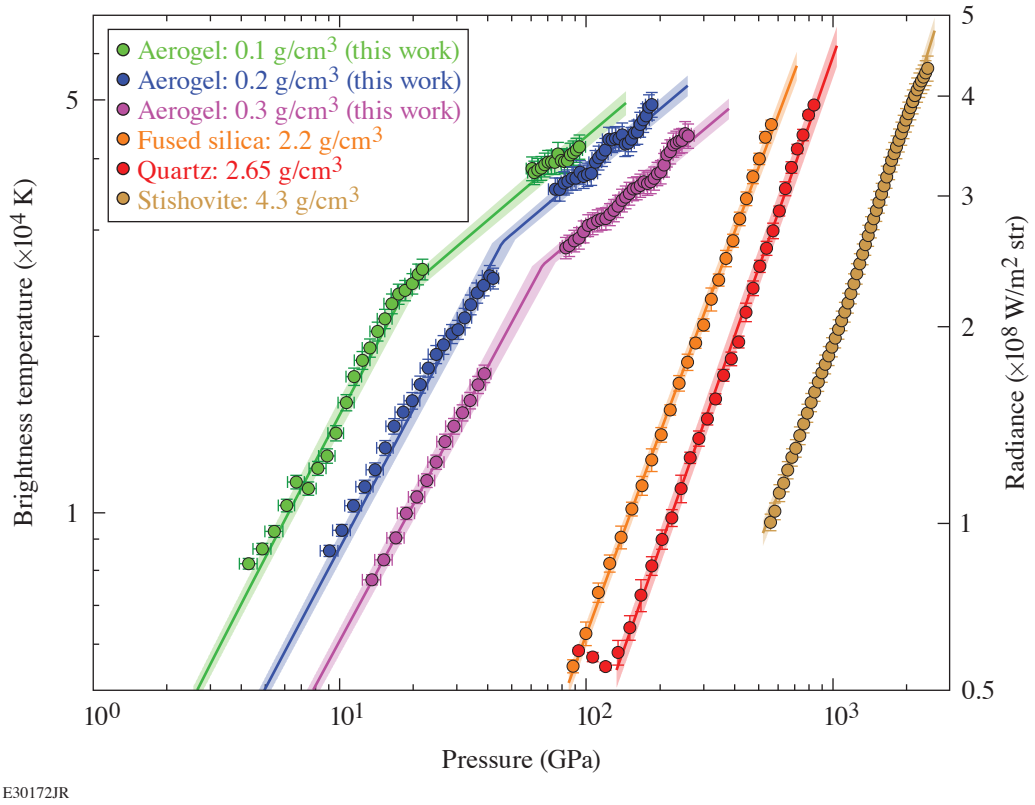

Figure 1
Brightness temperature (and integrated radiance in the 590- to 850-nm band) versus inferred pressure for shock compressed SiO_2 aerogel (green, blue, and pink circles) and their two-part power-law fits (green, blue, and pink curves). Shaded regions represent 1σ confidence intervals. Measurements of fused silica (orange circles),[1] quartz (red circles),[1] and stishovite (brown circles)[2] are fit with a single power-law function (orange, red, and brown curves).

1. D. G. Hicks *et al.*, Phys. Rev. Lett. **97**, 025502 (2006).
2. M. Millot *et al.*, Science **347**, 418 (2015).
3. S. Brygoo *et al.*, J. Appl. Phys. **118**, 195901 (2015).
4. J. C. Boettger, Los Alamos National Laboratory NM, New Mexico, Report LA-11488-MS (1989).
5. Ya. B. Zel'dovich and Yu. P. Raĭzer, in *Physics of Shock Waves and High-Temperature Hydrodynamic Phenomena*, edited by W. D. Hayes and R. F. Probstein (Academic Press, New York, 1966), Vol. I, Chap. II, pp. 107–175.
6. M. C. Gregor *et al.*, Rev. Sci. Instrum. **87**, 114903 (2016).

Shock-Induced Metallization of Polystyrene Along the Principal Hugoniot Investigated by Advanced Thermal Density Functionals

R. M. N. Goshadze, V. V. Karasiev, D. I. Mihaylov, and S. X. Hu

Laboratory for Laser Energetics, University of Rochester

Use of a recently developed thermal strongly constrained and appropriately normed Laplacian (T-SCAN-L)-dependent meta-generalized gradient approximation exchange correlation (XC) density functional[1] and thermal hybrid XC density functional (KDT0)[2] within the framework of density functional theory as implemented in Vienna *ab-initio* simulation package (VASP) to show that the inclusion of thermal and inhomogeneity effects is crucial for accurate prediction of structural evolution and corresponding insulator–metal transition (IMT) during shock compression. Optical reflectivity calculated as an indicator of IMT is in perfect accord with experimental data.[3] The discrepancy between experiment and *ab-initio* simulation results was reported several times during last decade.[4–6]

The equation of state (EOS) of shocked material just behind the shock front satisfies the Rankine–Hugoniot equation

$$E_1 - E_0 + \frac{1}{2}(P_1 + P_0)\left(\frac{1}{\rho_1} - \frac{1}{\rho_0}\right) = 0,$$

where the subscripts "0" and "1" stand for unshocked and shocked sides, respectively. The unshocked side of the ablator (CH) is in ambient conditions. At ambient conditions (T = 300 K and ρ = 1.055 g/cm^3), the pressure P_0 can be approximated by zero since it is orders of magnitude lower than the pressure at ~10^3 K. Based on the results from the *ab-initio* molecular dynamics (AIMD) calculations, E_0 is set to be –93 kJ/g.

Figure 1 shows the comparison between various experimental and theoretical studies of principal Hugoniot on the pressure–density plane. Both Perdew–Burke–Ernzerhof (PBE)[5] and T-SCAN-L AIMD calculations overestimate shock pressure compared

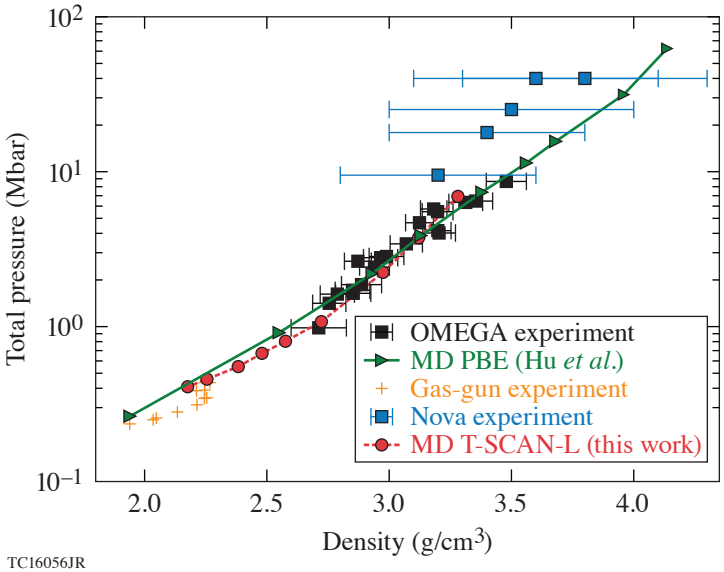

Figure 1
CH pressure as a function of density along the principal Hugoniot. The T-SCAN-L results are compared with PBE calculations by Hu *et al.*,[5] the Nova experiment,[7] gas-gun experiment,[8] and the OMEGA experiment[3] based on latest quartz EOS (black rectangles).

to a gas-gun[8] experiment below 1 Mbar. In the mid-pressure range (1 to 10 Mbar), T-SCAN-L shows concave behavior opposing more-linear PBE results. Apart from using a higher-rung XC functional with explicit temperature dependence, this change might also be associated with the proper treatment of structural characteristics of shocked CH. We carefully run structural relaxation until no structure remains, observing melting/dissociation exactly at these mid-range pressures.

Optical calculations are performed within the Kubo–Greenwood formalism, obtaining CH reflectivity by averaging the uncorrelated snapshots of ionic configurations from the AIMD simulations. The details of the process can be found in Ref. 5. A comparison of the results from the calculations with the OMEGA experiment and PBE-based AIMD study[5] is shown in Fig. 2. Note that the reflectivity turn-on point is shifted to higher pressures and the jump is much sharper, making it in perfect agreement with the OMEGA experiment. By separately plotting the results obtained by T-SCAN-L and KDT0 on top of the T-SCAN-L–generated ionic configurations in Fig. 2, we demonstrate that the improved results are the consequence of not only accurate ionic configurations, but also accurate electronic structure calculations. There are several factors that contribute to this enhancement. Foremost, our PBE calculations show that it underestimates the drop in density of states (DOS) as compared to T-SCAN-L at exactly the same conditions as shown in Fig. 3, which shows a comparison of DOS in the temperature range from 3500 to 5000 K along the principal Hugoniot. The second aspect is the shift in Hugoniot data. At lower densities, T-SCAN-L gives lower Hugoniot pressures compared to PBE calculations. As a result, the Hugoniot points at a fixed density predicted by T-SCAN-L have much less molecular dissociation and consequently exhibit a deeper drop in DOS, leading to smaller reflectivity.

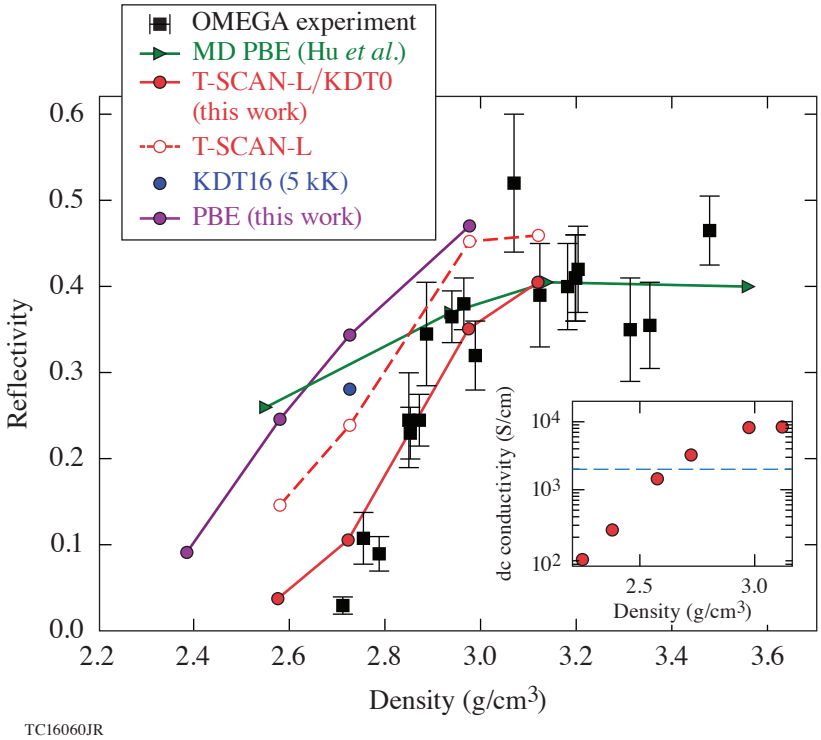

Figure 2
Reflectivity of shocked CH along the principal Hugoniot at 532-nm VISAR (velocity interferometer system for any reflection) light.

This material is based upon work supported by the Department of Energy National Nuclear Security Administration under Award Number DE-NA0003856 and US National Science Foundation PHY Grant No. 1802964.

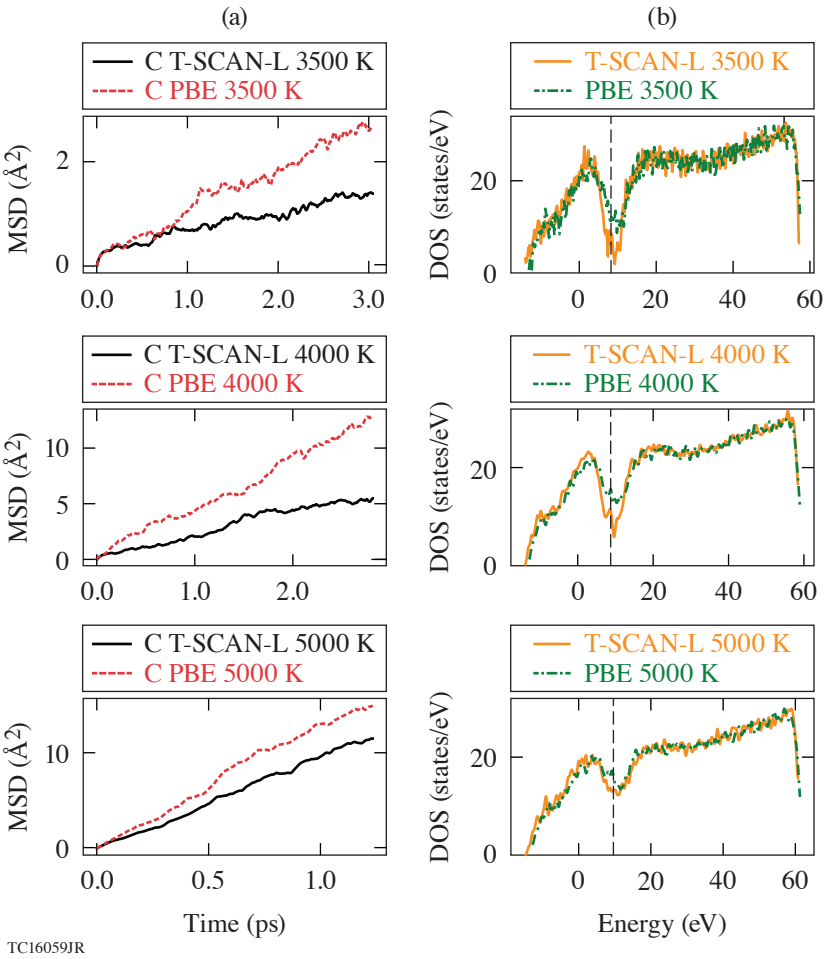

Figure 3
(a) Comparison of mean square displacement predicted by PBE versus TSCAN-L XC functionals and (b) comparison of corresponding DOS in the temperature range of 3500 to 5000 K. MSD: mean squared displacement.

1. V. V. Karasiev, D. I. Mihaylov, and S. X. Hu, Phys. Rev. Lett. **105**, L081109 (2022).
2. D. I. Mihaylov, V. V. Karasiev, and S. X. Hu, Phys. Rev. B **101**, 245141 (2020).
3. M. A. Barrios *et al.*, Phys. Plasmas **17**, 056307 (2010).
4. C. Wang, X.-T. He, and P. Zhang, Phys. Plasmas **18**, 082707 (2011).
5. S. X. Hu, T. R. Boehly, and L. A. Collins, Phys. Rev. E **89**, 063104 (2014).
6. N. J. Hartley *et al.*, Matter Radiat. Extremes **5**, 028401 (2020).
7. R. Cauble *et al.*, Phys. Plasmas **4**, 1857 (1997).
8. S. P. Marsh, ed. LASL Shock Hugoniot Data, Los Alamos Series on Dynamic Material Properties (University of California, Berkeley, CA, 1980).

The 13th Omega Laser Facility Users Group Hybrid Workshop

J. A. Frenje,[1] S. Ali,[2] E. Merritt,[3] K. Falk,[4] S. Finnegan,[3] M. Gatu Johnson,[1] J. P. Knauer,[5] M. P. Valdivia,[6] and L. Willingale

[1]Massachusetts Institute of Technology
[2]Lawrence Livermore National Laboratory
[3]Los Alamos National Laboratory
[4]Helmholtz-Zentrum Dresden-Rossendorf, Germany
[5]Laboratory for Laser Energetics, University of Rochester
[6]University of California, San Diego
[7]University of Michigan

Overview

On 27–29 April 2022, 158 researchers from more than 40 universities and laboratories and 13 countries gathered at LLE for the 13th Omega Laser Facility Users Group (OLUG) Hybrid Workshop (Fig. 1). Of these researchers, 103 had registered to attend the workshop in person and 55 had registered to attend the workshop virtually. The main goal of the three-day workshop was to facilitate a continuing dialog among the Omega users, the users and LLE management, and the users and the broader scientific community along with providing an opportunity for students and postdoctoral fellows to present their research at LLE in an interactive and informal atmosphere. What makes the annual OLUG Workshop unique is that it brings users together from all over the world, facilitating a vibrant dialog among them about their experiences running experiments at Omega, as can be seen in photographs shown in this summary.

U2877JR

Figure 1
In-person attendees at the 13th OLUG Hybrid Workshop.

A major part of OLUG's responsibility is to enhance the Omega Laser Facility and its capabilities by defining a set of Findings and Recommendations (F&R's) each year. In this year's workshop, the F&R discussions were stimulating and lively. As shown at the end of this report, 25 F&R's were defined and grouped into several categories. LLE management use these F&R's as a guide for making decisions about the Omega Laser Facility operations, priorities, and future changes.

The workshop included five science talks given by leading world authorities that described the breadth and excitement of high-energy-density (HED) science undertaken at Omega and other facilities in U.S. Two facility talks about the future of Omega proved especially enlightening to the OLUG participants. The workshop attendees also had a chance to hear the National Nuclear Security Administration's (NNSA's) and National Science Foundation's (NSF's) perspectives on the research conducted at Omega and how it fits into their national programs. A summary of this year's OLUG Executive Committee (ExCom) election was also presented. Another workshop highlight was the evening tutorial session given by LLE, in which the gas-jet platform, the MIFEDS (magneto-inertial fusion electrical discharge system) experimental platform, and as the *PlasmaPy* and *Fiducia* open-source codes were presented.

A student/postdoctoral-panel discussion was held to focus on their experiences at Omega and present their thoughts and recommendations on facility improvements. Several discussions were sparked by this forum, which resulted in the student/postdoctoral report summarized at the end of this summary. Another important event was the discussion on careers in HED science, which brought students together with potential future employers.

A total of 51 students and postdoctoral fellows (Fig. 2), 36 of whom were supported by travel grants from NNSA, attended the workshop and presented three sessions of posters. The presentations involved a large range of topics including target fabrication, inertial confinement fusion (ICF) experiments and simulations, and laboratory astrophysics, all of which generated spirited discussions, probing questions, and many suggestions. An award ceremony for the best student and postdoc posters was also held.

U2878JR

Figure 2
A total of 51 students and postdoctoral fellows attended the workshop and made engaging poster presentations.

The Workshop Presentations

A wide-ranging series of presentations and posters were presented during the workshop. The invited presentations covered facility, government, and science. The science talks focused on several interesting topics, including high-energy-density plasmas, laboratory astrophysics, and burning plasmas in ICF. Two facility talks—"The Renewal of the Five-Year LLE Cooperative Agreement" by Acting LLE Director Dr. Chris Deeney and "The LLE Sustainment Plan" by Omega Laser Facility Division Director Mr. Samuel Morse—presented important details on the status, performance, and path forward of the Omega Laser Facility. Mr. Morse also gave an enlightening talk on the "OMEGA Facility Update and Progress on OLUG Recommendations." Dr. Sarah Nelson, Acting Director of the NNSA Office of Experimental Sciences, presented an excellent perspective on the importance of the Omega facility within her program, and Dr. Slava Lukin, the Director for Plasma Physics at NSF, provided an informative overview of his program and the importance of training and educating the next-generation scientist in the area of plasma physics. In addition to the invited presentations, 63 contributed posters, presented in three sessions, covered a wide spectrum of work at Omega including target fabrication, ICF experiments, diagnostics, HED-plasma theory and simulations, laboratory astrophysics, material science, and laser–plasma interactions along with diversity, equity, and inclusion. Out of these posters, 51 were presented by graduate students, postdocs, and undergraduate students. These poster sessions offered ample opportunities for informal discussions about Omega experiments and their connections to work at other facilities. A set of four exciting facility talks were also given by LLE in an evening tutorial session. Figures 3–8 provide a representative sampling of the workshop's presentations and ambience.

Figure 3
In the plenary sessions, authorities spoke about science opportunities, government perspectives, and the evolving capabilities of the Omega Laser Facility to enable new science frontiers. (a) Dr. Chris Deeney, the Acting LLE Director, kicked off the workshop with a perspective on the renewal of the five-year LLE Cooperative Agreement; (b) Prof. Petros Tzeferacos of the University of Rochester (UR) gave an inspiring presentation on the Flash Center for Computational Science at the UR, and (c) Dr. Sarah Nelson, the Acting Director of the NNSA Office of Experimental Sciences, provided a bigger-picture perspective on the importance of the Omega Laser Facility within her program.

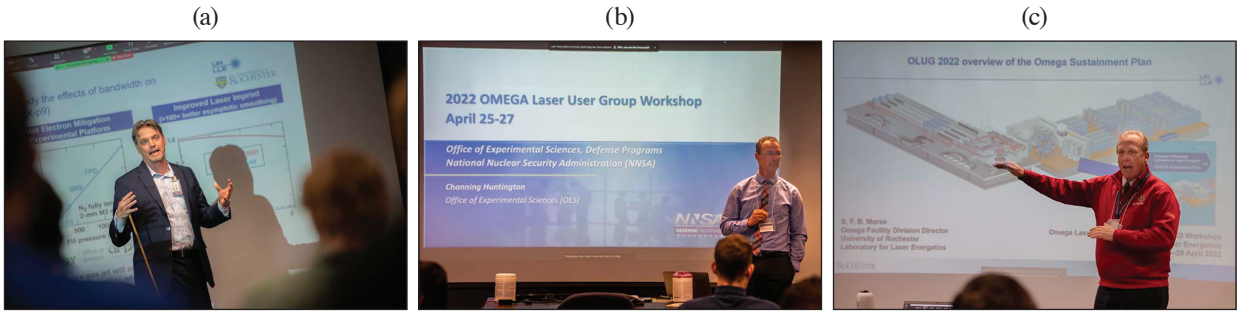

Figure 4
(a) UR Prof. Dustin Froula gave an exciting talk on the science that can be done on the Fourth-Generation Laser for Ultra-broadband eXperiments (FLUX); (b) Dr. Channing Huntington provided a wonderful personal account on his journey from a graduate student at University of Michigan (UM), conducting experiments at Omega, to working at the NNSA Office of Experimental Sciences; and (c) Samuel Morse (LLE) discussed the Omega sustainment plan, which is critical to the future of the laboratory and to the OLUG community. Mr. Morse's extensive knowledge of the facility is invaluable to those planning Omega experiments.

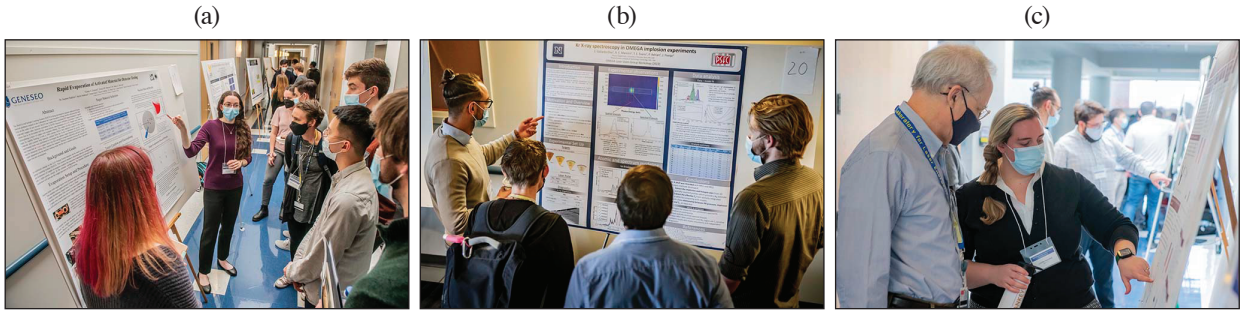

Figure 5
Sixty-three posters were presented in three sessions on a wide spectrum of work at Omega. Out of these posters, 51 were presented by graduate students, postdocs, and undergraduate students. In an interactive yet informal setting, these poster sessions provided opportunities for students and young researchers to present their research from Omega experiments and their connections to work at other facilities. (a) Undergraduate students Vizma Leimanis and Jessica Dawson [State University of New York (SUNY) Geneseo] discussed their work on "Rapid Evaporation of Activated Material for Detector Testing" with OLUG ExCom member Dr. Maria Gatu Johnson (MIT) and other students; (b) graduate student Enac Gallardo-Villaseca (University of Nevada, Reno) presented his work on "Krypton X-Ray Spectroscopy in OMEGA Implosion Experiments;" and (c) graduate student Camille Samulski (Virginia Tech) discusses her poster with LLE Senior Scientist Dr. Reuben Epstein on "Single-Feature Perturbation Seeded Rayleigh–Taylor Instability Studied in Planar Geometry."

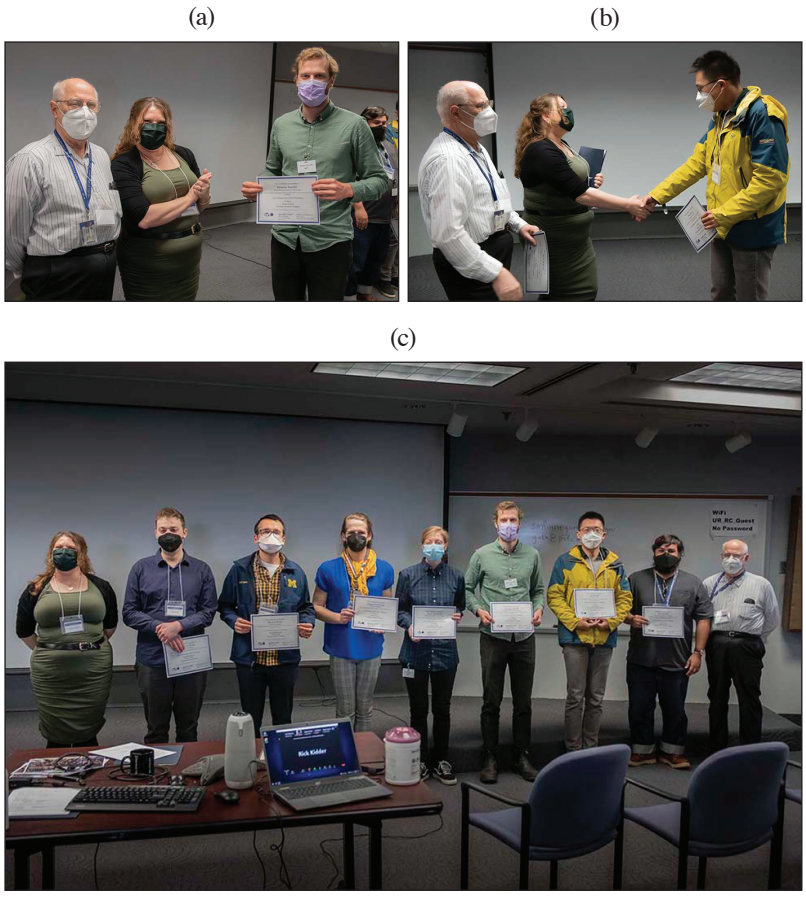

Figure 6
An award ceremony chaired by Drs. Liz Merritt and Jim Knauer was held for the best student and postdoctoral posters. (a) Graeme Sutcliffe (MIT) won the graduate student category; (b) Shu Zhang (Princeton) won the postdoctoral category. (c) Dr. Liz Merritt, Cameron Frank (graduate student at the University of Delaware), Michael Wadas [graduate student at UM (University of Michigan)], Abigail Armstrong (graduate student at UR), Skylar Dannhoff (graduate student at MIT), Graeme Sutcliffe (graduate student at MIT), Shu Zhang (postdoc at Princeton), Neel Kabadi (postdoc at MIT), and Dr. Jim Knauer. Not shown in the picture are Justin Kunimune (graduate student at MIT), Adam Brown (Houghton College) who won the undergraduate student category, and Jovahn Roumell (undergraduate student at SUNY Geneseo).

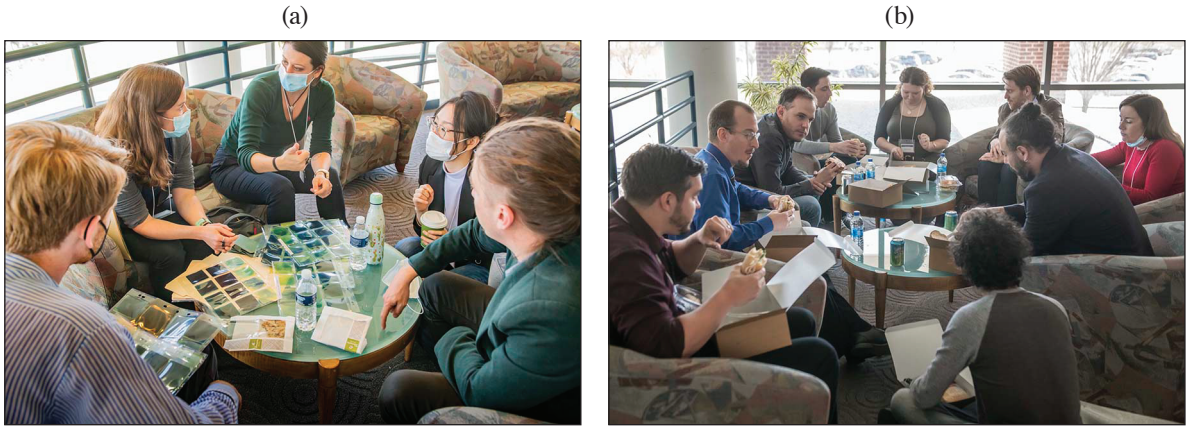

U2883JR

Figure 7
Productive discussions among researchers from around the world occurred in several informal settings.

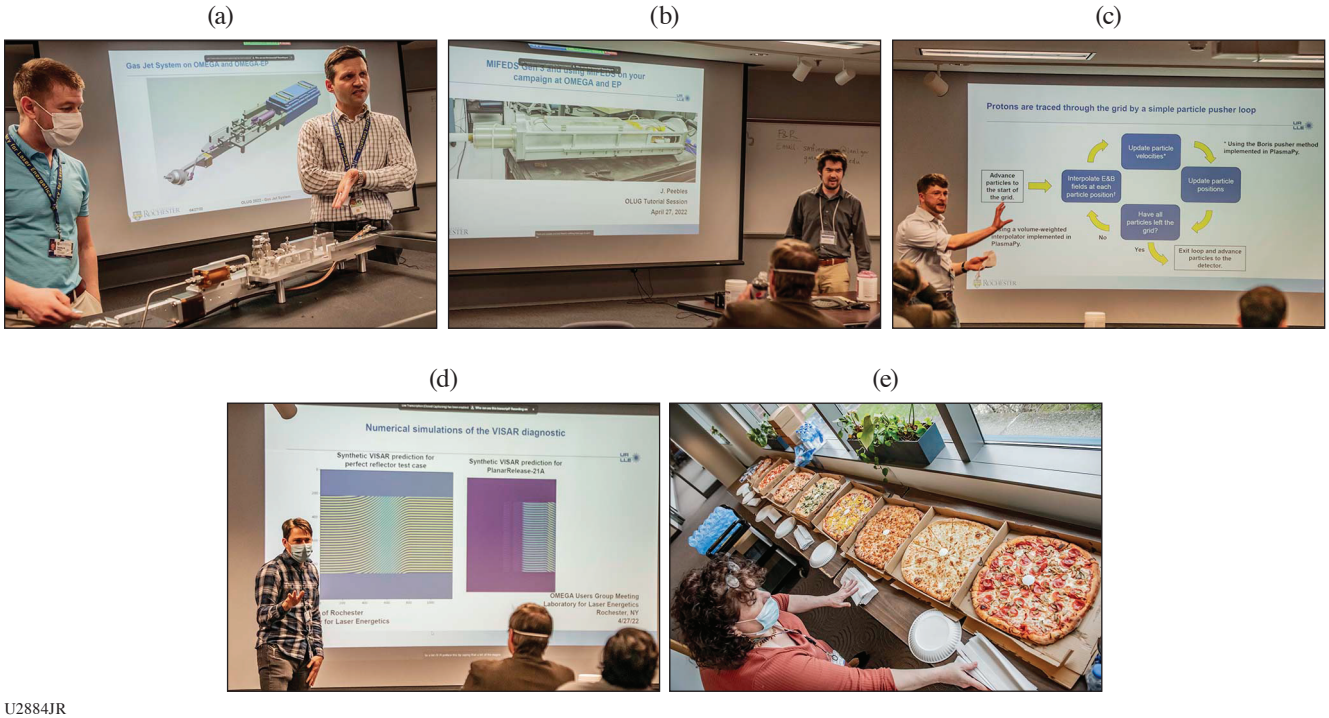

U2884JR

Figure 8
An evening tutorial session given by LLE highly regarded by the OLUG workshop participants. (a) Dr. Steven Ivancic and Tim Filkins discussed the "Gas-Jet System on OMEGA and OMEGA EP," which helped the external users get a better idea of what can be done with the system; (b) Dr. Jonathan Peebles gave an informative presentation on the "MIFEDS Generation-3 and Using It on Users' Experimental Campaign on OMEGA and OMEGA EP;" (c) Dr. Peter Heuer gave an inspiring talk on the "*PlasmaPy* Open-Source Code," which truly engaged the younger audience; (d) Dr. Daniel Barnak presented "*Fiducia* Open-Source Code and Analysis Software for the Dante-Diagnostic Data;" and (e) Mrs. Kim Truebger arranged for pizza to be served during the evening's tutorial session.

Figure 9
The student/postdoctoral panel presented important insights from young researchers working at the Omega facility. (a) Suzanne Ali (LLNL), not shown, Heath LeFevre (UM), Ellie Tubman (LLNL), Gabriel Perez-Callejo (University of Valladolid, Spain), and Brandon Russel (UM) led the discussion. (b) Graduate student Hongmei Tang (UM) brought her thoughts and recommendations.

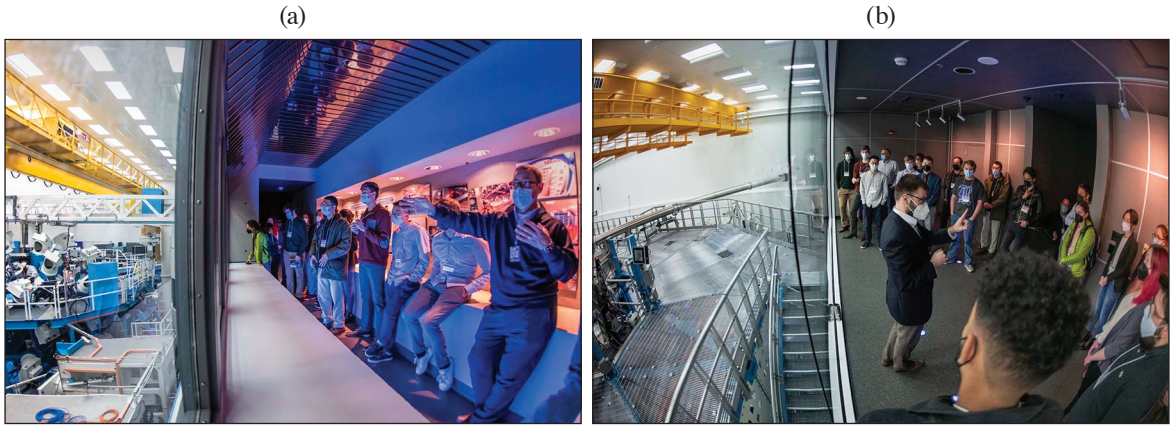

Figure 10
Mark Labuzeta and David Canning led tours of OMEGA and OMEGA EP, respectively. For many of the younger researchers, this was a great opportunity to learn about the facilities.

Summary of Findings and Recommendations

A big part of OLUG's responsibility is to enhance the Omega facility and its capabilities by defining a set of F&R's each year. Drs. Maria Gatu Johnson (MIT) and Sean Finnegan [Los Alamos National Laboratory (LANL)] led this year's F&R session, As shown below, 25 F&R's were defined and grouped into several categories at this workshop, i.e., general (1), documentation (2), calibration (3), diagnostics (4–15), target capability (16–18), laser systems (19–22), and data management (23–25). The LLE management is using these F&R's as a guide for making decisions about the operations of the Omega Laser Facility, priorities, and future changes. An update on the implementation of these F&R's will be presented by the LLE management at the OLUG satellite meeting on 18 October 2022 at the American Physical Society Division of Plasma Physics (APS-DPP) Conference in Spokane, WA.

1. Add equipment for improved hybrid workshop execution.
2. Ensure that users have access to detailed up-to-date documentation on diagnostics.
3. Make calibration data readily available on the PI portal.

4. Add a third VISAR (velocity interferometer system for any reflector) leg on the active shock breakout (ASBO) diagnostic on OMEGA EP and/or OMEGA.
5. Increase VISAR etalon support thickness for improved ASBO resolution.
6. Add a timing fiducial to Dante, noted in the Sustainment Plan (requires modern digitizers).
7. Add an optical Thomson-scattering diagnostic to OMEGA EP (multiple submissions).
8. Add the capability to infer directional flow vector on D_2 gas-filled or low-DT yield implosions.
9. Add the capability for neutron time-of-flight detectors to measure secondary DT-neutron spectra.
10. Reduce min/max camera timing jitter.
11. Improve Dante maintenance and documentation.
12. Create the ability to run streaked x-ray diagnostics with a gas jet.
13. Add gated spatially resolved x-ray spectroscopy.
14. Provide an additional Target Positioning System, more (mini) ten-inch manipulators (TIM's) and/or nuclear diagnostic inserters for OMEGA.
15. Add a diagnostic for forward-scattered light on OMEGA EP.
16. Characterize gas-jet nozzles (a TIM lab nozzle characterization test bench is now available to users).
17. Provide planar cryo on OMEGA EP.
18. Enable the ability to change MIFEDS leads on shot day
19. Increase UV power on OMEGA EP.
20. Enable 20-ns pulse duration on OMEGA EP.
21. Increase the quantity of tight-focus circular super-Gaussian distributed phase plates.
22. Extend backlighter beam delay.
23. Update HDF5 and utilize standard meta-data formats (multiple submissions).
24. Enable instant analysis of data on shot day.
25. Develop more open-source analysis software.

Findings and Recommendations from the Student/Postdoctoral Panel

Every year at the OLUG Workshop, a group of early career scientists, mainly students and postdocs, lead a discussion with the community on topics relevant to young researchers, including issues specific to the pandemic effects on early career scientists, the organization of the OLUG Workshop, and recommendations for the facility. Suzanne Ali [Lawrence Livermore National Laboratory (LLNL)] and Heath LeFevre (UM) led the discussion together with Ellie Tubman (LLNL), Gabriel Perez-Callejo (University of Valladolid, Spain), and Brandon Russel (UM). From these discussions, the following F&R were identified:

1. Develop a better framework for mentorship and guidance for early career scientists.
2. Facilitate cross-institution mentorship, matching up new researchers doing work at Omega with more-experienced mentors.
3. Form something like a journal club for topics related to experimental planning and analysis (monthly or biweekly, with a pre-meeting poll on the discussion topic).
4. Improve and modernize the web-based resources available to users.
5. Continue to improve documentation for diagnostic systems and targets.
6. Better advertise the existing online forum. A Microsoft Teams channel (or similar) is recommended specifically for users to ask questions to other users.
7. Record tutorials for some of the online resources for data access.
8. Enable access to calibration information for diagnostics via an online database.

Nominations and Election of Members for the OLUG ExCom

An OLUG ExCom election was held this year to elect three new members. A nominating committee was formed in November 2021 to request January nominations for the February 2022 election. Pia Valdivia [Chair, University of California, San Diego (UCSD), Hui Chen (LLNL), and Lan Gao (Princeton Plasma Physics Laboratory) formed the election committee. From a three-candidate ballot, Derek Schaeffer (Princeton) was elected as university representative to replace Maria Gatu Johnson (MIT); Verena Geppert-Kleinrath (LANL) was elected as national lab representative to replace Liz Merritt (LANL); and Heath LeFevre

(UM) was elected as the junior representative to replace Suzanne Ali (LLNL). In addition, Jim Knauer stepped down as the LLE ex-officio after 13 years of service. Jessica Shaw is the new LLE ex-officio.

For the May 2022–April 2023 period, the OLUG ExCom members are (a) four from U.S. university/small business: Johan Frenje (MIT, Chair), Maria-Pia Valdivia (UCSD, Vice Chair), Derek Schaeffer (Princeton), and Louise Willingale (UM); (b) three from national laboratory/major business: Verena Geppert-Kleinrath (LANL), Sean Finnegan (LANL), and Alison Saunders (LLNL); (c) one non-U.S. researcher: Katerina Falk [Helmholtz-Zentrum Dresden-Rossendorf (HZDM), Germany); (d) one from the junior researcher list: Heath LeFevre (UM); and (e) LLE ex-officio: Jessica Shaw. The OLUG ExCom thanks Maria Gatu Johnson, Liz Merritt, Suzanne Ali, and Jim Knauer for their service and excellent work making OLUG such a vibrant community.

U2887JR

Figure 11
Dr. Pia Valdivia (UCSD) presented the results from the 2022 OLUG ExCom elections.

(a)

(b)

(c)

(d)

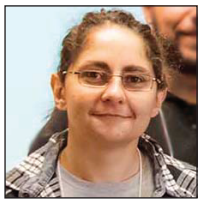

U2888JR

Figure 12
Members of the 2022 OLUG ExCom. (a) Back row (left to right): Jim Knauer (LLE), Liz Merrit (LANL), Katerina Falk (HZDR), Sean Finnegan (LANL), and Pia Valdivia (UCSD). Front row (left to right): Johan Frenje (MIT) and Maria Gatu Johnson (MIT); (b) Alison Saunders (LLNL); (c) Louise Willingale (UM); and (d) Suzanne Ali (LLNL) attended the workshop virtually.

Conclusions and Future Workshops

This OLUG Workshop, with 158 attendees, was part of a process that will keep members of the community involved in conversations and collaborations with each other and with the Omega Laser Facility. In addition, OLUG ExCom members and LLE management have an ongoing dialog to assess progress, compatibility with facility resources, and impact toward the implementation of the F&R's. An update on the implementation of these F&R's will be presented by the LLE management at the OLUG satellite meeting on 18 October 2022 at the APS-DPP Conference in Spokane, WA, and in depth at the 2023 OLUG Workshop.

Acknowledgment

This OLUG workshop was made possible in part by LLE at the University of Rochester for the use and availability of critical resources and support. In addition, OLUG thanks the LLE management for their exceptional responsiveness to our F&R's. For capturing the ambience and spirit of the workshop through his camera lens, we thank Eugene Kowaluk. To NNSA, we gratefully acknowledge the financial assistance for student/postdoctoral travel expenses. We also thank Kim Truebger for her incredible work setting up and executing the workshop.

FY22 Q3 Laser Facility Report

J. Puth, M. Labuzeta, D. Canning, and R. T. Janezic

Laboratory for Laser Energetics, University of Rochester

During the third quarter of FY22, the Omega Facility conducted 337 target shots on OMEGA and 242 target shots on OMEGA EP for a total of 579 target shots (see Tables I and II). OMEGA averaged 10.5 target shots per operating day, averaging 94.9% Availability and 94.7% Experimental Effectiveness. OMEGA EP averaged 8.3 target shots per operating day, averaging 95.4% Availability and 98.8% Experimental Effectiveness.

Table I: OMEGA Laser System target shot summary for Q3 FY22.

Program	Laboratory	Planned Number of Target Shots	Actual Number of Target Shots
ICF	LLE	66	61
	LANL	11	11
	LLNL	16.5	17
	SNL	5.5	6
ICF Subtotal		99	95
HED	LLE	33	38
	LANL	22	22
	LLNL	27.5	31
	SNL	11	12
HED Subtotal		93.5	103
LBS	LLNL	22	24
LBS Subtotal		22	24
NLUF		60.5	67
CEA		5.5	6
APL		11	12
CMAP		11	8
Calibration	LLE	0	22
Grand Total		302.5	337

APL: Applied Physics Labs (Johns Hopkins University)
CEA: Commissariat à l'énergie atomique aux énergies alternatives
CMAP: Center for Matter at Atomic Pressures
NLUF: National Laser Users Facility

Table II: OMEGA EP Laser System target shot summary for Q3 FY22.

Program	Laboratory	Planned Number of Target Shots	Actual Number of Target Shots
ICF	LLE	35	49
	LLNL	7	7
	SNL	7	6
ICF Subtotal		49	62
HED	LLE	14	17
	LANL	14	22
	LLNL	49	68
	SNL	7	10
HED Subtotal		84	117
CMAP		7	11
LaserNetUS		7	9
NLUF		28	25
Calibration	LLE	0	18
Grand Total		175	242

Publications and Conference Presentations

Publications

N. Acharya, H. Aluie, and J. K. Shang, "Numerical Investigation of Laser-Driven Shock Interaction with a Deformable Particle," Phys. Plasmas **29**, 052302 (2022).

S.-W. Bahk, I. A. Begishev, R. Roides, C. Mileham, R. Cuffney, C. Feng, B. M. Webb, C. Jeon, M. Spilatro, S. Bucht, C. Dorrer, and J. Bromage, "Effect of the Pump Beam Profile and Wavefront on the Amplified Signal Wavefront in Optical Parametric Amplifiers," Opt. Express **30**, 12,995 (2022).

A. Bose, J. Peebles, C. A. Walsh, J. A. Frenje, N. V. Kabadi, P. J. Adrian, G. D. Sutcliffe, M. Gatu Johnson, C. A. Frank, J. R. Davies, R. Betti, V. Yu. Glebov, F. J. Marshall, S. P. Regan, C. Stoeckl, E. M. Campbell, H. Sio, J. Moody, A. Crilly, B. D. Appelbe, J. P. Chittenden, S. Atzeni, F. Barbato, A. Forte, C. K. Li, F. H. Séguin, and R. D. Petrasso, "Effect of Strongly Magnetized Electrons and Ions on Heat Flow and Symmetry of Inertial Fusion Implosions," Phys. Rev. Lett. **128**, 195002 (2022).

A. F. A. Bott, L. Chen, P. Tzeferacos, C. A. J. Palmer, A. R. Bell, R. Bingham, A. Birkel, D. H. Froula, J. Katz, M. W. Kunz, C.-K. Li, H.-S. Park, R. Petrasso, J. S. Ross, B. Reville, D. Ryu, F. H. Séguin, T. G. White, A. A. Schekochihin, D. Q. Lamb, and G. Gregori, "Insensitivity of a Turbulent Laser-Plasma Dynamo to Initial Conditions," Matter Radiat. Extremes **7**, 046901 (2022).

S. J. Burns, J. R. Rygg, D. Polsin, B. Henderson, M. Marshall, S. Zhang, S. X. Hu, and G. Collins, "Planar, Longitudinal, Compressive Waves in Solids: Thermodynamics and Uniaxial Strain Restrictions," J. Appl. Phys. **131**, 215904 (2022).

D. A. Chin, J. J. Ruby, P. M. Nilson, D. T. Bishel, F. Coppari, Y. Ping, A. L. Coleman, R. S. Craxton, J. R. Rygg, and G. W. Collins, "Emission Phases of Implosion Sources for X-Ray Absorption Fine Structure Spectroscopy," Phys. Plasmas **29**, 052702 (2022).

A. Diaw, S. J. Coleman, N. M. Cook, J. P. Edelen, E. C. Hansen, and P. Tzeferacos, "Impact of Electron Transport Models on Capillary Discharge Plasmas," Phys. Plasmas **29**, 063101 (2022).

C. Dorrer and J. L. Shaw, "Single-Shot Cross-Correlation of Counter-Propagating, Short Optical Pulses Using Random Quasi-Phase-Matching," Opt. Express **30**, 16,677 (2022).

R. K. Follett, H. Wen, D. H. Froula, D. Turnbull, and J. P. Palastro, "Independent-Hot-Spot Approach to Multibeam Laser-Plasma Instabilities," Phys. Rev. E **105**, L063201 (2022).

G. W. Jenkins, C. Feng, and J. Bromage, "Simultaneous Contrast Improvement and Temporal Compression Using Divided-Pulse Nonlinear Compression," Opt. Express **30**, 13,968 (2022).

D. Kim, R. F. Smith, I. K. Ocampo, F. Coppari, M. C. Marshall, M. K. Ginnane, J. K. Wicks, S. J. Tracy, M. Millot, A. Lazicki, J. R. Rygg, J. H. Eggert, and T. S. Duffy, "Structure and Density of Silicon Carbide to 1.5 TPa and Implications for Extrasolar Planets," Nat. Commun. **13**, 2260 (2022).

Y.-J. Kim, B. Militzer, B. Boates, S. Bonev, P. M. Celliers, G. W. Collins, K. P. Driver, D. E. Fratanduono, S. Hamel, R. Jeanloz, J. R. Rygg, D. C. Swift, J. H. Eggert, and M. Millot, "Evidence for Dissociation and Ionization in Shock Compressed Nitrogen to 800 GPa," Phys. Rev. Lett. **129**, 015701(2022).

R. K. Kirkwood, P. L. Poole, D. H. Kalantar, T. D. Chapman, S. C. Wilks, M. R. Edwards, D. P. Turnbull, P. Michel, L. Divol, N. J. Fisch, P. Norreys, W. Rozmus, J. Bude, B. E. Blue, K. B. Fournier, B. M. Van Wonterghem, and A. MacKinnon, "Production of High Fluence Laser Beams Using Ion Wave Plasma Optics," Appl. Phys. Lett. **120**, 200501 (2022).

T. Z. Kosc, H. Huang, T. J. Kessler, and S. G. Demos, "Angular Dependence of the Transverse Raman Scattering in KDP and DKDP in Geometries Suitable for Beam Polarization Control," Opt. Express **30**, 12,918 (2022).

L. S. Leal, A. V. Maximov, E. C. Hansen, J. R. Davies, D. H. Barnak, J. L. Peebles, K. M. Woo, P. V. Heuer, A. B. Sefkow, and R. Betti, "Effect of Laser Preheat in Magnetized Liner Inertial Fusion at OMEGA," Phys. Plasmas **29**, 042703 (2022).

S. Malko, W. Cayzac, V. Ospina-Bohórquez, K. Bhutwala, M. Bailly-Grandvaux, C. McGuffey, R. Fedosejevs, X. Vaisseau, An. Tauschwitz, J. I. Apiñaniz, D. De Luis, G. Gatti, M. Huault, J. A. Perez Hernandez, S. X. Hu, A. J. White, L. A. Collins, K. Nichols, P. Neumayer, G. Faussurier, J. Vorberger, G. Prestopino, C. Verona, J. J. Santos, D. Batani, F. N. Beg, L. Roso, and L. Volpe, "Proton Stopping Measurements at Low Velocity in Warm Dense Carbon," Nat. Commun. **13**, 2893 (2022).

O. M. Mannion, A. J. Crilly, C. J. Forrest, B. D. Appelbe, R. Betti, V. Yu. Glebov, V. Gopalaswamy, J. P. Knauer, Z. L. Mohamed, C. Stoeckl, J. P. Chittenden, and S. P. Regan, "Measurements of the Temperature and Velocity of the Dense Fuel Layer in Inertial Confinement Fusion Experiments," Phys. Rev. E **105**, 055205 (2022).

K. L. Marshall, K. R. P. Kafka, N. D. Urban, J. U. Wallace, and S. G. Demos, "Multiparameter Laser Performance Characterization of Liquid Crystals for Polarization Control Devices in the Nanosecond Regime," Sci. Rep. **12**, 10969 (2022).

J. Musgrave and J. Bromage, "Impact of the Optical Parametric Amplification Phase on Laser Pulse Compression," Appl. Opt. **61**, 3838 (2022).

R. W. Paddock, H. Martin, R. T. Ruskov, R. H. H. Scott, W. Garbett, B. M. Haines, A. B. Zylstra, E. M. Campbell, T. J. B. Collins, R. S. Craxton, C. A. Thomas, V. N. Goncharov, R. Aboushelbaya, Q. S. Feng, M. W. von der Leyen, I. Ouatu, B. T. Spiers, R. Timmis, R. H. W. Wang, and P. A. Norreys, "Pathways Towards Break Even for Low Convergence Ratio Direct-Drive Inertial Confinement Fusion," J. Plasma Phys. **88**, 905880314 (2022).

D. N. Polsin, A. Lazicki, X. Gong, S. J. Burns, F. Coppari, L. E. Hansen, B. J. Henderson, M. F. Huff, M. I. McMahon, M. Millot, R. Paul, R. F. Smith, J. H. Eggert, G. W. Collins, and J. R. Rygg, "Structural Complexity in Ramp-Compressed Sodium to 480 GPa," Nat. Commun. **13**, 2534 (2022).

D. Ramsey, B. Malaca, A. Di Piazza, M. Formanek, P. Franke, D. H. Froula, M. Pardal, T. T. Simpson, J. Vieira, K. Weichman, and J. P. Palastro, "Nonlinear Thomson Scattering with Ponderomotive Control," Phys. Rev. E **105**, 065201 (2022).

G. F. Swadling, C. Bruulsema, W. Rozmus, and J. Katz, "Quantitative Assessment of Fitting Errors Associated with Streak Camera Noise in Thomson Scattering Data Analysis," Rev. Sci. Instrum. **93**, 043503 (2022).

K. Weichman, A. P. L. Robinson, M. Murakami, J. J. Santos, S. Fujioka, T. Toncian, J. P. Palastro, and A. V. Arefiev, "Progress in Relativistic Laser–Plasma Interaction with Kilotesla-Level Applied Magnetic Fields," Phys. Plasmas **29**, 053104 (2022) (invited).

H. Wen, C. Ren, E. C. Hansen, D. Michta, Y. Zhang, S. Langendorf, and P. Tzeferacos, "Particle-in-Cell Modeling of Plasma Jet Merging in the Large-Hall-Parameter Regime," Phys. Plasmas **29**, 062706 (2022).

J. Zhang, W. R. Donaldson, and G. P. Agrawal, "Temporal Reflection of an Optical Pulse from a Short Soliton: Impact of Raman Scattering," J. Opt. Soc. Am. B **39**, 1950 (2022).

Forthcoming Publications

A. F. Antoniadis, D. Drikakis, P. S. Farmakis, L. Fu, I. Kokkinakis, X. Nogueira, P. A. S. F. Silva, M. Skote, V. Titarev, and P. Tsoutsanis, "UCNS3D: An Open-Source High-Order Finite-Volume Unstructured CFD Solver," to be published in Computer Physics Communications.

Z. Chen, S. X. Hu, and N. P. Bigelow, "Imprinting a Three-Dimensional Skyrmion in a Bose–Einstein Condensate Via a Raman Process," to be published in the Journal of Low Temperature Physics.

V. Gopalaswamy, R. Betti, P. B. Radha, A. J. Crilly, K. M. Woo, A. Lees, C. Thomas, I. V. Igumenshchev, S. C. Miller, J. P. Knauer, C. Stoeckl, C. J. Forrest, O. M. Mannion, Z. L. Mohamed, H. G. Rinderknecht, and P. V. Heuer, "Analysis of Limited Coverage Effects on Areal Density Measurements in Inertial Confinement Fusion Implosions," to be published in Physics of Plasmas.

S. S. Harilal, M. C. Phillips, D. H. Froula, K. K. Anoop, R. C. Issac, and F. N. Beg, "Optical Diagnostics of Laser-Produced Plasmas," to be published in the Reviews of Modern Physics.

P. V. Heuer, L. S. Leal, J. R. Davies, E. C. Hansen, D. H. Barnak, J. L. Peebles, F. García-Rubio, B. Pollock, J. Moody, A. Birkel, and F. H. Séguin, "Diagnosing Magnetic Fields in

Cylindrical Implosions with Oblique Proton Radiography," to be published in Physics of Plasmas.

M. P. Jeske, W. Zhang, and M. Anthamatten "Two-Photon Printing of Shape-Memory Microstructures and Metasurfaces via Radical-Mediated Thiol-Vinyl Hydrothiolation," to be published in Advanced Materials Technologies.

K. R. P. Kafka, T. Z. Kosc, and S. G. Demos, "Methods and Apparatus for Comprehensive Characterization of Performance Attributes and Damage Thresholds of Ultrafast Laser Optics," to be published in Optical Engineering.

H. Poole, D. Cao, R. Epstein, I. Golovkin, T. Walton, S. X. Hu, M. Kasim, S. M. Vinko, J. R. Rygg, V. N. Goncharov, G. Gregori, and S. P. Regan, "A Case Study of Using X-Ray Thomson Scattering to Diagnose the In-Flight Plasma Condition of DT Cryogenic Implosions," to be published in Physics of Plasmas.

A. K. Schwemmlein, C. Stoeckl, C. J. Forrest, W. T. Shmayda, S. P. Regan, W. U. Schröder, "First Demonstration of a Triton Beam Using Target Normal Sheath Acceleration," to be published in Nuclear Instruments and Methods in Physics Research B.

R. C. Shah, D. Cao, L. Aghaian, B. Bachmann, R. Betti, E. M. Campbell, R. Epstein, C. J. Forrest, A. Forsman, V. Yu. Glebov, V. N. Goncharov, V. Gopalaswamy, D. R. Harding, S. X. Hu, I. V. Igumenshchev, R. T. Janezic, L. Keaty, J. P. Knauer, D. Kobs, A. Lees, O. M. Mannion, Z. L. Mohamed, D. Patel, M. J. Rosenberg, W. T. Shmayda, C. Stoeckl, W. Theobald, C. A. Thomas, P. Volegov, K. M. Woo, and S. P. Regan, "Bound on Hot-Spot Mix in High-Velocity, High-Adiabat Direct-Drive Cryogenic Implosions Based on Comparison of Absolute X-Ray and Neutron Yields," to be published in Physical Review E.

S. Singh, A. L. Coleman, S. Zhang, F. Coppari, M. G. Gorman, R. F. Smith, J. H. Briggs, and D. E. Fratanduono, "Quantitative Analysis of Diffraction by Liquids Using a Pink-Spectrum X-Ray Source," to be published in the Journal of Synchrotron Radiation.

R. Sobolewski, "Optical Detectors and Sensors," to be published in the Handbook of Superconducting Materials.

D. Turnbull, J. Katz, D. E. Hinkel, P. Michel, T. Chapman, L. Divol, E. Kur, S. MacLaren, A. L. Milder, M. Rosen, A. Shvydky, G. B. Zimmerman, and D. H. Froula, "Beam Spray Thresholds in ICF-Relevant Plasmas," to be published in Physical Review Letters.

N. D. Urban, K. R. P. Kafka, K. L. Marshall, and S. G. Demos, "Laser-Induced Damage Characteristics of Fused Silica Surfaces Polished to Different Depths Using Fluid Jet Polishing," to be published in Optical Engineering.

K. M. Woo, R. Betti, C. A. Thomas, C. Stoeckl, K. Churnetski, C. J. Forrest, Z. L. Mohamed, B. Zirps, S. P. Regan, T. J. B. Collins, W. Theobald, R. C. Shah, O. M. Mannion, D. Patel, D. Cao, J. P. Knauer, V. Yu. Glebov, V. N. Goncharov, P. B. Radha, H. G. Rinderknecht, R. Epstein, V. Gopalaswamy, F. J. Marshall, S. T. Ivancic, and E. M. Campbell, "Analysis of Core Asymmetries in Inertial Confinement Fusion Implosions Using Three-Dimensional Hot-Spot Reconstruction," to be published in Physics of Plasmas.

D. Zhang, J. Li, J. Xin, R. Yan, Z. Wan, H. Zhang, and J. Zheng, "Self-Generated Magnetic Field in Ablative Rayleigh–Taylor Instability," to be published in Physics of Plasmas.

Conference Presentations

The following presentations were made at the 2022 Panchanatan Visit, Rochester, NY, 11 April 2022:

C. Deeney, "An Overview of the Laboratory for Laser Energetics: Always 'Reaching for the Brightest Light.' "

V. Gopalaswamy, "Data-Driven Experimental Design at LLE."

E. M. Hill, "LLE is a Word Leader for Designing, Innovating, and Constructing State-of-the-Art Lasers for a Wide Range of Scientific Applications for Ourselves and the Broader Scientific Community."

M. F. Huff, "Measuring Sound Speed in Shocked Iron."

J. Katz, "Diagnostic Development and Advanced Instrumentation for Fundamental Physics."

Z. K. Sprowal, L. E. Hansen, M. F. Huff, D. N. Polsin, T. R. Boehly, J. R. Rygg, G. W. Collins, and D. G. Hicks, "Accessing High-Density States in D_2 Using Double Shocks."

M. S. Wei, "User Community."

C. A. Williams, "Convergence Research in Inertial Confinement Fusion."

J. D. Zuegel, "Laser Materials Technology Division and Major Projects," presented at the NNSA–OES Visit, virtual, 12 April 2022.

R. B. Spielman, "The Design of Self-Magnetically Insulated Transmission Lines for a 10-MA Intermediate-Scale Facility," presented at the Cornell University Seminar, Cornell, NY, 13 April 2022.

J. Bromage, S.-W. Bahk, M. Bedzyk, I. A. Begishev, S. Bucht, C. Dorrer, C. Feng, B. N. Hoffman, C. Jeon, C. Mileham, J. B. Oliver, R. G. Roides, E. M. Schiesser, K. Shaughnessy, M. J. Shoup III, M. Spilatro, B. Webb, D. Weiner, and J. D. Zuegel, "Development of Ultra-Intense OPCPA Technologies on the MTW-OPAL System," presented at the 11th Advanced Lasers and Photon Sources, Yokohama, Japan, 18–21 April 2022 (invited).

S. X. Hu, P. M. Nilson, D. T. Bishel, D. A. Chin, V. V. Karasiev, D. I. Mihaylov, N. R. Shaffer, S. Zhang, V. Recoules, N. Brouwer, M. Torrent, I. E. Golovkin, M. Gu, T. Walton, and S. B. Hansen, "Probing Atomic Physics at Extreme Conditions," presented at the International Conference on High-Energy-Density Sciences, Yokohama, Japan, 18–22 April 2022 (invited).

J. D. Zuegel, J. Bromage, D. H. Froula, E. M. Hill, J. P. Palastro, J. C. Puth, H. G. Rinderknecht, J. L. Shaw, C. J. Forrest, and L. J. Waxer, "Proposed EP-OPAL Laser Facility," presented at the MP3 Workshop, Paris, France, 20–22 April 2022.

C. Deeney, "Pulsed-Power Research at LLE," presented at the ZNetUS Workshop, virtual, 21–22 April 2022.

The following presentations were made at the 2022 ARPA-E Fusion Programs Annual Meeting, San Francisco, CA, 26–27 April 2022:

J. R. Davies, H. Berger, C. J. Forrest, V. Yu. Glebov, H. McClow, M. Sharpe, and W. T. Shmayda, "The LLE Diagnostic Resource Team for Innovative Fusion Concepts."

V. N. Goncharov, I. V. Igumenshchev, W. Trickey, R. K. Follett, N. Shaffer, A. Pineau, Y. Lawrence, M. Tobin, W. Meier, S. Woodruff, C. Dorrer, and J. D. Zuegel, "Advanced Inertial Fusion Energy Target Designs with Next-Generation Laser Technologies."

P. Tzeferacos, A. Sefkow, C. Ren, R. Betti, J. R. Davies, H. Wen, J. G. Shaw, E. C. Hansen, D. Michta, F. García-Rubio, and K. M. Woo, "A Simulation Resource Team for Innovative Fusion Concepts in the BETHE Program."

The following presentations were made at the 2022 Omega Laser Facility Users Group, Rochester, NY, 27–29 April 2022:

A. Armstrong, A. Reyes, M. B. P. Adams, P. Farmakis, E. C. Hansen, Y. Lu, D. Michta, K. Moczulski, D. Q Lamb, and P. Tzeferacos, "Implementation and Verification of Spitzer Viscosity in the *FLASH* Code."

D. H. Barnak, "Self-Optimizing Savitzky–Golay Filter for Generalized Signal Denoising."

D. H. Barnak, R. Betti, V. Gopalaswamy, A. Lees, and A. Shvydky, "Numerical Simulations of the VISAR Diagnostic."

D. H. Barnak, J. R. Davies, J. P. Knauer, and P. M. Kozlowski, "*FIDUCIA*: A New User's Course into the Wonderful World of Cubic Spline Unfolding."

G. Bruhaug, H. G. Rinderknecht, M. S. Wei, B. Brannon, D. Guy, R. Peck, N. Landis, G. Brent, R. Fairbanks, C. McAtee, T. Walker, T. Buczek, M. Krieger, M. Romanofsky, Y. E, K. Garriga, X. C. Zhang, G. W. Collins, and J. R. Rygg, "High-Power, High-Energy THz Generation Using Joule- and Kilojoule-Class Lasers."

C. Deeney, "The Next Cooperative Agreement: FY24–FY28."

P. Farmakis, M. McMullan, A. Reyes, J. Laune, M. B. P. Adams, A. Armstrong, E. C. Hansen, Y. Lu, D. Michta,

K. Moczulski, D. Lamb, and P. Tzeferacos, "Expanding the Tabulated Equationof-State Implementations in the *FLASH* Code for the *SESAME* Database."

D. H. Froula, "Fourth-Generation Laser for Ultra-Broadband Experiments."

E. C. Hansen, P. Farmakis, D. Michta, C. Ren, A. C. Reyes, H. Wen, S. Langendorf, and P. Tzeferacos, "Simulating the Plasma Liner Experiment (PLX) with the *FLASH* Code."

P. V. Heuer, J. R. Davies, D. Stanczak, E. Everson, and N. Murphy, "Synthetic Diagnostics for High-Energy-Density Physics in *PlasmaPy*."

S. T. Ivancic, "Gas-Jet System on OMEGA and OMEGA EP."

T. J. Kessler and M. Romo-Gonzalez, "Inclusion, Diversity, and Equity at the Laboratory for Laser Energetics."

Y. Lu, S. Feister, J. Meinecke, F. Miniati, G. Gregori, A. Bott, A. Reyes, E. C. Hansen, J. T. Laune, B. Reville, J. S. Ross, D. Q. Lamb, and P. Tzeferacos, "Numerical Modeling of Laser-Driven Plasma Experiments Aiming to Study Turbulent Dynamo and Thermal Conduction at the National Ignition Facility."

D. Michta, P. Tzeferacos, S. Bolanos, and M. Manuel, "*FLASH* Simulations of the Magnetized Quasi-Parallel Collisionless Shock Experiments on OMEGA EP."

K. Moczulski, A. Reyes, M. B. P. Adams, A. Armstrong, P. Farmakis, E. C. Hansen, Y. Lu, D. Michta, D. Q. Lamb, and P. Tzeferacos, "Implementation and Verification of LC Circuit for *Z*-Pinch *FLASH* Simulations."

S. F. B. Morse, "Omega Facility OLUG 2022 Update: Progress on Recommendations and Items of General Interest."

S. F. B. Morse, "The Sustainment Plan for the Omega Laser Facility."

J. L. Peebles, "Generating Magnetic Fields Using MIFEDS on Your Campaign at OMEGA/OMEGA EP."

A. Reyes, M. B. P. Adams, A. Armstrong, K. Moczulski, P. Farmakis, E. C. Hansen, Y. Lu, D. Michta, J. Grove, and P. Tzeferacos, "Volume-of-Fluid Representation of Multifluid Compressible Hydrodynamics in the *FLASH* Code."

P. Tzeferacos, "Big Lasers and Big Computers: The Flash Center for Computational Science and the *FLASH* Code at UR."

A. Bowman, M. Burns, A. Poudel, S. Zhai, S. Dwarkadas, A. B. Sefkow, and S. Pai, "Cross-Beam Energy Transfer on Graphics Processing Units," presented at Senior Design Day, Rochester, NY, 29 April 2022.

D. Mihaylov, "Improving the Accuracy of Density Functional Theory Simulations of Warm Dense Matter by Including Exchange-Correlation Thermal Effects," presented at the Center for Advanced Systems Understanding Seminar, virtual, 3 May 2022.

The following presentations were made at the 17th Direct Drive and Fast Ignition Workshop, Madrid, Spain, 3–5 May 2022:

E. M. Campbell, "Perspective on Inertial Fusion Energy."

L. Ceurvorst, W. Theobald, M. J. Rosenberg, P. B. Radha, S. P. Regan, C. Stoeckl, R. Betti, K. S. Anderson, J. A. Marozas, V. N. Goncharov, E. M. Campbell, C. M. Shuldberg, R. W. Luo, W. Sweet, L. Aghaiain, D. N. Kaczala, B. Bachmann, T. Döppner, M. Hohenberger, K. Glize, R. H. H. Scott, and A. Colaïtis, "Laser-Direct-Drive Energy-Coupling Experiments Using Solid Spheres at the National Ignition Facility."

V. N. Goncharov, W. Trickey, I. V. Igumenshchev, N. Shaffer, Y. Lawrence, S. Atzeni, and L. Savino, "Advanced Target Designs for Laser-Direct-Drive Inertial Confinement Fusion."

S. X. Hu, L. Ceurvorst, J. L. Peebles, V. N. Goncharov, Y.-F. Lu, A. Pineau, G. Duchateau, K. R. P. Kafka, S. G. Demos, W. Theobald, S. P. Regan, A. Shvydky, T. J. B. Collins, V. V. Karasiev, S. Zhang, D. R. Harding, R. C. Shah, E. M. Campbell, and C. Deeney, "Review on Laser Imprint for Direct-Drive Inertial Confinement Fusion Implosions."

S. P. Regan, V. N. Goncharov, E. M. Campbell, R. Betti, P. Adrian, K. S. Anderson, B. Appelbe, J. Baltazar, D. H. Barnak, J. Bates, K. A. Bauer, R. Boni, M. J. Bonino, D. Cao, A. Colaïtis, D. Canning, K. Churnetski, T. J. B. Collins, G. W.

Collins, A. J. Crilly, J. R. Davies, S. G. Demos, C. Dorrer, R. F. Earley, R. Epstein, M. Farrell, R. K. Follett, C. J. Forrest, J. A. Frenje, D. H. Froula, M. Gatu-Johnson, V. Yu. Glebov, V. Gopalaswamy, A. M. Hansen, D. R. Harding, P. V. Heuer, E. M. Hill, S. X. Hu, H. Huang, J. Hund, I. V. Igumenshchev, S. T. Ivancic, D. W. Jacobs-Perkins, R. T. Janezic, M. Karasik, J. Katz, J. P. Knauer, B. Kruschwitz, J. Kunimune, M. Labuzeta, A. Lees, O. M. Mannion, J. A. Marozas, P. W. McKenty, S. F. B. Morse, P. M. Nilson, J. P. Palastro, D. Patel, J. L. Peebles, P. B. Radha, H. G. Rinderknecht, M. J. Rosenberg, J. R. Rygg, S. Sampat, T. C. Sangster, R. C. Shah, M. Sharpe, W. T. Shmayda, M. J. Shoup III, C. Shuldberg, A. Shvydky, A. A. Solodov, Z. K. Sprowal, C. Sorce, A. Sorce, C. Stoeckl, C. A. Thomas, W. Theobald, D. Turnbull, L. J. Waxer, M. D. Wittman, K. M. Woo, and J. D. Zuegel, "Accomplishments of the 100-Gbar Campaign on OMEGA."

R. C. Shah, S. X. Hu, I. V. Igumenshchev, J. Baltazar, D. Cao, C. J. Forrest, V. N. Goncharov, V. Gopalaswamy, D. Patel, W. Theobald, S. P. Regan, and F. Philippe, "Anomalous X-Ray Emission at Early Stages of Hot-Spot Formation in Deuterium–Tritium Cryogenic Implosions."

W. Trickey, V. N. Goncharov, E. M. Campbell, Y. Lawrence, M. J. Rosenberg, N. Shaffer, W. Theobald, R. C. Shah, A. Shvydky, I. V. Igumenshchev, A. Colaïtis, S. Atzeni, and L. Savino, "Multidimensional Modeling of Low-Mode Perturbations in the Dynamic-Shell Inertial Confinement Fusion Design."

The following presentations were made at the 2022 Center for Matter at Atomic Pressures, Rochester, NY, 5–6 May 2022:

D. Bishel, P. M. Nilson, D. A. Chin, E. Smith, S. X. Hu, V. V. Karasiev, J. R. Rygg, G. W. Collins, J. J. Ruby, and E. V. Marley, "Interrogating the Atomic Structure of Dense Plasmas by X-Ray Absorption Spectroscopy of Implosion Shells."

D. A. Chin, P. M. Nilson, D. T. Bishel, R. Paul, E. Smith, X. Gong, M. K. Ginnane, B. J. Henderson, D. N. Polsin, S. X. Hu, J. R. Rygg, G. W. Collins, D. Trail, A. Amouretti, M. Harmand, O. Mathon, R. Torchio, J. J. Ruby, F. Coppari, A. Coleman, and Y. Ping, "X-Ray Fine Absorption Fine Structure Spectroscopy Measurements of High-Energy-Density Matter."

Z. K. Sprowal, L. E. Hansen, M. F. Huff, D. N. Polsin, D. G. Hicks, T. R. Boehly, J. R. Rygg, and G. W. Collins, "Accessing High-Density States in D_2 Using Double Shock."

S. Zhang, "Isentrope and Equation of State of Solid Hydrogen."

C. Jeon, "Smart Cities and Lasers: Connecting the Dots," presented at the Han Yang University Seminar, virtual, 6 May 2022.

The following presentations were made at the 2022 Materials Research Society Spring Meeting, Honolulu, HI, 8–25 May 2022:

S. M. Fess, D. R. Harding, M. J. Bonino, R. F. Earley, P. Fan, X. Huang, Y.-F. Lu, S. P. Regan, and E. M. Campbell, "Fabrication of Shells and Foams via Two-Photon Polymerization for Laser-Fusion Experiments."

D. R. Harding, S. M. Fess, M. Bonino, R. F. Earley, Y.-F. Lu, X. Huang, P. Fan, S. P. Regan, and E. M. Campbell, "Multiphoton Applications in Laser Fusion Research: From Printing Fusion-Fuel Targets with Sub-150-nm Features to Acquiring Three-Dimensional Structural and Elemental Information of the Target."

M. P. Jeske and M. Anthamatten, "Thermally Responsive Resins for Free-Radical and Base-Catalyzed Two-Photon Polymerization."

P. Tzeferacos, "*FLASH* for *Z*-Pinch Experiments and Extended MHD," presented at the 2022 Center for Matter Under Extreme Conditions Review, San Diego, CA, 10–11 May 2022.

The following presentations were made at the 24th High-Temperature Plasma Diagnostic Conference, Rochester, NY, 15–19 May 2022:

J. Baltazar, R. Betti, K. Churnetski, V. Gopalaswamy, J. P. Knauer, D. Patel, H. G. Rinderknecht, R. C. Shah, C. Stoeckl, C. A. Willliams, and S. P. Regan, "Diagnosing Low-Mode ($\ell < 6$) and Mid-Mode ($6 \leq \ell \leq 20$) Asymmetries in the

Explosion Phase of Laser-Direct-Drive Deuterium–Tritium Cryogenic Implosions on OMEGA."

G. Bruhaug, H. G. Rinderknecht, M. S. Wei, B. Brannon, D. Guy, R. G. Peck, N. Landis, G. Brent, R. Fairbanks, C. McAtee, T. Walker, T. Buczek, M. Krieger, M. Romanofsky, Y. E, K. Garriga, X. C. Zhang, G. W. Collins, and J. R. Rygg, "Development of a Hardened THz Energy Meter for Use on the Kilojoule-Scale, Short-Pulse OMEGA EP Laser."

L. Ceurvorst, W. Theobald, M. J. Rosenberg, P. B. Radha, S. P. Regan, C. Stoeckl, R. Betti, K. S. Anderson, J. A. Marozas, V. N. Goncharov, E. M. Campbell, C. M. Shuldberg, R. W. Luo, W. Sweet, L. Aghaian, D. N. Kaczala, B. Bachmann, T. Döppner, M. Hohenberger, K. Glize, R. H. H. Scott, and A. Colaïtis, "Development of an X-Ray Radiography Platform to Study Laser-Direct-Drive Energy Coupling at the National Ignition Facility."

J. Cheng, G. Chen, D. Chakraborty, S. Kutcher, J. Wen, H. Chen, S. Trivedi, and R. Sobolewski, "(Cd,Mg)Te for Picosecond Response Optical to X-Ray Radiation Detectors."

K. Churnetski, K. M. Woo, W. Theobald, P. B. Radha, R. Betti, V. Gopalaswamy, I. V. Igumenshchev, S. T. Ivancic, M. Michalko, R. C. Shah, C. Stoeckl, C. A. Thomas, and S. P. Regan, "Three-Dimensional Hot-Spot X-Ray Emission Tomography from Cryogenic Deuterium–Tritium Direct-Drive Implosions on OMEGA."

R. Cuffney, J. Shamlian, M. Sharpe, T. Lewis, M. J. Shoup III, J. Bromage, B. Golick, N. Palmer, A. Golod, B. Hatch, and M. Miller, "4ω Fiducial Generator: Provides Optical Timing Reference Marks for Streak Cameras."

D. H. Edgell, J. Katz, R. Raimondi, D. Turnbull, and D. H. Froula, "Scattered-Light Uniformity Imager for Diagnosing Laser Absorption Asymmetries on OMEGA."

T. Filkins, M. J. Rosenberg, R. Bahr, J. Katz, and S. T. Ivancic, "Calibration of the Sub-Aperture Backscatter System on OMEGA EP."

C. J. Forrest, R. Betti, J. P. Knauer, V. Yu. Glebov, V. Gopalaswamy, O. M. Mannion, Z. L. Mohamed, P. B. Radha, S. P. Regan, A. Schwemmlein, C. Stoeckl, W. Theobald, J. A. Frenje, M. Gatu Johnson, B. Appelbe, and A. J. Crilly, "Measurements of Low-Mode Asymmetries in Areal Density of Laser-Direct-Drive DT Cryogenic Implosions on OMEGA Using Neutron Spectroscopy" (invited).

V. Yu. Glebov, C. J. Forrest, J. Kendrick, J. P. Knauer, H. McClow, S. P. Regan, C. Stoeckl, B. Stanley, W. Theobald, and O. M. Mannion, "A New Neutron Time-of-Flight Detector for D_2 Yield and Ion-Temperature Measurements on OMEGA."

D. Haberberger, A. Shvydky, and D. H. Froula, "Fresnel Zone Plate Calculations for the Application to Laser-Plasma Experiments."

P. V. Heuer, D. Stanczak, E. T. Everson, N. A. Murphy, and J. R. Davies, "Open-Source Analysis Software for High-Temperature Plasma Diagnostics."

S. T. Ivancic, W. Theobald, K. Churnetski, M. Michalko, D. Willistein, W. Bittle, S. P. Regan, A. Carpenter, C. Trosseille, J. D. Kilkenny, A. Raymond, J. D. Hares, A. K. L. Dymoke-Bradshaw, G. Rochau, and D. Garand "Design of the High-Yield Time-Gated X-Ray Hot-Spot Imager (XRHSI) for OMEGA."

T. R. Joshi, R. C. Shah, W. Theobald, K. Churnetski, P. B. Radha, D. Cao, C. A. Thomas, J. Baltazar, and S. P. Regan, "Diagnosis of the Imploding Shell Asymmetry in Polar-Direct-Drive DT Cryogenic Target Implosions on OMEGA."

J. Katz, D. Turnbull, S. T. Ivancic, A. L. Milder, and D. H. Froula, "Measurement of Laser Absorption in Underdense Plasmas Using Near-Field Imaging of the Incident and Transmitted Beams."

J. P. Knauer, C. J. Forrest, V. Gopalaswamy, and Z. L. Mohamed, "Normalized Time Axis for Neutron Time-of-Flight Analysis."

S. Kostick, M. J. Rosenberg, W. Theobald, J. Katz, N. Lemos, E. Tubman, J. S. Ross, N. Butler, G. Swadling, R. Sommers, J. D. Moody, R. S. Craxton, A. Sharma, and S. P. Regan, "Assessment of the Calibration of the Scattered-Light Time-History Diagnostic at the National Ignition Facility."

H. McClow, H. Berger, J. R. Davies, C. J. Forrest, G. Gates, S. T. Ivancic, J. Katz, J. Ruby, A. Sorce, and W. Theobald, "First Measurements with a Single-Hit Neutron Spectrometer."

S. F. Nwabunwanne and W. R. Donaldson, "Tunable, Picosecond AlGaN UV Photodiodes."

H. Poole, M. K. Ginnane, J. Topp-Mugglestone, R. Saha, D. N. Polsin, G. W. Collins, S. X. Hu, T. White, S. P. Regan,

G. Gregori, and J. R. Rygg, "Measurements of Warm-Dense-Matter Silicon Based on Angularly and Spectrally Dispersed X-Ray Scattering."

H. G. Rinderknecht, P. V. Heuer, V. Gopalaswamy, J. P. Knauer, C. A. Williams, W. Theobald, R. Fairbanks, B. Brannon, V. Kobilansky, R. Peck, J. Armstrong, M. Weisbeck, J. Brown, L. Ceurvorst, P. B. Radha, S. P. Regan, J. Kunimune, P. Adrian, M. Gatu Johnson, J. A. Frenje, F. Séguin, A. J. Crilly, B. Appelbe, and B. Bachmann, "A Knock-On Deuteron Imager for Measurements of Fuel and Hot-Spot Asymmetry in Direct-Drive Inertial Confinement Fusion Implosions" (invited).

M. Romo-Gonzalez and R. Boni, "Free-Standing Thin Membrane Zero *B*-Integral Beam Splitters."

B. Stanley, C. J. Forrest, and S. T. Ivancic, "Nuclear Activation Analysis of Zirconium-90 Isomeric and Ground-State Reactions at the Omega Laser Facility."

C. Stoeckl, D. Cao, L. Ceurvorst, A. Kalb, J. Kwiatkowski, A. Shvydky, and W. Theobald, "Beam Pointing Verification Using X-Ray Pinhole Cameras on the 60-Beam OMEGA Laser."

The following presentations were made at CLEO 2022, San Jose, CA, 15–20 May 2022:

C. Dorrer and J. L. Shaw, "Single-Shot Cross-Correlation of Counter-Propagating Pulses in a Disordered Nonlinear Crystal."

C. Dorrer and M. A. Spilatro, "Spectral and Temporal Shaping of Spectrally Incoherent UV Pulses by Sum-Frequency Generation."

G. W. Jenkins, C. Feng, and J. Bromage, "Energy Scaling Beyond Gas-Ionization Thresholds with Divided-Pulse Nonlinear Compression."

J. P. Palastro, "Laser–Plasma Interactions Driven by Flying Focus Pulses."

J. Zhang, W. R. Donaldson, and G. P. Agrawal, "Theory and Applications of Temporal Reflection in a Dispersive Medium."

The following presentations were made at the 49th International Conference on Plasma Science, Seattle, WA, 22–26 May 2022:

C. Deeney, E. M. Campbell, V. N. Goncharov, R. Betti, J. D. Zuegel, S. P. Regan, G. W. Collins, S. F. B. Morse, C. Sorce, D. H. Froula, and M. S. Wei, "Laboratory for Laser Energetics: Progress in Science and Technology."

J. Katz, R. Boni, A. L. Milder, D. Nelson, K. Daub, and D. H. Froula, "A High-Numerical-Aperture, Angularly Resolved Thomson-Scattering Spectrometer" (invited).

V. N. Goncharov, W. Trickey, N. Shaffer, A. Peneau, I. V. Igumenshchev, R. K. Follett, T. J. B. Collins, C. Dorrer, J. D. Zuegel, M. Tobin, W. Meier, and Y. Lawrence, "Advanced Inertial Fusion Energy Target Designs with Next-Generation Laser Technologies," presented at the ARPA-E Summit, Denver, CO, 23–25 May 2022.

V. N. Goncharov, W. Trickey, I. V. Igumenshchev, N. Shaffer, T. J. B. Collins, R. K. Follett, C. Stoeckl, R. C. Shah, C. Dorrer, J. D. Zuegel, D. R. Harding, S. Fess, E. M. Campbell, C. Deeney, S. Atzeni, L. Savino, F. Barbato, and A. Colaïtis, "Direct-Drive Designs and Experiments on OMEGA," presented at the EUROfusion Science Meeting, virtual, 27 May 2022.

The following presentations were made at the 50th Anomalous Absorption Conference, Skytop, PA, 5–10 June 2022:

Z. Barfield, J. L. Peebles, P. Tzeferacos, D. Mastrosimone, J. Katz, P. V. Heuer, and D. H. Froula, "Measurements of Anisotropic Temperatures in Magnetized Gas-Jet Plasmas."

S. H. Cao, D. Patel, A. Lees, V. Gopalaswamy, C. Stoeckl, M. J. Rosenberg, H. Wen, H. Huang, A. Shvydky, R. Betti, and C. Ren, "Predicting Hot-Electron Generation in Inertial Confinement Fusion with Particle-in-Cell Simulations."

D. H. Edgell, A. Colaïtis, M. J. Guardalben, A. Kalb, J. Katz, J. Kwiatkowski, O. M. Mannion, A. Shvydky, C. Stoeckl, D. Turnbull, and D. H. Froula, "Cross-Beam Energy Transfer-Induced Nonuniformity in Direct-Drive Implosions on OMEGA."

R. Epstein, V. N. Goncharov, S. X. Hu, D. Cao, A. Shvydky, P. W. McKenty, G. W. Collins, and D. Haberberger, "Assessment of Radiation Trapping in Inertial Confinement Fusion Implosion Experiments with High-*Z*-Lined, Single-Shell Targets."

V. N. Goncharov, W. Trickey, I. V. Igumenshchev, N. Shaffer, T. J. B. Collins, R. K. Follett, W. Theobald, C. Stoeckl, R. C. Shah, C. Dorrer, J. D. Zuegel, D. R. Harding, S. Fess, E. M. Campbell, C. Deeney, S. Atzeni, L. Savino, F. Barbato, and A. Colaïtis, "Physics Requirements for High-Gain Inertial Confinement Fusion Target Designs."

D. Haberberger, A. Shvydky, C. Stoeckl, V. N. Goncharov, and D. H. Froula, "Schlieren Refraction Imaging for Cryo Implosions."

L. S. Leal, A. V. Maximov, F. García-Rubio, R. Betti, and V. V. Ivanov, "Modeling of Laser-Driven Ablative Magneto-thermal Instability."

A. V. Maximov, D. Turnbull, D. H. Edgell, R. K. Follett, H. Wen, J. P. Palastro, and D. H. Froula, "Nonlinear Laser–Plasma Coupling Caused by Two-Plasmon Decay and Cross-Beam Energy Transfer."

K. L. Nguyen, A. M. Hansen, D. Turnbull, R. K. Follett, D. H. Edgell, D. H. Froula, J. P. Palastro, L. Yin, and B. J. Albright, "Cross-Beam Energy Transfer Saturation by Ion-Trapping-Induced Detuning."

J. P. Palastro, D. Ramsey, M. Ambat, P. Franke, D. H. Froula, J. Pigeon, J. L. Shaw, T. T. Simpson, K. Weichman, B. Barbosa, B. Malaca, M. Pardal, J. Vieira, M. Vranic, M. Formanek, A. Di Piazza, J. Pierce, and W. Mori, "Nonlinear Thomson Scattering with Ponderomotive Control."

D. Ramsey, A. Di Piazza, M. Formanek, P. Franke, D. H. Froula, W. Mori, J. Pierce, T. T. Simpson, K. Weichman, and J. P. Palastro, "Exact Analytic Solutions Yielding Flying Focus Pulses (EASYFFP)."

H. G. Rinderknecht, G. Bruhaug, K. Weichman, M. Van Dusen-Gross, J. P. Palastro, M. S. Wei, A. Arefiev, T. Wang, T. Toncian, A. Laso Garcia, D. Doria, K. Spohr, H. J. Quevedo, T. Ditmire, J. Williams, A. Haid, and D. Stutman, "Relativistically Transparent Magnetic Filaments: a Short-Pulse Path to MegaTesla Fields and Efficient Gamma Radiation."

N. R. Shaffer, V. N. Goncharov, A. V. Maximov, and M. Sherlock, "An Extended Vlasov–Foller–Planck Approach to Laser Absorption and Ponderomotive Effects."

T. T. Simpson, J. Pigeon, M. Lim Pac Chong, D. Ramsey, K. Weichman, D. H. Froula, and J. P. Palastro, "High-Energy Two-Color Terahertz Generation."

A. A. Solodov, M. J. Rosenberg, M. Stoeckl, R. Betti, W. Seka, R. Epstein, C. Stoeckl, R. K. Follett, P. B. Radha, S. P. Regan, D. H. Froula, J. P. Palastro, E. M. Campbell, V. N. Goncharov, A. R. Christopherson, B. Bachman, M. Hohenberger, P. Michel, and J. F. Myatt, "Hot-Electron Preheat and Mitigation in Polar-Direct-Drive Experiments at the National Ignition Facility."

D. Turnbull, J. Katz, A. L. Milder, A. Shvydky, D. H. Froula, D. E. Hinkel, P. Michel, T. Chapman, L. Divol, E. Kur, S. MacLaren, M. Rosen, and G. B. Zimmerman, "Beam Spray Thresholds in ICF-Relevant Plasmas."

K. Weichman, J. P. Palastro, A. P. L. Robinson, and A. V. Arefiev, "Relativistically Thermal Plasma Generation by Magnetically Assisted Direct Laser Acceleration."

H. Wen, R. K. Follett, A. V. Maximov, and J. P. Palastro, "Mitigation of Inflationary Stimulated Raman Scattering with Laser Bandwidth."

The following presentations were made at the 24th Target Fabrication Specialist meeting, virtual, 6–9 June 2022:

J. M. García-Figueroa and D. R. Harding, "Observations on Smooth Diamond-Like Composition Films Deposited at Low Temperature via an Electron Cyclotron Resonance-Microwave-Chemical Vapor Deposition One-Step Process."

M. Wang and D. R. Harding, "Mechanical Properties of Micrometer-Size Foam Structures."

C. Deeney, "LLE Strategy," presented at the Office of Experimental Sciences Executives Meeting, Washington, DC, 8–9 June 2022.

The following presentations were made at Technology of Fusion Energy, Anaheim, CA, 12–16 June 2022:

M. Sharpe, C. Fagan, and W. T. Shmayda, "Influence of Microstructure on the Absorption of Tritium into Gold-Plated 316 Stainless Steel."

W. T. Shmayda, E. Dombrowski, and H. K. Mutha, "Pumping and Purifying the SPARC Tokamak Exhaust."

D. A. Chin, P. M. Nilson, J. J. Ruby, D. T. Bishel, R. Paul, M. Signor, A. Amouretti, A. Coleman, F. Coppari, M. K. Ginnane, X. Gong, M. Harmand, B. J. Henderson, S. X. Hu, O. Mathon, D. N. Polsin, E. Smith, R. Torchio, D. Trail, Y. Ping, J. R. Rygg, and G. W. Collins, "X-Ray Absorption Fine Structure Spectroscopy of Iron Compounds at High-Energy-Density Conditions," presented at the DOE NNSA Stewardship Science Graduate Fellowship, Santa Fe, NM, 20–23 June 2022.

E. M. Campbell, "Overview of Inertial Confinement Fusion History, Challenges, and Prospects for Driver-Target Concepts," presented at the Basic Research Needs Workshop, virtual, 21–23 June 2022.

R. B. Spielman and T. Joshi, "Annual Technical Review," presented at the Materials Science in Extreme Environments Annual Technical Review Meeting, Baltimore, MD, 22–24 June 2022.

C. Deeney, "The Laboratory for Laser Energetics: Progress in Science and Technology," presented at the Washington State University Institute for Shock Physics, Pullman, WA, 27 June 2022 (invited).

R Betti, A. Casner, X. Ribeyre, and W. Theobald, "Progress in Laser Direct Drive: Conventional and Shock Ignition," presented at the 48th European Physical Society Conference on Plasma Physics, virtual, 27 June–1 July 2022.